8-30-2018

Implementation and Analysis of Direct Torque Control for Permanent Magnet Synchronous Motor Using Gallium Nitride based Inverter

Junxi Cai
University of Windsor

Recommended Citation

Cai, Junxi, "Implementation and Analysis of Direct Torque Control for Permanent Magnet Synchronous Motor Using Gallium Nitride based Inverter" (2018). *Electronic Theses and Dissertations*. 7502.
https://scholar.uwindsor.ca/etd/7502

Implementation and Analysis of Direct Torque Control for Permanent Magnet Synchronous Motor Using Gallium Nitride based Inverter

By

Junxi Cai

A Thesis

Submitted to the Faculty of Graduate Studies
through the Department of Electrical and Computer Engineering
in Partial Fulfillment of the Requirements for
the Degree of Master of Applied Science
at the University of Windsor

Windsor, Ontario, Canada

2018

Implementation and Analysis of Direct Torque Control for Permanent Magnet Synchronous Motor Using Gallium Nitride based Inverter

by

Junxi Cai

APPROVED BY:

O. Jianu
Department of Mechanical, Automotive & Materials Engineering

M. Abdelkhalek
Department of Electrical and Computer Engineering

N. C. Kar, Advisor
Department of Electrical and Computer Engineering

August 27, 2018

DECLARATION OF ORIGINALITY

I hereby certify that I am the sole author of this thesis and that no part of this thesis has been published or submitted for publication.

I certify that, to the best of my knowledge, my thesis does not infringe upon anyone's copyright nor violate any proprietary rights and that any ideas, techniques, quotations, or any other material from the work of other people included in my thesis, published or otherwise, are fully acknowledged in accordance with the standard referencing practices. Furthermore, to the extent that I have included copyrighted material that surpasses the bounds of fair dealing within the meaning of the Canada Copyright Act, I certify that I have obtained a written permission from the copyright owner(s) to include such material(s) in my thesis and have included copies of such copyright clearances to my appendix.

I declare that this is a true copy of my thesis, including any final revisions, as approved by my thesis committee and the Graduate Studies office, and that this thesis has not been submitted for a higher degree to any other University or Institution.

ABSTRACT

Permanent magnet synchronous machines (PMSMs) attract considerable attention in various industrial applications, such as electric and hybrid electric vehicles, due to their high efficiency and high-power density. In this thesis, the mathematical model of PMSM and two popular control strategies, field-oriented control (FOC) and direct torque control (DTC), are analyzed and compared. The results demonstrated that the DTC has better dynamic response in comparison to FOC. Moreover, DTC can eliminate the use of position sensor, which will save the cost of the PMSM drive system. Therefore, this thesis focuses on the design and implementation of high-performance DTC for PMSMs with a Gallium Nitride (GaN) based high switching frequency motor drive.

First, the characteristics and operation principles of a PMSM are introduced. Then, the mathematical models of a PMSM under different coordinate systems are investigated. Consequently, a PMSM model is developed based on the *dq* rotating reference frame and implemented in the MATLAB/Simulink for validation. Two advanced PMSM control strategies, FOC and DTC, are investigated and compared in terms of control performance through comprehensive simulation studies and the results demonstrate that DTC has better dynamic performance.

Conventional DTC contributes to higher torque ripple in the PMSM due to the limited switching frequency in a conventional semiconductor-based motor drive, which inevitably deteriorates the drive performance. Therefore, this thesis aims to reduce the torque ripple in the DTC based PMSM drive by using the new generation wide bandgap switching devices. More specifically, DTC is improved by using the optimized space vector pulse width modulation strategy and a higher switching frequency contributed by the GaN based motor drive.

Finally, the proposed DTC-SVM based PMSM control strategy is implemented on the digital signal processor (DSP) and evaluated on the laboratory GaN based PMSM drive. Both the simulation and experimental results show that the proposed improvement in the DTC can further improve the PMSM drive performance.

DEDICATION

Dedicated to my parents and the memory of my grandfather and grandmother.

ACKNOWLEDGEMENTS

First and foremost, I give my sincere thanks to my advisor Dr. Narayan Kar, for providing me continuous guidance, support and numerous of resources for my study and research throughout the past two years in my MASc program. He inspired me with confidence and always encouraged me strive for the best. Dr. Kar treated me as a friend and a family member. It has been an honour working with him.

I would also like to express my gratitude and respect towards to my thesis committee members, Dr. Maher Abdelkhalek and Dr. Ofelia A. Jianu for agreeing to serve on my committee and, attending my seminars and defense. With their valuable suggestions and comments, I was able improve the quality of my research and this thesis.

My sincere thanks also go to Dr. Chunyan Lai, who has guided me in a supervisory role during my MASc study. She not only gave me constructive suggestions, but also shared her valuable research experience with me, which helped me solve many problems from my research and industry projects.

I am thankful to past and current lab colleagues and friends who supported me immensely during my research and life. Starting from Jiangbo Tian, who has introduced me into this program and continues cooperating with me for research and industry projects. My research group leader, Dr. Guodong Feng, his attitude to research inspires me to be diligent to my current and future work.

I am grateful to my parents who give me the chance to study abroad. Their continuous love and support gives me the confidence and strength to face and overcome all the difficulties in life.

TABLE OF CONTENTS

LIST OF TABLES

LIST OF FIGURES

NOMENCLATURE

u_{sd}, u_{sq} : d- and q- axis stator voltages (V)

i_{sd}, i_{sq} : d- and q- axis stator currents (A)

ψ_{sd}, ψ_{sq} : d- and q- axis stator flux linkages (V·s)

L_d, L_q : d- and q-axis inductances (H)

$u_{s\alpha}, u_{s\beta}$: α- and β- axis stator voltages (V)

$i_{s\alpha}, i_{s\beta}$: α- and β- axis stator currents (A)

$\psi_{s\alpha}, \psi_{s\beta}$: α- and β- axis stator flux linkages (V·s)

δ : Load angle (rad)

ψ_s : Stator flux linkage (V·s)

ψ_f : Rotor flux linkage (V·s)

p : Number of pole pairs

T_e : Electromagnetic torque (Nm)

f_{sw} : Switching frequency (Hz)

Chapter 1

Introduction

1.1 Background and Motivation

Motor control systems play an important role in the development of modern industry and society. The applications range widely from general purpose variable-speed drives, such as water pumps, wind fans and conveyors, to high-performance drives, e.g., robotics, CNC machines and electric vehicles. In the last century, for a long time, direct-current (DC) motor drives dominated the adjustable-speed drive market because of their excellent control performance, e.g., fast torque and speed dynamic response, and precise torque control in four-quadrant operations. There are two key control variables for the DC machine the excitation flux and electromagnetic torque which are naturally orthogonally decoupled so that they can be easily controlled by regulating the field and armature currents, respectively [1]. During DC motor drives dominated the market, the advanced control theory of alternating-current (AC) machines has not been developed and there are limitations in using the semiconductor devices for variable speed drives. As the result, the market for AC motor control systems was limited to undemanding applications, although AC machines have the advantages of simple structure, reliable operation, and easy maintenance. However, in recent years, the development of power electronics technology, microelectronics, and modern control theory has created favorable conditions for the development of AC motor drives. This makes AC motor drives more competitive in terms of performance and economy when compared with DC motor drives [2]. Due to their wide range of uses, there are many different types of AC motor drives.

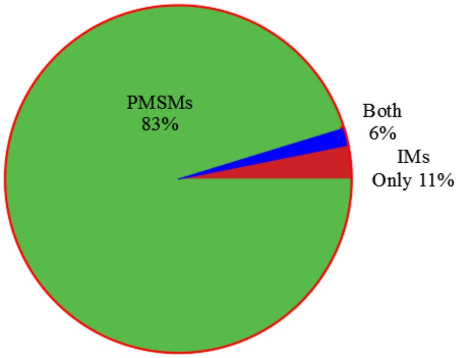

Fig. 1.1. Suppliers of vehicle traction motors [4].

Among various types of motor drives, permanent magnet (PM) brushless motor drives as well as the PM synchronous motor drive are currently the most attractive ones for electric vehicle (EV) propulsion. Their key features, namely high-power density and high efficiency are attributed to the use of high-energy PM material. PMSMs are becoming dominant in the market share of EV motor drives. [3]. It is reported that 83% of the vehicle traction motor manufacturers supply PMSMs [4], as shown in Fig. 1.1. Only 11% of the manufacturers supply induction machines (IMs) and 6% produce both PMSMs and IMs. Due to their popularity, more and more researchers have focused on the design and development of advanced control methodologies for PMSM drives, which significantly improves the dynamic performance, system robustness and reduce the complexity of control systems for PMSM drives.

1.2 Introduction of PMSMs

In general, PMSMs can be divided into two types according to the shape of back electromotive force (EMF): one with approximately sinusoidal back EMF, which normally adopts the distributed windings. The other with square or trapezoidal back EMF, is normally called brushless DC motor (BLDCM), which adopts the concentrated windings.

The one with sinusoidal back EMF can be broadly divided into non-salient-pole PMSMs (surface-mounted PMSMs) and salient-pole PMSMs (interior PMSMs), based on PM placement and rotor construction. As Fig. 1.2 shows, surface-mounted PMSMs have the PMs mounted on the surface of the rotor core. Consequently, the manufacturing and assembly of this type of machine is relatively simple [5]. On the other hand, interior PMSMs have the PMs buried deeply inside the rotor so that the rotor iron can effectively protect the PMs against centrifugal forces. Such rotor construction is more suitable for high-speed, flux-weakening operations [6].

Although there are distinct features between the two types of PMSMs, both are applied to the drive systems of EVs, such as Ford Focus with IPMSM drive and TM4 SPMSM drive for commercial vehicles. While the design is important, the focus of this thesis is the control strategies, which is outlined in the next section.

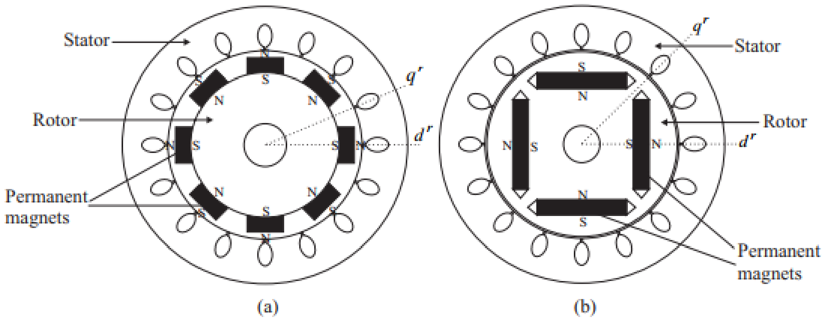

Fig. 1.2. Different rotor configurations for PMSMs. (a) Surface magnets type (b) Interior magnets type [6].

1.3 Control Theory of PMSMs

PMSMs are able to run at different speeds driven by a variable frequency drive. Typically, the classic control theory of PMSMs can be divided into three categories: scalar control, field-oriented control (FOC), and direct torque control (DTC). Each control theory is introduced in the following three sub-sections, respectively.

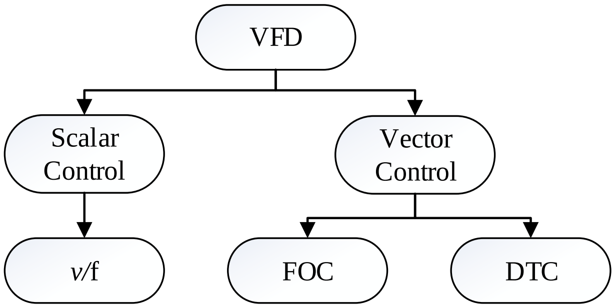

Fig. 1.3. Overview of key competing VFD control platforms.

1.3.1 Scalar Control

Scalar control, which is also called *v*/f control, is popular in general purpose industrial AC motor drives. A schematic diagram of a PMSM drive system equipped with a scalar control scheme is shown in Fig. 1.4. [6]. In the *v*/f control, the speed of PMSM is controlled by the adjustable magnitude of stator voltages and frequency. A voltage modulator is used to convert the three-phase voltage references to gate signals for the inverter. Since the scalar control focuses only on the steady-state dynamic and no feedback loop, the drive system’s transient behavior will not be satisfied. Also, the electromagnetic torque cannot be controlled directly. However, in some simple, low cost and sensorless motion implementation, PMSM drives with scalar control can achieve an acceptable steady-state response. As a result of that, scalar control is widely used in low-demand applications, such as pumps and fans [6].

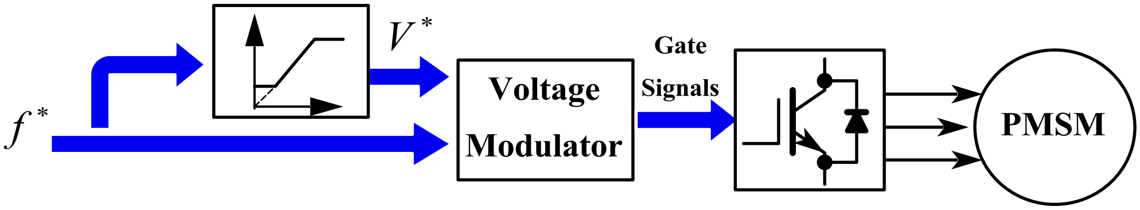

Fig. 1.4. Block diagram of scalar control for PMSM.

1.3.2 Field-Oriented Control

Operation theory of the DC motor shows that the produced torque and the flux can be independently tuned. However, AC machines do not have the same features as the DC motor. This becomes a barrier to AC drives to be widely accepted in the market. The issue was not solved until the 1970s when the FOC technique was first proposed for induction machines. Studies of AC machines showed that the mechanisms of torque production in AC and DC machines are quite similar [9]. With the help of the Park transformation, the current components corresponding to the field-magnetizing flux and torque generation in AC machines can be decoupled orthogonally so that the field-magnetizing flux can be controlled without affecting the dynamic response of the torque and vice versa. This is the basic principle of the FOC [10]. In FOC, the flux and torque of AC machines can be separately controlled as DC motors.

Shortly after it was proposed, FOC was successfully applied to synchronous motors. With the speed and current feedback, PMSM drive with FOC can achieve precise speed control and frees itself from the mechanical commutation drawbacks. Over the years, FOC drives have achieved a high degree of maturity in a wide range of applications. They have established a substantial worldwide market which continues to increase [11]. FOC can be divided into: air gap magnetic field orientated, stator magnetic field oriented, and rotor magnetic field oriented depending on the selected directional magnetic field. For the PMSM, due to the constant magnetic flux of the permanent magnet in the rotor, the rotor magnetic field oriented control is generally adopted. At present, the research and application objects mainly focus on sinusoidal PMSMs compared with the trapezoidal PMSMs. A schematic diagram of a PMSM drive system equipped with FOC is shown in Fig. 1.5. [6].

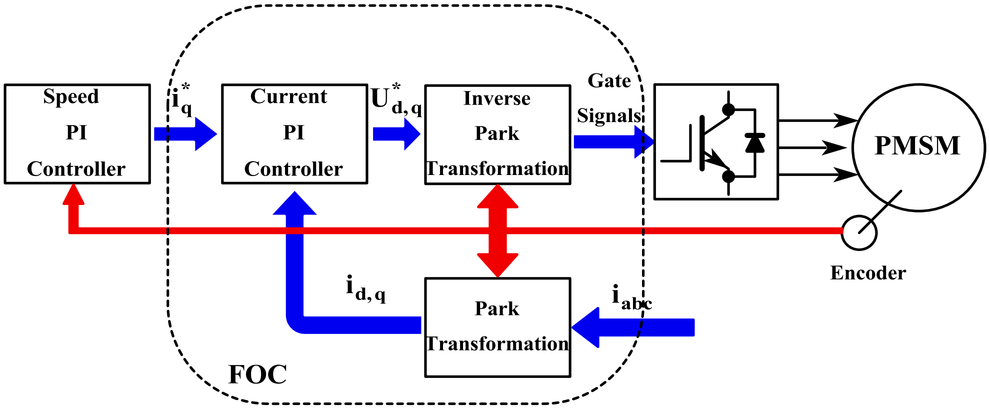

Fig. 1.5. Block diagram of field-oriented control for PMSM.

The control of the motor is essentially the control of the motor output torque, while the PMSMs FOC achieves indirect control of the torque by controlling the orthogonal current. According to the different control objectives, the specific control method of the stator orthogonal axis current can be divided into the following categories:

(1) I_d=0 control: this method is to control the direct axis current to be zero, so there is no direct axis armature reaction. Regardless of the surface PMSM or interior PMSM, the torque is only proportional to the quadrature axis current, and the control structure is simple. The disadvantage is that the motor power factor decreases as the load increases, and the inverter's capacity requirements are higher.

(2) Maximum torque per ampere (MTPA) control is a control method that strives to find the optimum points of operation to provide a specific torque and speed with minimum current. For surface PMSM, MTPA is equivalent to I_d=0 control. For interior PMSM, this control can make full use of the reluctance torque component of the motor.

(3) Unity power factor control: this method considers unity power factor as the control target to achieve a high-power factor operation of the motor by controlling the motor's orthogonal axis current component to reduce the inverter capacity. The disadvantage is that the maximum output torque is limited during the operation of the motor.

From above, different current control modes of FOC can be used to achieve different control targets. However, there is a fundamental commonality between these control methods, that is, traditional FOC methods mostly rely on the current loop to achieve indirect control of the motor torque.

1.3.3 Direct Torque Control

After proposed FOC, around 20 years later, direct torque control (DTC) was introduced by Takahashi and Noguchi in Japan [12], and Depenbrock in Germany [13,14]. Although the emergence of DTC was later than FOC, it had long been regarded as a revolutionary control scheme and a promising alternative to FOC for AC machines [15]. This method is first proposed for induction machines. However, for PMSMs, unlike induction machines, because there is no slip, it can not directly duplicate the DTC control scheme of the induction machines. In [16], through research on the torque generation mechanism of PMSMs, it shows that although there is no slip in PMSMs, the angle between the stator flux linkages and rotor flux linkages, which is the load angle, is very closely related to the electromagnetic torque of PMSMs. Under the condition that the stator flux amplitude is controlled to be constant, rapid control of the motor torque can be achieved by controlling the torque angle. The conventional DTC drive system is shown in Fig. 1.6 [6].

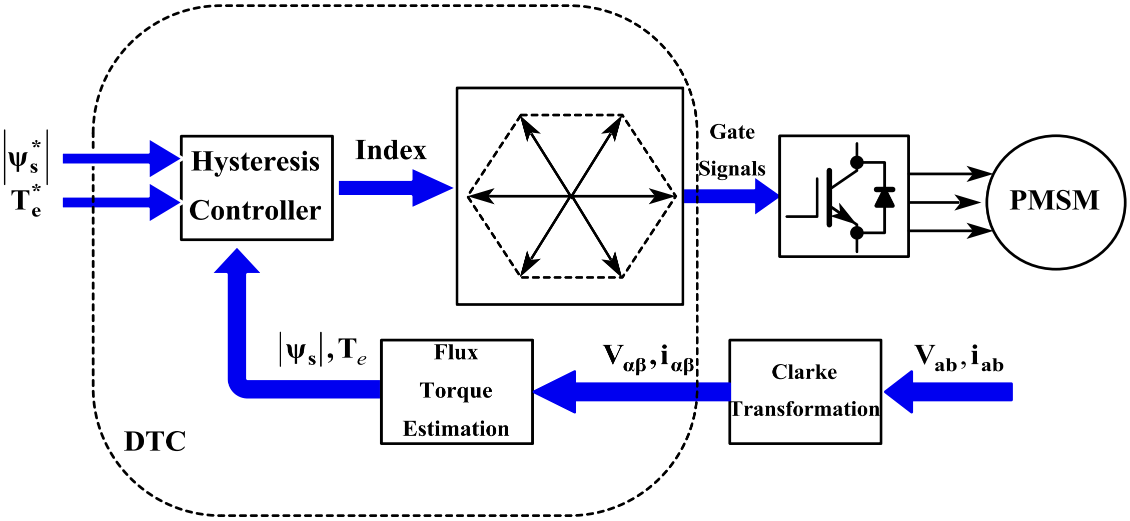

Fig. 1.6. Block diagram of conventional direct torque control for PMSM.

Different from FOC, DTC firstly observes the stator flux by flux observer, then determines the sector where the stator flux is located. Next, it calculates the electromagnetic torque, then the actual flux and torque will be compared with the reference, and a bang-bang control is usually adopted. Combing with the stator flux sector signal, appropriate voltage space vector is selected to control the stator flux amplitude to be constant and the change of the torque angle to achieve a direct torque control of the PMSMs.

The conventional DTC has the following characteristics:

Stator flux linkage and electromagnetic torque are directly obtained in the two-phase stationary coordinates of the stator. There is no need to change into the rotating coordinate, and the position information of the rotor is not required so it is easy to implement as sensorless control.

Also, DTC has low dependence on motor parameters. Stator resistance is the only parameter used when observing the flux linkage. The system has high robustness. Directly taking the motor torque as the control object eliminates the current control link and has good dynamic performance. In the report of ABB, it shows the torque dynamic response of a DTC drive system can be ten times faster than any other AC drive [17].

However, at the same time, it must be noted that the conventional DTC adopts an implementation similar as the bang-bang control, resulting in a large motor torque and flux linkage fluctuation, especially at low speed. Also, it also has other shortcomings, such as switching frequency is not fixed, noise, etc.

1.4 Research Objective and Contributions

The main objective of this thesis is to design and implement a high-performance control algorithm for a PMSM drive system with a digital processor. To this end, the control performance of FOC and DTC has been firstly investigated and compared from different aspects through MATLAB/Simulink simulation and laboratory experimental studies. Thereafter, the DTC is selected due to its better dynamic performance. Furthermore, issues encountered during DTC implementation in a GaN-based electric motor drive are discussed and resolved to achieve a satisfactory control performance. The main contributions of this thesis include:

(1) Develop MATLAB/Simulink simulation model of FOC and DTC based on the control diagram. From the MATLAB/Simulink simulation, making a comparison of FOC and DTC from dynamic and static performance.

(2) Based on the simulation results, further improvement of DTC control performance of PMSM would be discussed. An approach is to adjust the hysteresis control to reduce the torque ripple using GaN based inverter. The other approach is to apply SVPWM to DTC to achieve constant switching frequency which will make it feasible for hardware implementation.

(3) Hardware implementation of FOC and DTC-SVM have been achieved by DSP based motor drive to control PMSM. A hardware implementation has been presented as flowchart to explain the structure of the program. Moreover, algorithms implementation in discrete system like low-pass filter and high-pass filter have also been introduced.

1.5 Outline of the Thesis

The thesis is organized as follows.

Chapter 2 presents a comprehensive literature review of the DTC of PMSMs. A comparison between FOC and DTC will also be discussed. Furthermore, the state-of-the-art DTC improvement techniques are reviewed comprehensively. Then the principle and limitation from the conventional DTC will be analyzed to clarify the motivations for the research conducted for this thesis. Finally, a solution will be proposed to improve the conventional DTC control performance.

Chapter 3 presents the investigated simulation studies in MATLAB/Simulink for the comparison of FOC and DTC control performance of PMSMs. First, the simulation model of FOC is presented, then the simulation model of DTC is shown. In the end, the simulation results are compared to demonstrate that DTC has better dynamic response.

Chapter 4 focuses on the optimization of conventional DTC of PMSMs in term of torque ripple minimization. First, the torque ripple analysis is presented to explain how the bandwidth of hysteresis controller would affect on the steady state behavior. Then, an optimization solution for torque ripple minimization is presented. In order to achieve the objectives, an innovative inverter based on Gallium Nitride (GaN) has been introduced to improve the switching frequency of the drive system for the implementation of high performance DTC. Then, the DTC-SVM with constant switching frequency has been developed and validated through MATLAB/Simulink simulation to demonstrate that the proposed approach is able to achieve the objective of torque ripple minimization.

Chapter 5 presents the hardware implementation of DTC-SVM for PMSM using GaN based inverter. It mainly focuses on the process of hardware implementation. This chapter is divided into two parts: hardware implementation of DTC-SVM. First, the digital signal processer (DSP) TMS320F28335 build by Texas Instruments will be introduced. Then, hardware implementation of DTC-SVM is presented to demonstrate and validate the proposed improved DTC control strategy for PMSM drive.

Chapter 2

PMSM Modeling and Control Strategies

This chapter is divided into four parts. First, the mathematical model of PMSM in different reference frame is introduced. Secondly, comparative results on FOC and DTC are reviewed from the literature. Third, a comprehensive literature review of DTC techniques is presented. Eventually, the principle from the conventional DTC is analyzed to clarify the motivations for the research work 1cconducted in this thesis.

2.1. Mathematical Model of PMSMs

The mathematical model of AC machines is a time-variant, multivariable, nonlinear and coupling system. To obtain excellent control of PMSMs, their mathematical model needs to be established based on the hypotheses below:

(1) Neglecting core saturation, irrespective of core eddy current and hysteresis loss;
(2) The electric conductivity of permanent magnet material is zero;
(3) No damper windings in rotor;
(4) The excitation magnetic field generated by the permanent magnet and the armature reaction magnetic field generated by the three-phase winding are all sinusoidal distributed in the air gap.

Generally, there are four Coordinate Systems below used to analysis the control of PMSMs:

(1) Three-phase stationary reference frame *abc*

In this reference frame, the *abc* axes are the three-phase winding axis of the motor, and the components of the motor voltage, current, and flux on the coordinate axis are the actual three-phase components of the motor. In this coordinate system, the motor equation is a variable coefficient differential equation, and the solution to the equation is more complicated.

(2) Two-phase stationary reference frame αβ

In the αβ two-phase stationary frame, the α-axis aligns with the α -phase winding, and the β-axis leads the α -axis by 90 degrees.

(3) Two-phase stator flux synchronously rotating reference frame *xy*

The *xy* reference frame is a coordinate system that rotates synchronously with the stator flux vector, where the direction of *x*-axis is the same as the direction of the stator flux vector, the *y*-axis leads the *x*-axis by 90 degrees, and the angle between the *x*-axis and the α-axis winding is θ_s.

(4) Two-phase rotor flux synchronously rotating reference frame *dq*

In this coordinate system, the direction of the *d*-axis is the direction of the permanent magnet flux of the rotor, and the *q*-axis is 90 degrees ahead of the *d*-axis. The *dq* coordinate system rotates synchronously with the rotor permanent magnet flux, and the angle between the axis of the *d*-axis and the α -phase winding is θ_r.

From the introduction to different reference frames, it can be seen that there are differences and connections between these reference frames. The relationship between different reference frames is shown as Fig. 2.1, ψ_s the stator flux linkage vector, ψ_r is rotor (magnet) flux linkage vector. The angle between the stator and rotor flux linkages δ is the load angle when the stator resistance is neglected. In the steady state, δ is constant corresponding to a load torque, and both stator and rotor flux rotate at the synchronous speed. In transient operation, δ varies and the stator and rotor flux rotate at different speeds [8].

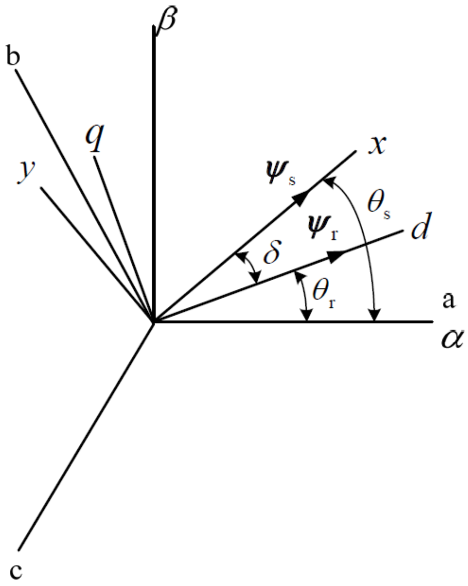

Fig. 2.1. The stator and rotor flux linkage in different reference frames.

In order to analyze different reference frames, a transformation will be used. The transformations for different reference frames are shown as below:

(1) The transformation of *abc*↔αβ

The conversion is known as Clarke Transformation. Assuming *F* represents the voltage, current and flux linkage, in *abc* reference frame are F_a, F_b, F_c and in αβ reference frame are F_α, F_β. The transformation will be:

$$\begin{bmatrix} F_\alpha \\ F_\beta \end{bmatrix} = C_{3s/2s} \begin{bmatrix} 1 & -\frac{1}{2} & -\frac{1}{2} \\ 0 & \frac{\sqrt{3}}{2} & -\frac{\sqrt{3}}{2} \\ \frac{\sqrt{2}}{2} & \frac{\sqrt{2}}{2} & \frac{\sqrt{2}}{2} \end{bmatrix} \begin{bmatrix} F_a \\ F_b \\ F_c \end{bmatrix} \tag{1}$$

$$\begin{bmatrix} F_a \\ F_b \\ F_c \end{bmatrix} = C_{2s/3s} \begin{bmatrix} 1 & 0 & \frac{\sqrt{2}}{2} \\ -\frac{1}{2} & \frac{\sqrt{3}}{2} & \frac{\sqrt{2}}{2} \\ -\frac{1}{2} & -\frac{\sqrt{3}}{2} & \frac{\sqrt{2}}{2} \end{bmatrix} \begin{bmatrix} F_\alpha \\ F_\beta \end{bmatrix} \tag{2}$$

Where C is the coefficient before and after the transformation. For constant power conversion, $C_{3s/2s} = \sqrt{\frac{2}{3}}, C_{2s/3s} = \sqrt{\frac{2}{3}}$, and for constant amplitude conversion, $C_{3s/2s} = \frac{2}{3}, C_{2s/3s} = 1$.

(2) The transformation of $\alpha\beta \leftrightarrow dq$

The conversion is known as Park Transformation. Assuming F represents the voltage, current and flux linkage, in dq reference frame are F_d, F_q. The transformation is:

$$\begin{bmatrix} F_d \\ F_q \end{bmatrix} = \begin{bmatrix} \cos\theta_r & \sin\theta_r \\ -\sin\theta_r & \cos\theta_r \end{bmatrix} \begin{bmatrix} F_\alpha \\ F_\beta \end{bmatrix} \tag{3}$$

$$\begin{bmatrix} F_\alpha \\ F_\beta \end{bmatrix} = \begin{bmatrix} \cos\theta_r & -\sin\theta_r \\ \sin\theta_r & \cos\theta_r \end{bmatrix} \begin{bmatrix} F_d \\ F_q \end{bmatrix} \tag{4}$$

(3) The transformation of $xy \leftrightarrow dq$

Assuming F represents the voltage, current and flux linkage, in xy reference frame are F_x, F_y. The transformation is:

$$\begin{bmatrix} F_x \\ F_y \end{bmatrix} = \begin{bmatrix} \cos\delta & \sin\delta \\ -\sin\delta & \cos\delta \end{bmatrix} \begin{bmatrix} F_d \\ F_q \end{bmatrix} \tag{5}$$

$$\begin{bmatrix} F_d \\ F_q \end{bmatrix} = \begin{bmatrix} \cos\delta & -\sin\delta \\ \sin\delta & \cos\delta \end{bmatrix} \begin{bmatrix} F_x \\ F_y \end{bmatrix} \tag{6}$$

The well-known dynamic equations of a three-phase PMSM can be written in the dq reference frame as follows:

$$\begin{cases} u_{sd} = R_s i_{sd} + \dfrac{d\psi_{sd}}{dt} - \omega_e \psi_{sq} \\ u_{sq} = R_s i_{sq} + \dfrac{d\psi_{sq}}{dt} + \omega_e \psi_{sd} \end{cases} \tag{7}$$

Where u_{sd} and u_{sq} are the *d*- and *q*-axis stator terminal voltages, respectively, i_{sd} and i_{sq} are the *d*- and *q*-axis stator currents, R_s is the resistance of stator windings, ω_e is the rotor electrical angular speed. The *d*- and *q*-axis stator flux linkages of the PMSM ψ_{sd} and ψ_{sq} have the form of:

$$\begin{cases} \psi_{sd} = L_d i_{sd} + \psi_f \\ \psi_{sq} = L_q i_{sq} \end{cases} \tag{8}$$

Where L_d and L_q are the *d*- and *q*-axis inductances of the PMSM. ψ_f is the flux linkage generated by the PMs.

The electromagnetic torque T_e generated by the PMSM can be calculated by:

$$\begin{aligned} T_e &= \frac{3}{2} p\left(\psi_{sd} i_{sq} - \psi_{sq} i_{sd}\right) \\ &= \frac{3}{2} p\left[\psi_f i_{sq} + \left(L_d - L_q\right) i_{sd} i_{sq}\right] \end{aligned} \tag{9}$$

Where p is the number of pole pairs. It can also be rewritten in terms of stator flux linkage and load angle, which is

$$T_e = \frac{3p}{4L_d L_q} |\psi_s| \left[2\psi_f L_q \sin\delta - |\psi_s| \left(L_q - L_d\right) \sin 2\delta\right] \tag{10}$$

Where $|\psi_f|$ is the magnitude of the stator flux linkage. The electromagnetic torque consists of two terms. The first is the excitation torque, which is produced by the permanent magnet flux, and the second term is the reluctance torque. For a PMSM with saliency ($L_d \neq L_q$), the difference between the asymmetrical flux paths in the *d*- and *q*-axis produces the reluctance torque which is not present in a nonsalient-pole PMSM [6].

Equation (7)-(10) can be transformed into the αβ stationary reference frame with the inverse Park transformation, which is given by:

$$\begin{bmatrix} u_{s\alpha} \\ u_{s\beta} \end{bmatrix} = \begin{bmatrix} R_s & 0 \\ 0 & R_s \end{bmatrix} \begin{bmatrix} i_{s\alpha} \\ i_{s\beta} \end{bmatrix} + \frac{d}{dt} \begin{bmatrix} \psi_{s\alpha} \\ \psi_{s\beta} \end{bmatrix} \tag{11}$$

Where $u_{s\alpha}$ and $u_{s\beta}$ are the α- and β-axis stator terminal voltages, respectively, $i_{s\alpha}$ and $i_{s\beta}$ are the α- and β-axis stator currents, $\psi_{s\alpha}$ and $\psi_{s\beta}$ are the α- and β-axis stator flux linkages.

The electromagnetic torque T_e can also be calculated by:

$$T_e = \frac{3}{2} p \left(\psi_{s\alpha} i_{s\beta} - \psi_{s\beta} i_{s\alpha} \right) \tag{12}$$

According to different control theory, mathematical models in different reference frames are used for analysis. For example, conventional field-oriented control is preferably implemented in the *dq* reference frame, while conventional direct torque control is preferably implemented in the αβ reference frame. A spatial illustration of the stator flux components in the αβ and *dq* reference frames is shown in Fig. 2.2 [6].

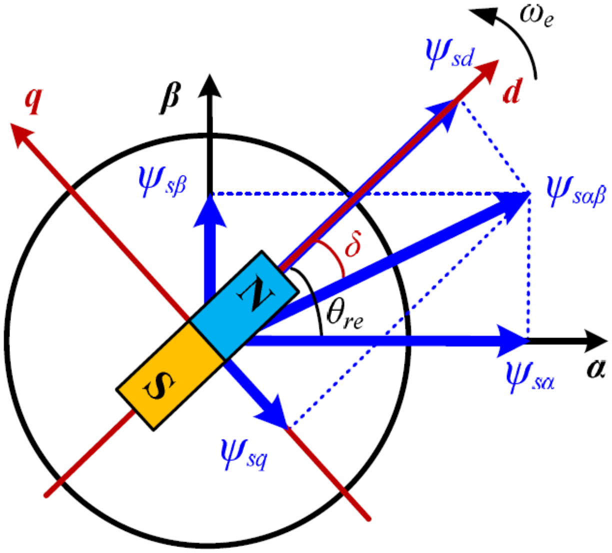

Fig. 2.2. Illustration of the stator flux components in αβ stationary and synchronously rotating *dq* reference frames [6].

2.2 Comparison Between FOC and DTC Strategies for PMSMs

Table. 2.1. summarizes and compares FOC and DTC from the aspects of the controllers' features, dynamic performance, steady-state behavior and implementation complexity [18].

Table. 2.1. Summary of the comparison between FOC and DTC [18]

Comparison property	FOC	DTC
Dynamic response	Fast	Very fast
Steady-state behavior	Low ripple and distortion	High ripple and distortion
Switching frequency	Constant	Variable
Parameter sensitivity	High	Low
Requirement of rotor position	Yes	No
Current control	Yes	No
PWM modulator	Yes	No
Coordinate transformation	Yes	No
Control tuning	PI gains	Hysteresis bands
Complexity and processing requirements	Higher	Lower

This thesis mainly focuses on the dynamic response and steady-state behavior. From Table. 2.1, it can be known that for dynamic response, DTC is faster than FOC. However, for the steady-state behavior, FOC is better than DTC.

In view of the deficiencies of the conventional DTC of PMSMs, researches and scholars from all over the world have conducted a series of studied and improvements and made a great progress. In the next subsection, there is a literature review on DTC of PMSMs.

2.3 Literature Review of Existing DTC Techniques

The DTC using hysteresis controllers to regulate the stator flux linkage and electromagnetic torque with only nonzero voltage space vector has been proposed in [8] and it shows a significant torque ripple. Large torque ripples will inevitably affect the stability of the low speed performance of the motor. Existing research has proposed many different ways to reduce torque ripples in the DTC based PMSM and induction machine drive systems [19-32]. Therefore, the corresponding research work on torque ripple investigation and reduction is also introduced in this review.

Based on the conventional DTC, research is seeking to reduce torque ripple from the perspective of improvement and optimization of torque flux linkage regulators and switching table. In [19], after analyzing the effect of the voltage space vector on the torque, the zero-voltage vector is introduced into the torque regulator, and the zero-voltage vector is used to maintain the torque to reduce the torque ripple. This method has achieved a good result of torque ripple minimization and has further improved the conventional DTC. However, it missed the further discussion about how long the zero-voltage vector should be applied. For digital control system, when using the conventional DTC, the voltage space vector selected by the flux linkage and torque regulators is applied to the entire control cycle. Once a non-zero vector has been selected, it can not be controlled, which inevitably brings the torque ripple issue. Therefore, some researches have proposed a method to reduce the torque ripple from the perspective of controlling the acting time the voltage space vector. [20] V. Ambrozic presents a method to calculate the non-zero voltage vector acting time through the difference between the actual torque and torque reference combined with the equation of torque in a control cycle. The rest would be the acting time for zero voltage vector used for torque ripple minimization.

The conventional DTC only utilizes six non-zero voltage vector. However, synthesizing more voltage space vectors is becoming another method to achieve torque ripple minimization. This helps increase the control in the control cycle. In [21-24], the researchers make it possible to synthesize a higher number of voltage vectors with respect to conventional DTC scheme through using prefixed time intervals within a control cycle period. With the increase of the available voltage space vector, the torque error in the torque regulator can be divided into different levels. According to the magnitude of the torque error range, a suitable voltage space vector is selected from the synthesized voltage space vectors to compensate for the torque error. In practice, the extended switch table is pre-defined in the controller without extra calculation. Due to more voltage space vectors, multiple control of the motor flux linkage and torque can be achieved within one control cycle, thus increasing the control accuracy and effectively reducing torque ripple.

Aside from synthesizing more voltage space vectors, there are some researches looking into how stator flux linkage sectors will effect on the torque ripple. In [25-27], Y. Kwak, S. S. Sebtahmadi and X. Liao analyze the effect of the voltage space vector on the torque and flux linkage in the conventional DTC. For the selected voltage space vector both the torque and flux control requirements are taken into consideration at the same time. The results show that the control effect of the voltage space vector on the amplitude and torque of the magnetic flux will also be affected as the stator flux linkages position changes. Therefore, it is difficult to achieve effective control of torque and stator flux linkages at the same time. In order to solve this issue, a method of 12 sectors division is used. Within each new sector, the voltage space vector selection table is determined based on the effect of each spatial voltage vector on the amplitude and position of the stator flux linkages. This method improves the control effect of the flux linkage and torque and achieves the purpose of reducing torque ripple.

Due to the hysteresis control, the sampling frequency of an inverter in DTC must be higher than that with FOC. Therefore, it is vital to determine the switching frequency of the inverter for DTC; taking into account that it varies with the operation point [28]. In [29] the relationship between the inverter switching frequency and the width of the hysteresis bands of the controllers was studied in detail, together with the impact of motor parameters and speed. Generally speaking, smaller torque hysteresis band will result in smaller torque ripple but higher switching frequency. However, this is limited by computational speed of digital control system and operational frequency of power switch.

Although synthesizing voltage space vectors and stator flux linkage section division can help to reduce the torque ripple, the number of voltage space vectors and sections are not endless. Some researchers have learnt from the idea of vector synthesis and sector division and made further advances. The basic idea is to use space voltage vector modulation (SVM) technology to synthesize an optimal voltage space vector based on the motor torque and flux control requirements [30-37]. This will accurately compensate the flux linkage and torque error, and finally achieve the purpose of reducing torque ripple [35]. Conventional switching-table-based DTC utilizes one of a limited number of voltage vectors with fixed magnitudes and positions in each control period. However, DTC-SVM can synthesize an arbitrary reference voltage vector within its linear range with multiple vectors in each sampling interval [36]. SVM-based DTC can calculate the required voltage vector to simultaneously regulate the stator flux and torque of the PMSM which significantly reduces the torque ripple with constant switching frequency. The caveat is the usage of the SVM increases the computational burden as compared to the conventional DTC [37].

In the past decades, modern control theories were widely used in power and dynamic control systems. Many new DTC controllers were realized by combining traditional DTC schemes with modern control methods such as fuzzy logic control, sliding mode and artificial neural network [28]. The development of the digital controller provides good conditions for the implementation of DTC methods based on modern control theory.

In the conventional DTC, when the different voltage space vector is selected to act on the motor, the state of the switch of the inverter will change accordingly. With that change of state, the entire circuit structure also changes. From this perspective, the DTC system itself has a variable structure. Therefore, it is reasonable to apply sliding mode and variable structure control into DTC, since it is well suited for nonlinear dynamic systems with uncertainties. Sliding mode control ideas have been investigated for the SVM-DTC of induction motors. They are characterized by the fact that enforcing a sliding mode leads to low sensitivity with respect to a class of disturbances and plant parameter variations [28]. In [38-39], variable structure control method is used for torque and stator flux control.

In addition to sliding mode and variable structure control, fuzzy logic control has also been applied to DTC [40]. The errors of the torque, stator flux linkage and flux linkage angular position of the PMSM are fuzzified into several fuzzy subsets. This is done to select a suitable voltage space vector to obtain fast torque response and smooth the torque and flux linkage ripples simultaneously. The stator flux linkage vector angle is also mapped to a single reduced 60 degree region. This is based on the symmetry of the control rules for each 60 degree flux linkage angular region. As a result, the torque response performance can be improved because of the minimization of the number of fuzzy reasoning rules and hence the reasoning time.

The neural network is well known for its learning ability and approximation to any arbitrary continuous function. Neural networks have recently shown good promise for application in power electronics and motion control system. It has been stated in the literatures that artificial neural network can be applied to DTC controller design, parameter identification and state estimation of motor control systems [28]. In [41], two kinds of neural network controllers were used to perform as the state selector of DTC for an inverter-fed IPMSM. The result indicates that it is possible to replace switching table of the DTC for permanent magnet synchronous motor by a neural network controller and achieve high torque dynamic response.

2.4 Principle of DTC

As aforementioned, DTC can achieve rapid control of the torque. In contrast to induction machines, there is no slip between stator and rotor of PMSMs. Therefore, the DTC used for induction machines cannot be directly applied to PMSMs. However, the angle between the stator flux linkages and rotor flux linkages, which is the load angle, is very closely related to the electromagnetic torque of PMSMs. Equation (10) with constant motor parameters, shows that the amplitude of torque depends on stator flux amplitude and load angle. Since the the reluctance torque exists in interior PMSMs, the *d*- and *q*-axis inductances will impact the torque.

For surface-mounted PMSMs, there is no reluctance torque, thus the electromagnetic torque equation will be:

$$T_e = \frac{3p}{2L_s}|\psi_s|\psi_f \sin\delta \tag{13}$$

Equation (13) implies that the torque increases with the increase of δ. If the amplitude of stator flux linkage ψ_s is kept constant and the load angle δ is controlled within the range of -90°-90°. Then, the derivative of Equation (13) with respect to the load angle can be derived as:

$$\frac{dT_e}{d\delta} = \frac{3p}{2L_s}|\psi_s|\psi_f \dot{\delta}\cos\delta \tag{14}$$

The relationship between torque and load angle δ of surface PMSMs has been shown as Fig. 2.3.

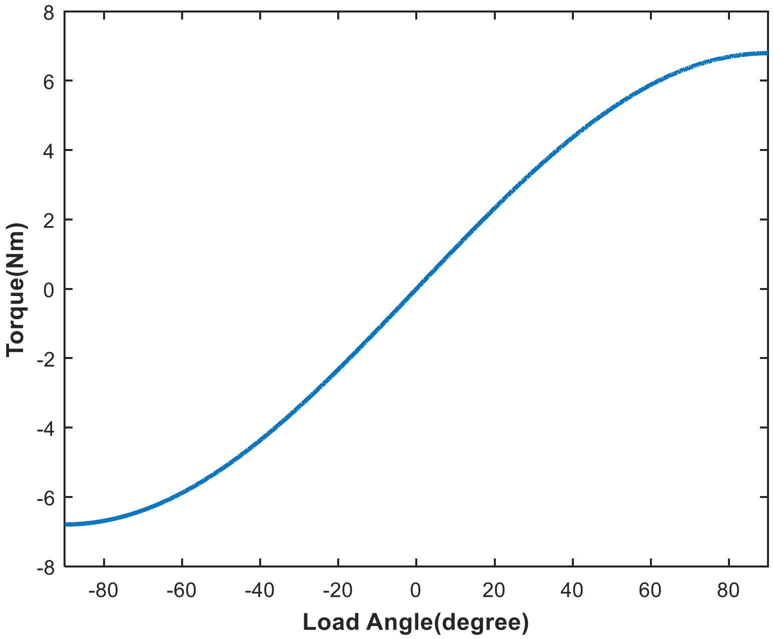

Fig. 2.3 The relationship between torque and load angle δ of surface PMSMs.

From Fig. 2.3, shows within the range of -90°-90°, Equation (14) is always positive. This implies that the increase of torque is proportional to the increase of the load angle δ. In other words, the stator flux linkage should be controlled in such a way that the amplitude is kept constant and the rotating speed is controlled as fast as possible to obtain the maximum change in actual torque [8].

However, for interior PMSMs, since $L_d \neq L_q$, the derivative of the electromagnetic torque with respect to the load angle will be:

$$\frac{dT_e}{d\delta} = \frac{3p}{4L_d L_q}|\psi_s|\left[2\psi_f L_q \dot{\delta}\cos\delta - 2|\psi_s|\left(L_q - L_d\right)\dot{\delta}\cos 2\delta\right] \tag{15}$$

In interior PMSMs the torque increases with the increase of the load angle δ due to the reluctance torque as can be observed Equation (15). It is necessary to discuss the relationship between the amplitude of stator flux linkage and the derivative of the torque. Fig. 2.4. shows the relationship between torque and load angle of interior PMSMs when the amplitude of stator flux linkage is at $0.5\psi_f$, ψ_f, $1.5\psi_f$, $2\psi_f$.

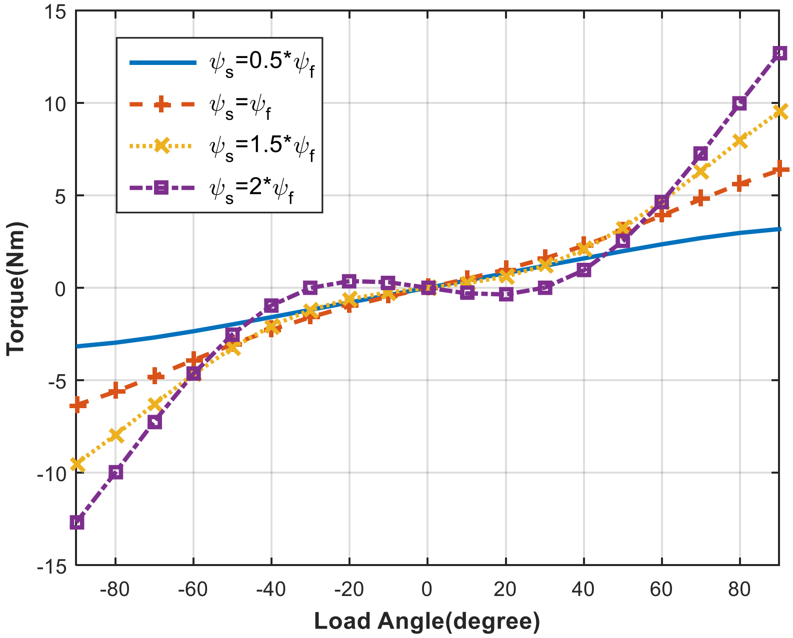

Fig. 2.4. The relationship between torque and load angle δ of interior PMSMs.

Note that for the torque near the zero point, when $\psi_s = 2\psi_f$, the derivative of torque is negative, so DTC cannot be applied in this case. In order to assure it is always positive, Equation (15) should satisfy the condition below (16).

$$|\psi_s| < \frac{L_q}{L_q - L_d}\psi_f \tag{16}$$

Through the equations and discussions, the control of the stator flux linkage and load torque can be achieved by selecting the appropriate stator voltage vectors. Generally, two-level or three-phase voltage source inverter is used for PMSM drive systems. As shown below as Fig. 2.5, the primary voltage V_a, V_b, V_c are determined by the status of the three power switches, which called S_a, S_b, S_c here.

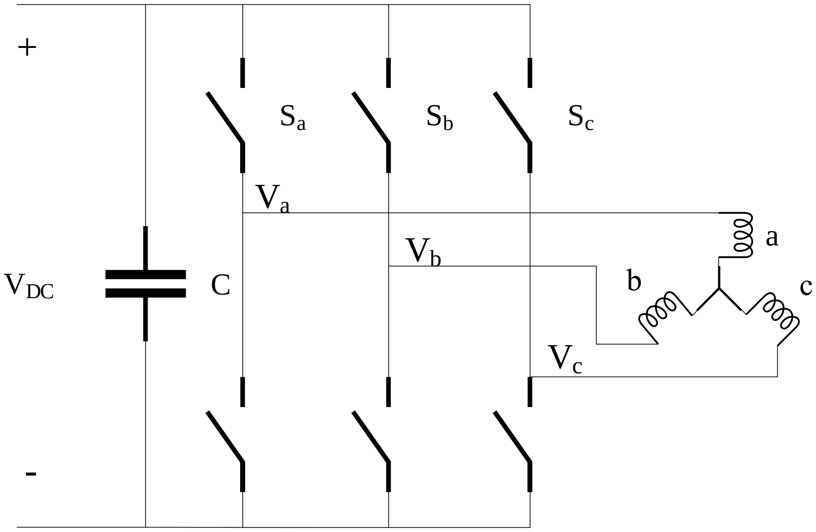

Fig. 2.5. A voltage source inverter-fed PMSM drive system.

The V_a, V_b, V_c can be presented in Equation (17) with the respect to S_a, S_b, S_c:

$$\begin{cases} V_a = \frac{1}{3}V_{DC}\left(2S_a - S_b - S_c\right) \\ V_b = \frac{1}{3}V_{DC}\left(2S_b - S_a - S_c\right) \\ V_c = \frac{1}{3}V_{DC}\left(2S_c - S_a - S_b\right) \end{cases} \tag{17}$$

Through the different switching statuses, the controller generates eight voltage space vectors, six of them are non-zero voltage vectors, and the rest are zero voltage vectors, as Fig. 2.6. shows below. Each voltage space vector has the numerical label to show the status of power switches in order of S_a, S_b, S_c. To achieve the stator flux trajectory circular, the stator flux vector space in the αβ stationary reference frame is divided into six sectors equally, which is the dotted line in Fig. 2.6. The sector can be selected based on the position of the estimated stator flux, which can be obtained from the α-, and β-axis stator flux components, as Equation (18) shows below:

$$\theta = \tan^{-1}\left(\frac{\psi_{s\beta}}{\psi_{s\alpha}}\right) \tag{18}$$

Where θ presents the angle of stator flux.

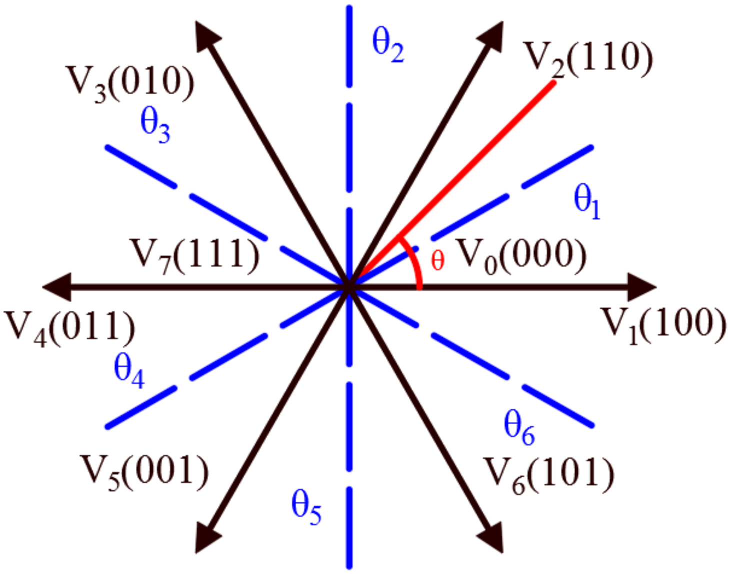

Fig. 2.6. Voltage space vectors and sectors in the αβ reference frame.

For PMSMs, the stator flux vector in α-, and β-axis can be expressed by:

$$\psi_{s\alpha\beta}(t)=\int\left(V_{s\alpha\beta}(t)-R_s i_{\alpha\beta}(t)\right)dt \tag{19}$$

If neglecting the voltage drop on the resistor, Equation (19) can be simplified as

$$\psi_{s\alpha\beta}(\Delta t)=V_{s\alpha\beta}\Delta t+\psi_{s\alpha\beta}\big|_{t=0} \tag{20}$$

Figure 2.7 shows the illustration of the voltage space vectors effect on the torque and stator. This diagram will help in analyzing the effects of the voltage space vector on the variations in the toque and stator flux.

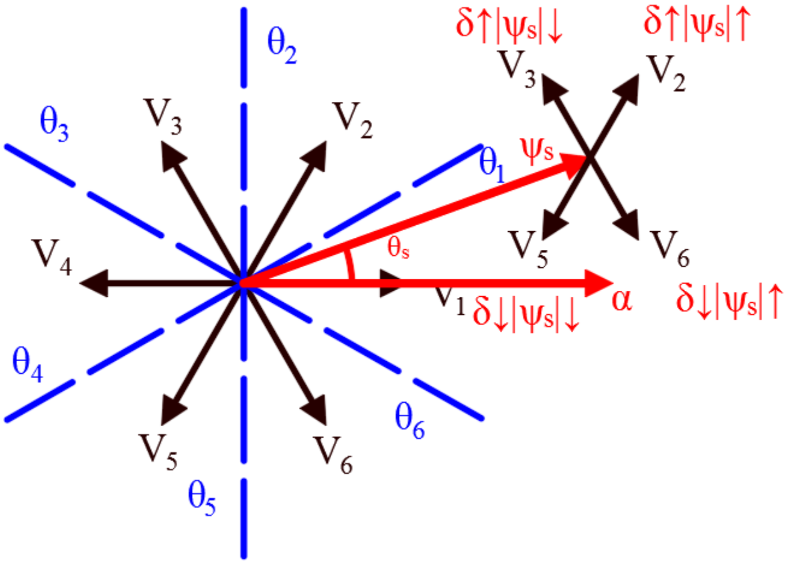

Fig. 2.7. Illustration of the voltage space vectors effect on the torque and stator flux.

Assuming the PMSM is rotating at the counter-clock direction, the stator flux vector lies in Sector 1. This also assumes the stator flux vector is ψ_s at this moment. From Fig. 2.7, the variations of the torque and stator flux is illustrated by applying different voltage space vector (V_2, V_3, V_4, V_5, V_6). If V_2 is applied, it will make the stator flux rotate counter clockwise, which will increase the load angle δ and stator flux magnitude. Therefore, according to Equation (10), the torque will increase. Similarly, if V_5 is applied, both the load angle δ and the stator flux magnitude will decrease, thus torque will decrease. Again, when V_3 is applied, the load angle δ will increase but the stator flux magnitude will decrease. Overall, the torque still increases because the weight of the load angle on the torque change is larger than that of the stator flux magnitude. Similarly, V_6 reduces the load angle δ but increase the stator flux magnitude. Although the other active voltage space vectors V_1 and V_4 can also increase or decrease the stator flux magnitude to effect on the change of torque, the signs of the associated torque variations are not consistent. That is why only four active voltage space vectors are used in the Sector 1.

Similarly, in other different sector, there also exists four active voltage space vectors that can be selected. This is determined by the requirements of the stator flux linkage and torque changes. Figure 2.8. shows the control of stator flux linkage and torque. It demonstrates that the stator flux linkage is circular, and the width of the circle is decided by the band width of the hysteresis controller, which will be discussed later.

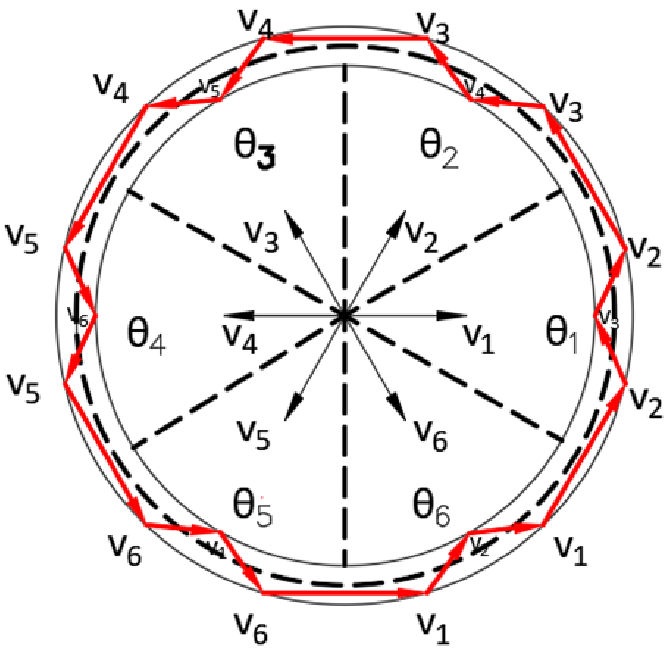

Fig. 2.8. The control of stator flux linkage and torque.

For conventional DTC of PMSM, the closed-loop control of the stator flux linkage magnitude and torque is required. In the first proposed DTC of PMSM, the stator flux linkage and torque regulator were as follows [8]:

$$\phi = \begin{cases} 1\left(\left|\psi_s\right|^* - \left|\psi_s\right| > 0\right) \\ 0\left(\left|\psi_s\right|^* - \left|\psi_s\right| < 0\right) \end{cases} \tag{21}$$

$$\tau = \begin{cases} 1\left(T_e^* - T_e > 0\right) \\ -1\left(T_e^* - T_e < 0\right) \end{cases} \tag{22}$$

Where $|\psi_s|^*$ is the stator flux linkage reference, ϕ is the output of the stator flux linkage regulator. If $\phi=1$ means the stator flux linkage need to be increase, then according to the sector appropriate voltage space vector will be selected. Else, the stator flux linkage needs to be decreased. T_e^* is the torque reference, and τ is the output of the torque regulator. If $\tau=1$ means the actual torque is smaller than the reference, else it is larger than the reference. According to the selection rules of voltage space vectors in different sectors, the switching table is obtained by combining the output of the stator flux linkage and torque regulators as follows:

Table. 2.2. Switching table in the conventional DTC

ϕ	τ	θ_1	θ_2	θ_3	θ_4	θ_5	θ_6
1	1	V_2	V_3	V_4	V_5	V_6	V_1
	-1	V_6	V_1	V_2	V_3	V_4	V_5
0	1	V_3	V_4	V_5	V_6	V_1	V_2
	-1	V_5	V_6	V_1	V_2	V_3	V_4

Eventually, the DTC of PMSM schematic diagram is shown as Fig. 1.8. From the schematic diagram, the voltage and current are first sampled, then the components of the voltage and current in the stationary two-phase reference frames are obtained through coordinate transformation. According to the relationship between the voltage current and the stator flux components, the stator flux linkage of the PMSM is observed. Then the amplitude and sector of the stator flux linkage can be known. Combined with the sampled current, the actual torque can be calculated. And the torque reference is obtained by the speed regulator to be the input of the torque regulator. After comparison, the output of the torque regulator can be determined. Similarly, the flux regulator can be determined. According to Table. 2.2, appropriate voltage space vector will be selected to realize the DTC of PMSMs.

Chapter 3

Investigations of FOC and DTC of PMSMs through Simulations

In this chapter, the simulation studies were investigated using the MATLAB/Simulink software for the comparison of FOC and DTC control performance of PMSMs. First, the simulation model of FOC is presented, then the simulation model of DTC is shown. In the end, comparison studies are conducted based on the simulation results.

3.1 Motor Parameters for Simulation of FOC and DTC

The PMSM under test is from Estun Automation. Table. 3.1. below shows the parameters of the servo PMSM.

Table. 3.1. Motor Parameters for Simulation of FOC and DTC

Motor Part Number	EMJ04APB22
Rated voltage, V_{rated}	200 V
Rated voltage, I_{rated}	2.8 A
Rated speed, n_{rated}	3000 rpm
Rated torque, T_{erated}	1.27 Nm
Stator resistance, R_s	2.35 Ω
D-axis inductance, L_d	8.721mH
Q-axis inductance, L_q	8.721mH
Inertia, J	3.1×10^{-5} kg·m^2
Damping, B	5.3×10^{-5} Nms
PM flux linkage, ψ_f	0.0617 Wb
Number of pole pairs	4

3.2 Simulation Model of FOC of PMSM

Since the PMSM used for simulation is a surface-mounted PMSM, as mentioned before, the I_d=0 control is equivalent to MTPA. In this simulation model, I_d=0 combined with SVPWM have been applied to achieve the FOC of PMSM.

3.2.1 PI controller tuning for current loop

Substitute Equation (8) into Equation (7), can obtain the equation below:

$$\begin{cases} \dfrac{di_{sd}}{dt} = -\dfrac{R_s}{L_d} i_{sd} + \dfrac{L_q}{L_d}\omega_e i_{sq} + \dfrac{u_{sd}}{L_d} \\ \dfrac{di_{sq}}{dt} = -\dfrac{R_s}{L_q} i_{sq} - \dfrac{1}{L_q}\omega_e\left(L_d i_{sd} + \psi_f\right) + \dfrac{u_{sq}}{L_q} \end{cases} \tag{23}$$

Through Laplace transformation, applying the PI controller for current control, the equation for *d*- and *q* -axis voltage will be:

$$\begin{cases} u_{sd}{}^{*} = \left(K_{pd} + \dfrac{K_{id}}{s}\right)\left(i_{sd}{}^{*} - i_{sd}\right) - \omega_e L_q i_{sq} \\ u_{sq}{}^{*} = \left(K_{pq} + \dfrac{K_{iq}}{s}\right)\left(i_{sq}{}^{*} - i_{sq}\right) + \omega_e\left(L_d i_{sd} + \psi_f\right) \end{cases} \tag{24}$$

The zero of the PI controller block equals to the pole of the simplified filter model $\dfrac{1}{R_s + sL_{dq}}$ and the current controller bandwidth can be made to be 1/10 of the switching frequency. The parameters of the current controller can be calculated as:

$$\begin{cases} K_{pdq} = \omega_B L_{dq} = 2\pi f_{sw} L_{dq} / 10 \\ K_{idq} = \omega_B R_s = 2\pi f_{sw} R_s / 10 \end{cases} \tag{24}$$

3.2.2 PI controller parameter tuning for speed control

For PMSMs, the mechanical equations are shown as follows:

$$\begin{cases} J\dfrac{d}{dt}\omega_m = T_e - T_L - B\omega_m \\ T_e = \dfrac{3}{2} p\left[\psi_f i_{sq} + \left(L_d - L_q\right) i_{sd} i_{sq}\right] \end{cases} \tag{25}$$

If considering the inner loop fully following and with no load torque condition with $T_L = 0$ and $i_{sd} = 0$, the equation above can be converted into:

$$\frac{\omega_m(s)}{i_{sq}(s)} = \frac{\frac{3}{2} p\psi_f}{Js + B} \tag{26}$$

Similar, the PI controller for speed loop can be obtained:

$$\begin{cases} K_p = \dfrac{J 2\pi f_{sw} / 10}{\dfrac{3}{2} p\psi_f} \\ K_i = \dfrac{B}{J} K_p = \dfrac{B 2\pi f_{sw} / 10}{\dfrac{3}{2} p\psi_f} \end{cases} \tag{27}$$

3.2.3 Simulation Diagram for FOC of PMSM

From Fig. 1.7, the simulation model of FOC of PMSM in MATLAB/Simulink is built as Fig. 3.1. The simulation model consists of the function subsystem blocks including PI controller block, reference transformation block, SVPWM block, inverter block and PMSM. Through PI speed controller, the speed controller outputs the reference of *q*-axis current. Then the current PI controller outputs *dq*-axis reference voltages. Through inverse park transformation, *abc* frame reference voltages are obtained, and they can be the input of SVPWM block to generate the PWM switching signals that drive the PMSM.

The SVPWM block is shown as Fig. 3.2,

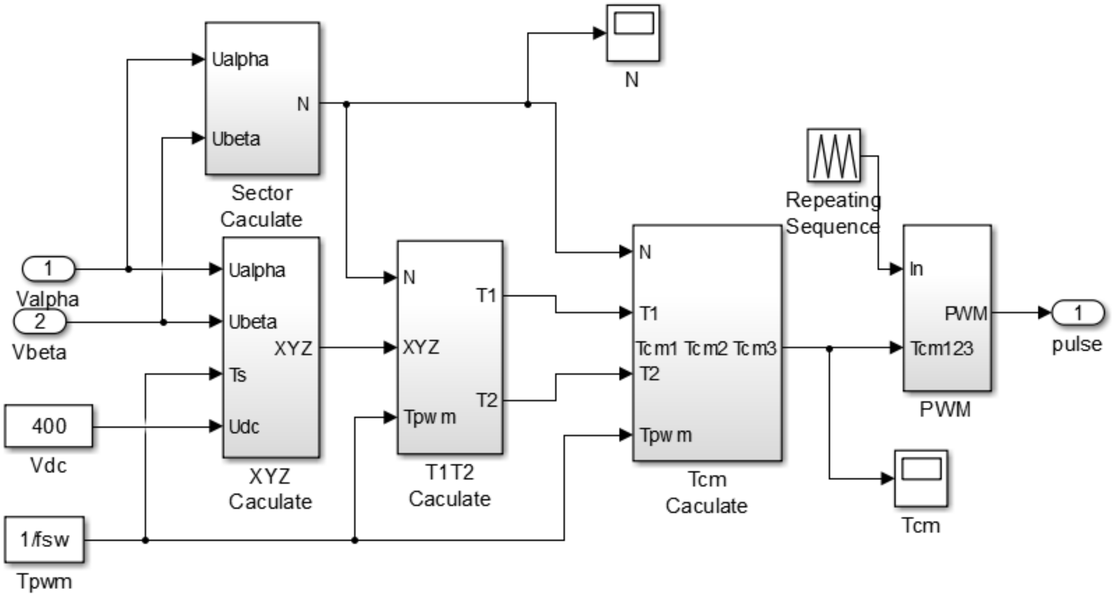

Fig. 3.2. Diagram of SVPWM block.

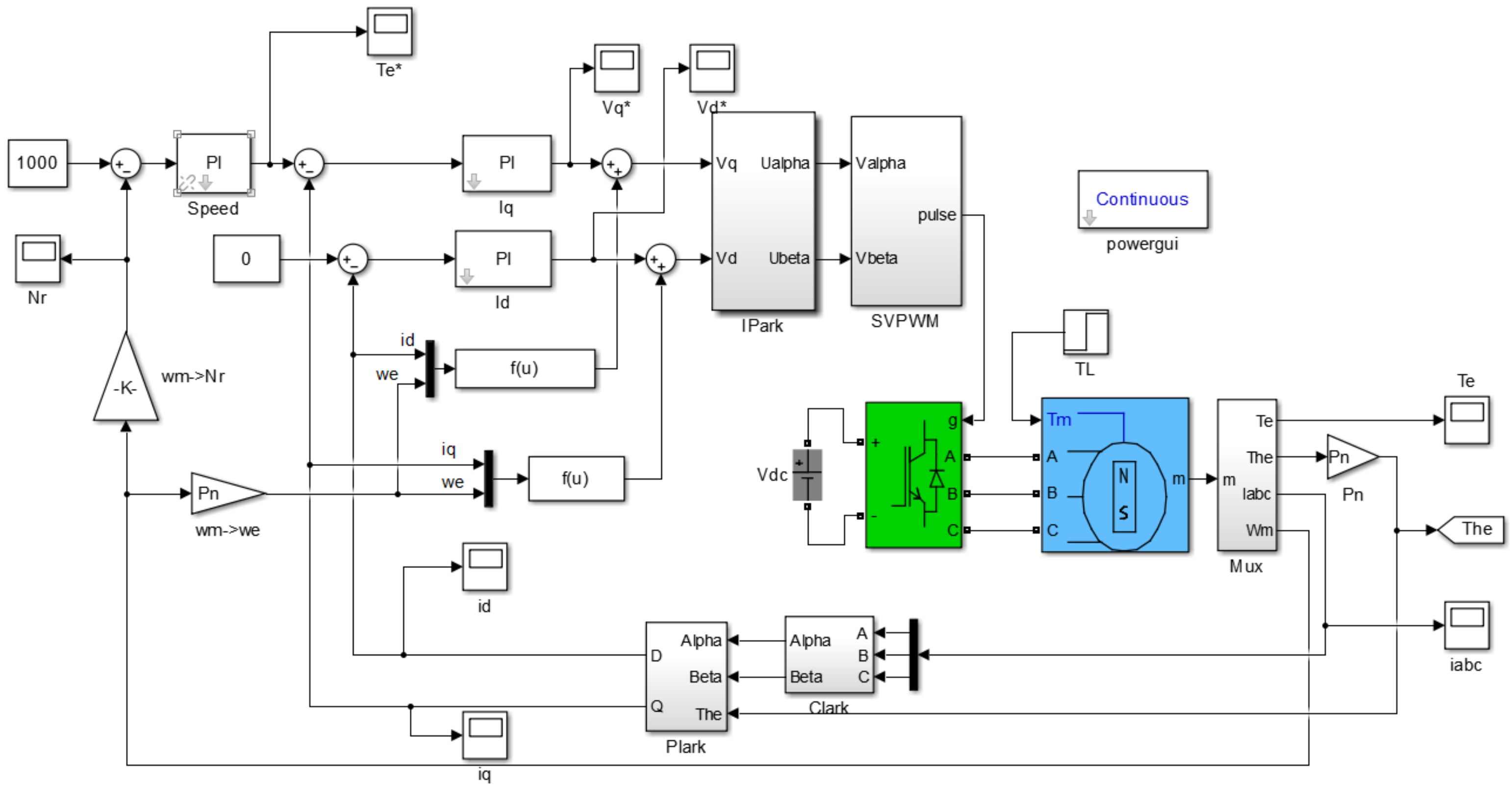

Fig. 3.1. Simulation model of FOC of PMSM, I_d=0 control

3.3 Simulation model of DTC of PMSM

Figure 3.3 shows the conventional DTC of PMSM simulation model in MATLAB/Simulink. The stator flux linkage reference is set to be 0.078 *Wb*. Since the PMSM is surface PMSM, it will satisfy the requirement to keep the torque increases with the increase of load angle. Furthermore, the band width of hysteresis controller for flux is 0.004 *Wb*, which depends on the accuracy requirement for control performance, which can also be adjusted. The bandwidth of hysteresis controller for torque is 0.01 *Nm*.

Figure 3.4 shows the calculation of α- and β-axis stator flux linkages.

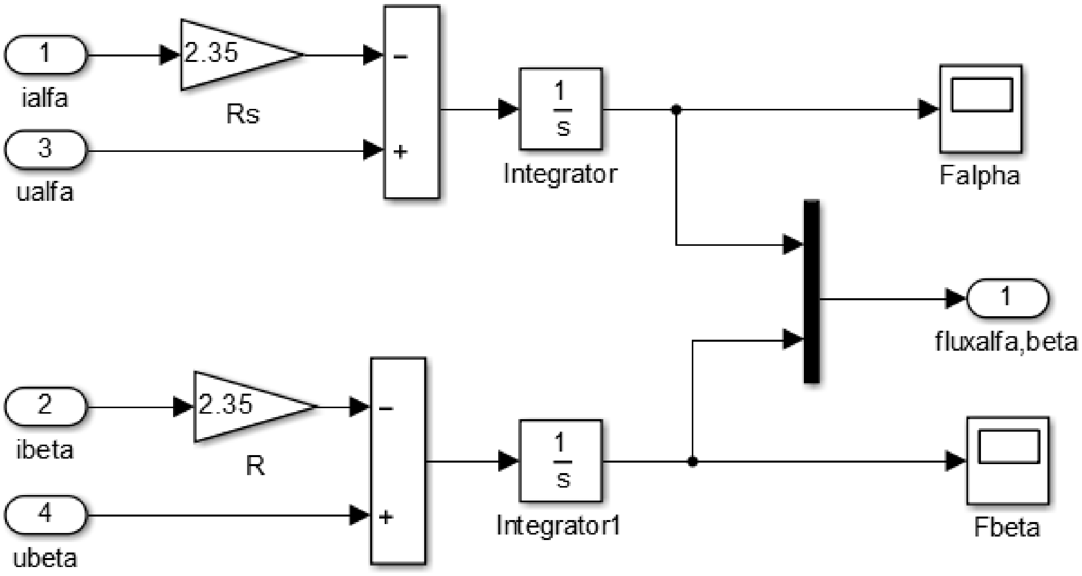

Fig. 3.4. α- and β-axis stator flux linkages calculation block.

As aforementioned, the sector can be obtained through the α- and β-axis stator flux linkages. This can be achieved in s-function. Then combining with the outputs from flux and torque regulators, switching signals can be calculated in the switching table calculation block, which shows below as Fig. 3.5.

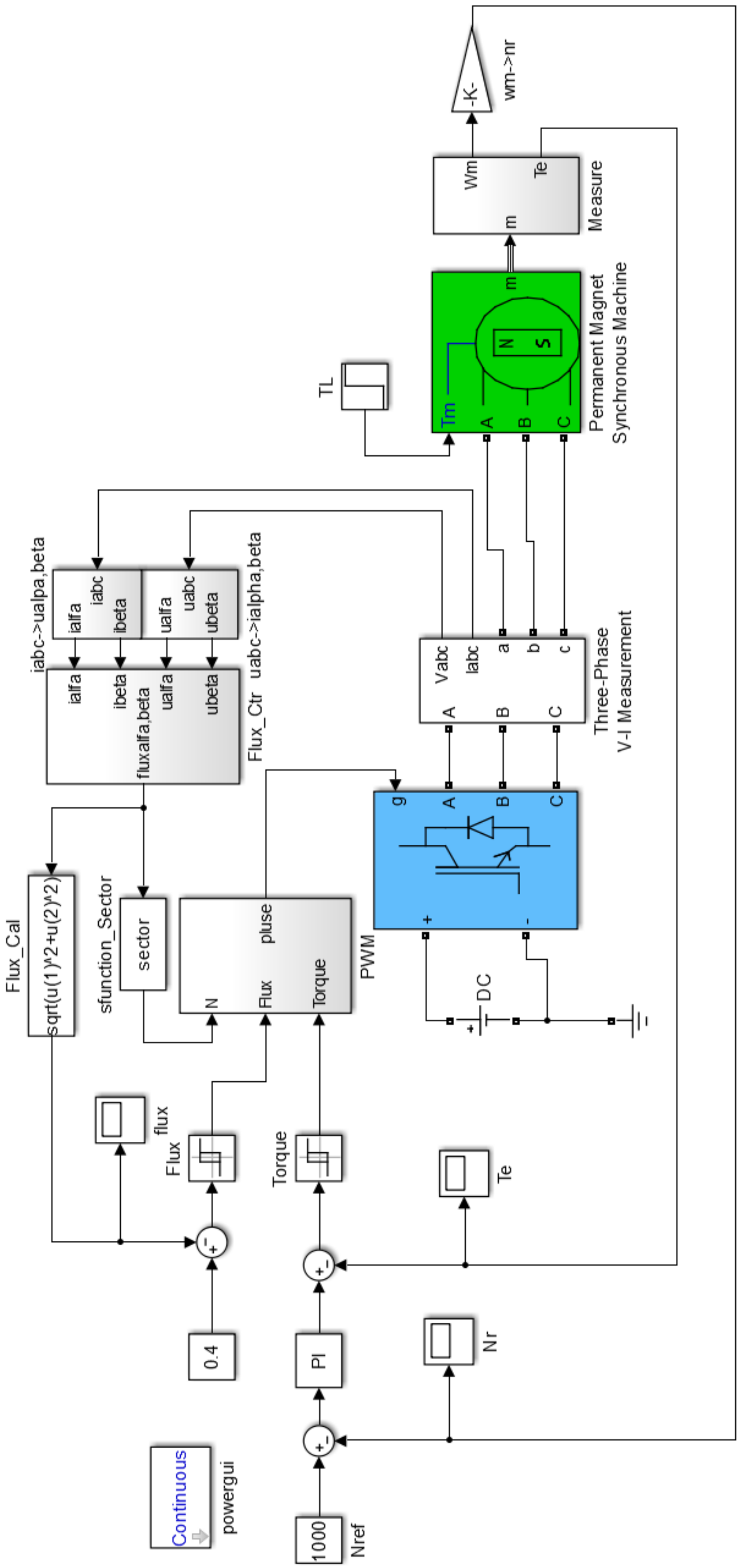

Fig. 3.3. Diagram of conventional DTC of PMSM.

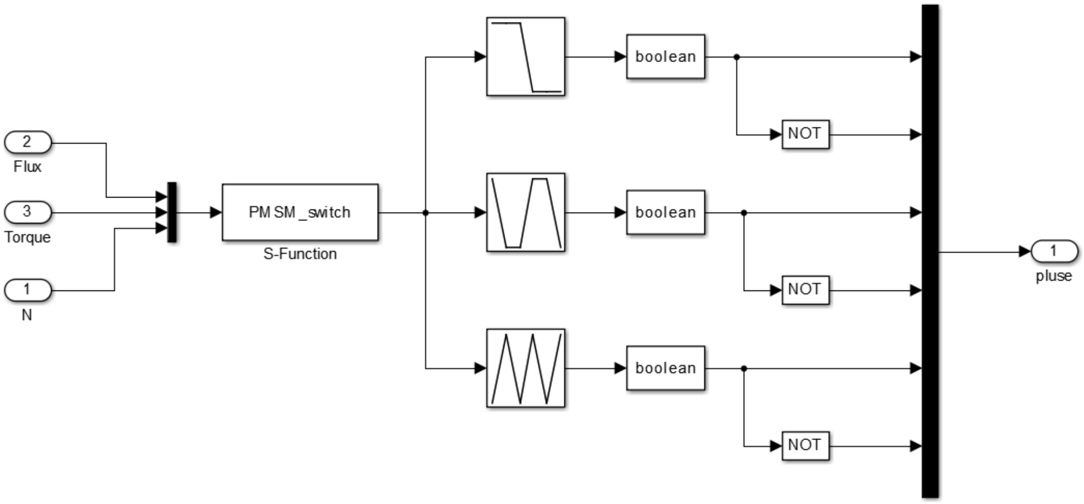

Fig. 3.5. Switching table calculation block.

Figure 3.6. shows the actual stator flux trajectory from the simulation. It is similar with Fig. 2.8, which is also a circle with bandwidth. As mentioned before, the bandwidth is changed by adjusting the bandwidth of hysteresis controller. The amplitude of the α- and β-axis stator flux linkages are the reference given for the stator flux linkages.

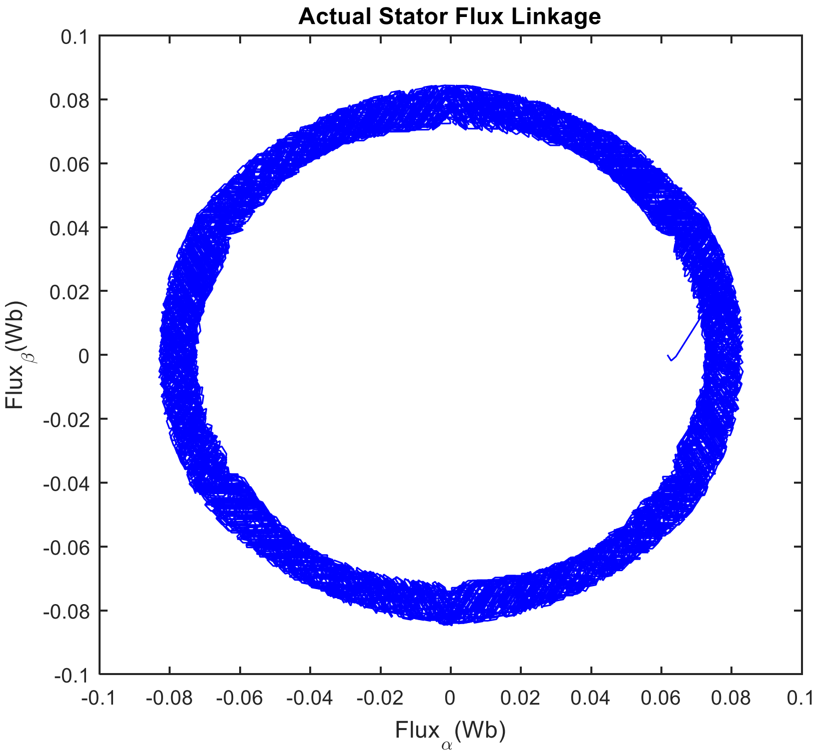

Fig. 3.6. Actual stator flux trajectory for DTC of PMSM.

3.4 Simulation Results and Analysis

The simulations were justified to obtain comparative results of FOC and DTC. The model runs at discrete mode with 100kHz sampling frequency, and the switching frequency is 10 kHz. There are two methods applied to compare the dynamic response and steady-state performance of FOC and DTC.

The first method is to make the speed reference continuously change. Here, the speed reference is generated by a function signal with different ramp. Also, the load torque is step changed from 0 Nm to 1 Nm at 0.1 second. Fig. 3.7. shows the speed response comparison of FOC and DTC, here the FOC requires more time to reach the reference point, but DTC follows the speed reference much faster.

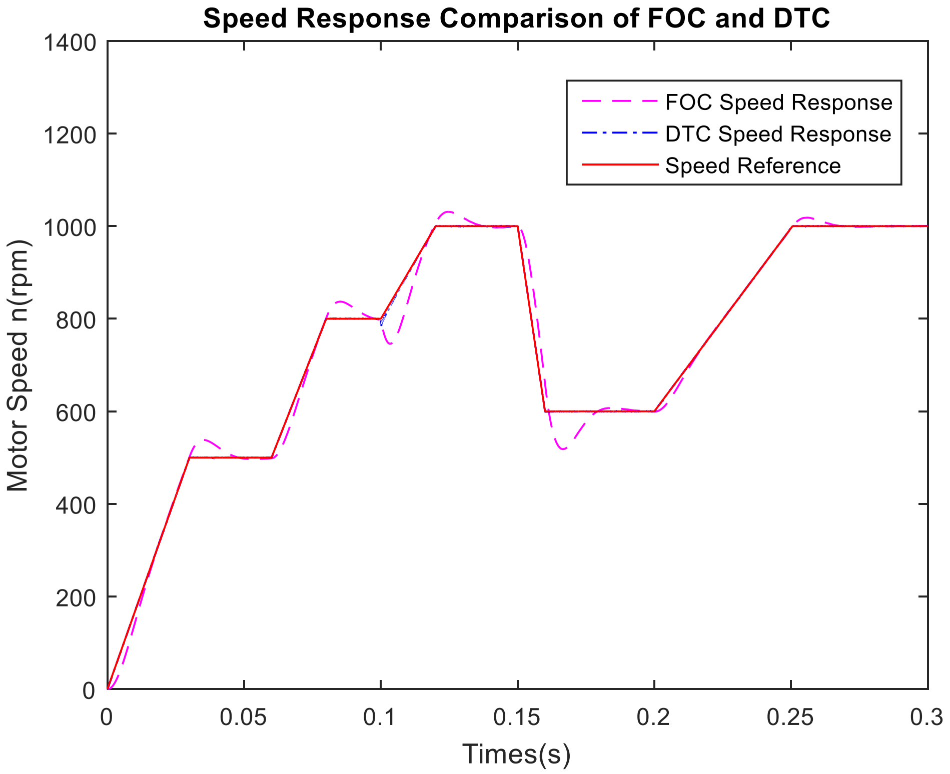

Fig. 3.7. The speed response comparison of FOC and DTC with variable speed reference.

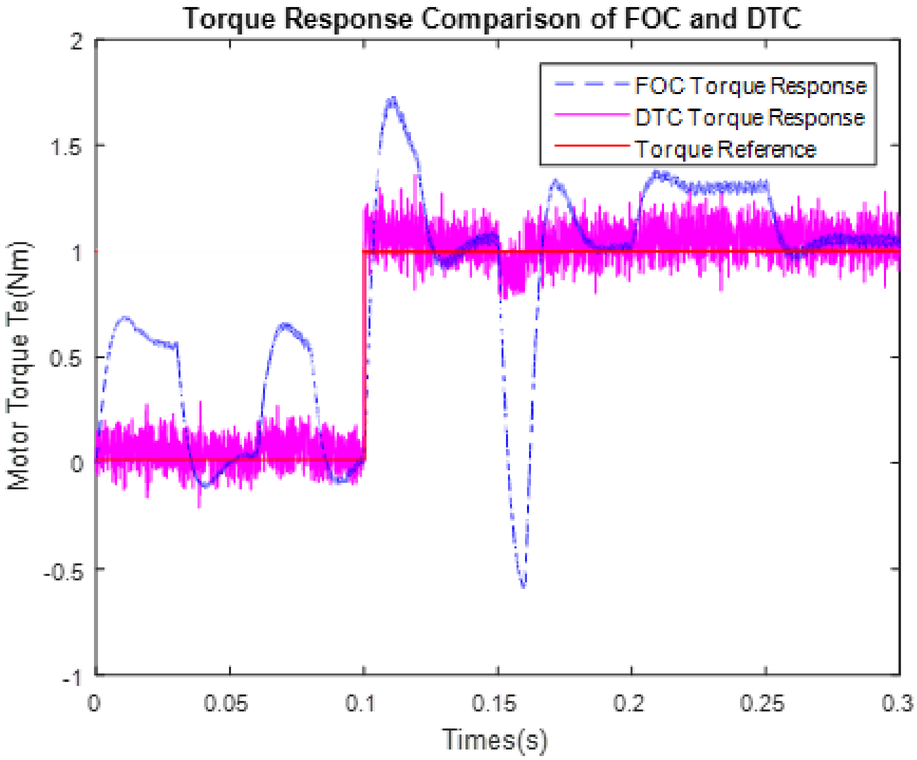

Fig. 3.8. The torque response comparison of FOC and DTC with variable speed reference.

Figure 3.8. shows the torque response comparison of FOC and DTC. Although DTC still has a faster torque response than FOC, for the steady-state condition, the torque ripple of DTC is much larger than that of the FOC. Which is same as the conclusion from Table. 2.1.

The second method is to fix the load condition, which is first with no load, then with full load, at variable speed references to make the comparison of FOC and DTC. Variable speed references taken are: 500 rpm,800 rpm and 1000rpm. The load is applied at 0.1 second. Table. 3.2. shows the comparison between the time required to attain steady state and steady state torque ripple for FOC and DTC control with reference to results shown in Fig. 3.9. to Fig. 3.14.

Table. 3.2. Comparison at variable speed with full load.

Speed Reference	Type of Control	Time to attain steady state (*ms*) (no load)	Time to attain steady state (*ms*) (full load)	Steady state torque ripple (%)
500 rpm	FOC	6.61	14.4	3.69
	DTC	0.08	2.1	20.92
800 rpm	FOC	6.42	12	3.14

	DTC	0.14	0.3	20.92
1000 rpm	FOC	6.51	10.8	2.76
	DTC	0.08	0.3	19.85

The conclusions drawn from Table. 3.2 are similar as Table. 2.1. From Fig. 3.9. to Fig. 3.14, the comparisons between FOC and DTC on speed and torque reference are presented as follows: it is very clear that DTC has faster dynamic response for speed and torque compared with FOC; regardless of load or no load. This proves that DTC has the advantage of fast dynamic response. However, the limitation of DTC is the steady state behavior. It has a larger torque ripple compared to FOC. Therefore, in order to optimize the DTC torque ripple, a torque ripple analysis is needed.

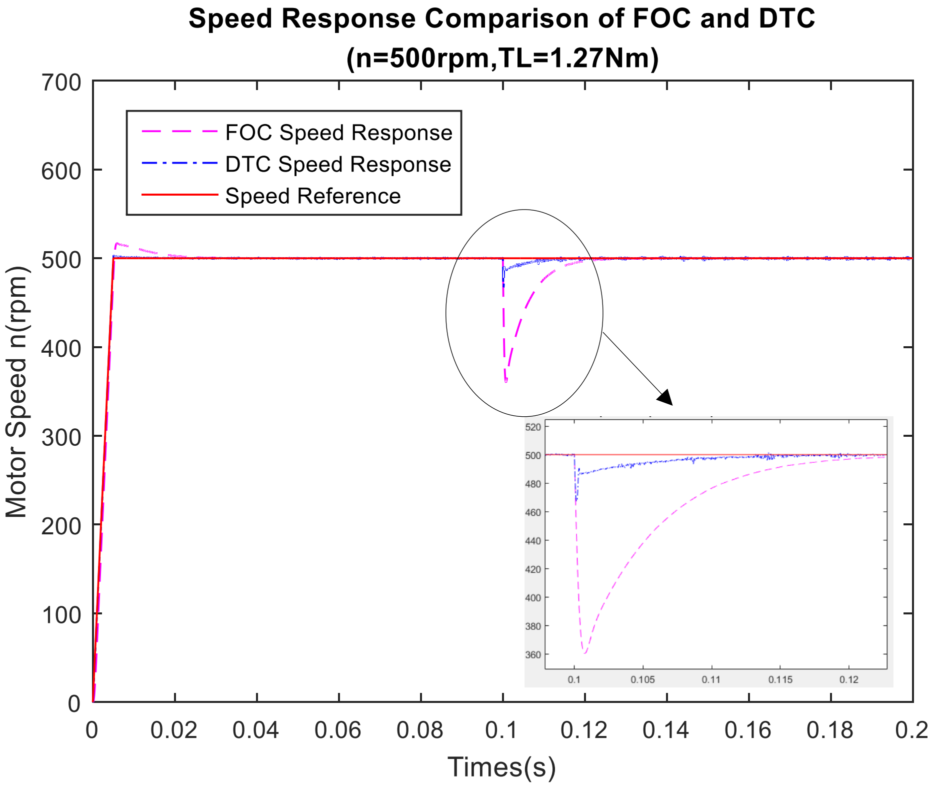

Fig. 3.9. Speed response comparison of FOC and DTC at 500 rpm.

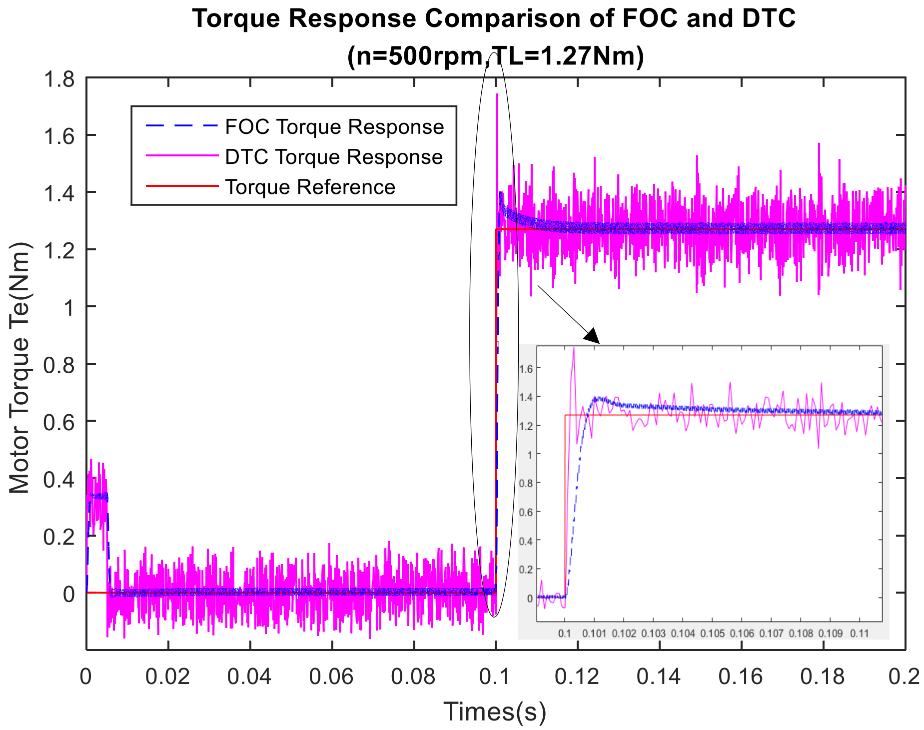

Fig. 3.10. Torque response comparison of FOC and DTC at 500 rpm.

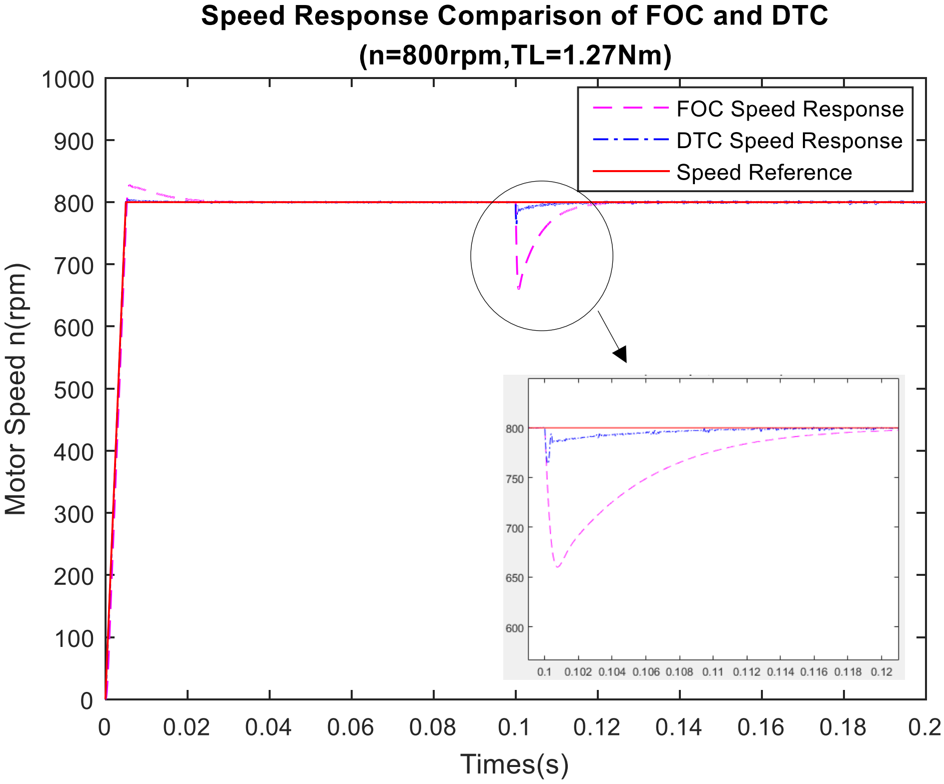

Fig. 3.11. Speed response comparison of FOC and DTC at 800 rpm.

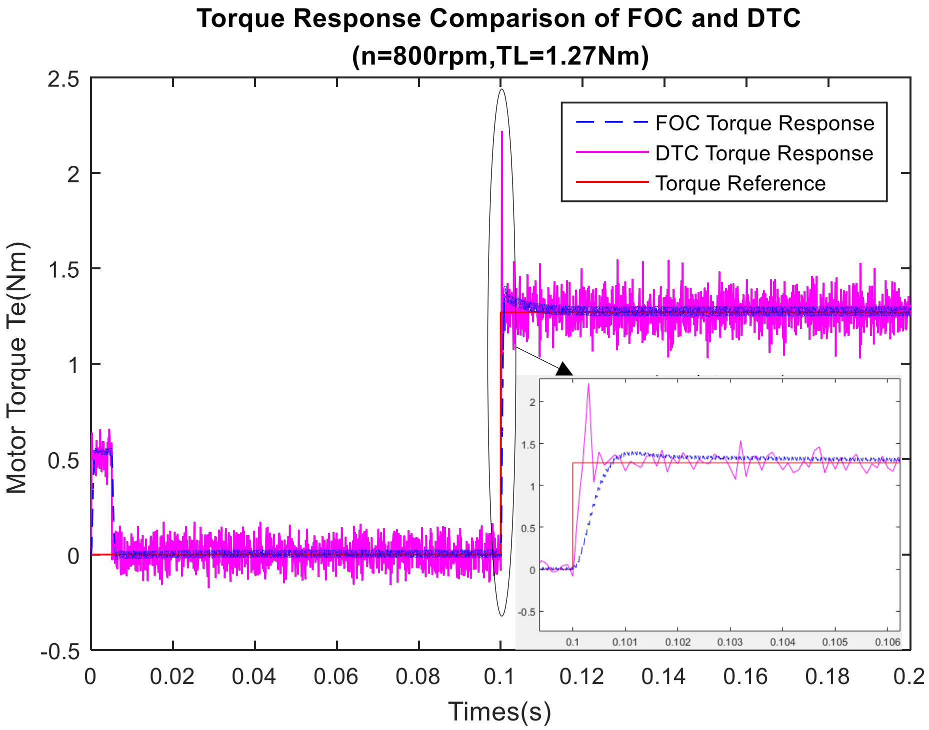

Fig. 3.12. Torque response comparison of FOC and DTC at 800 rpm.

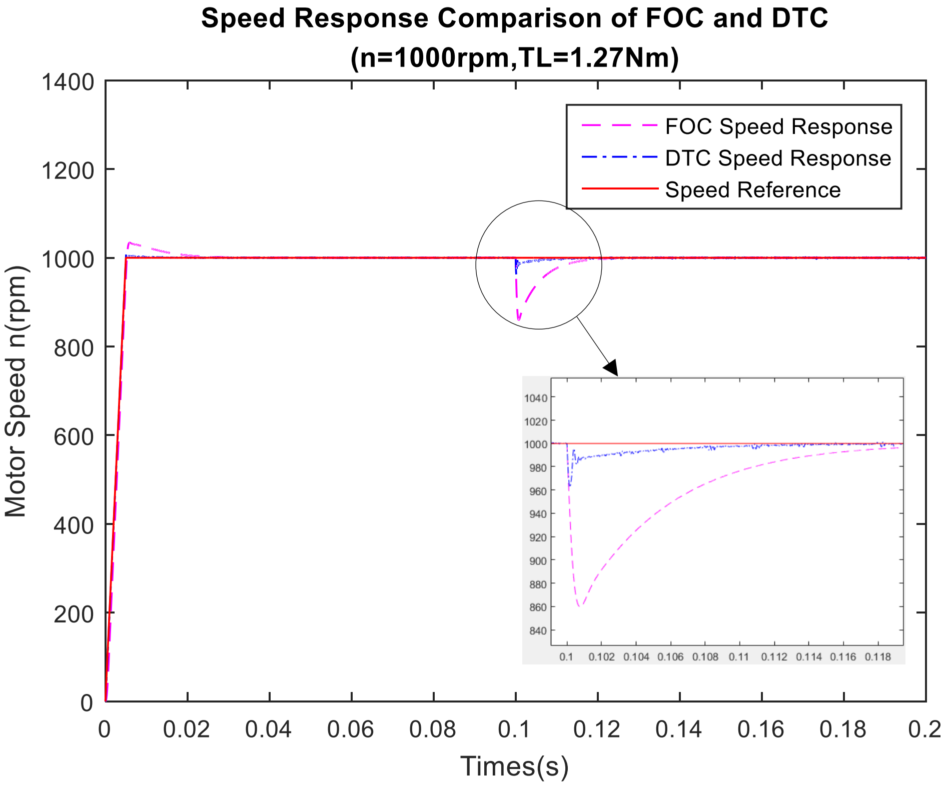

Fig. 3.13. Speed response comparison of FOC and DTC at 1000 rpm.

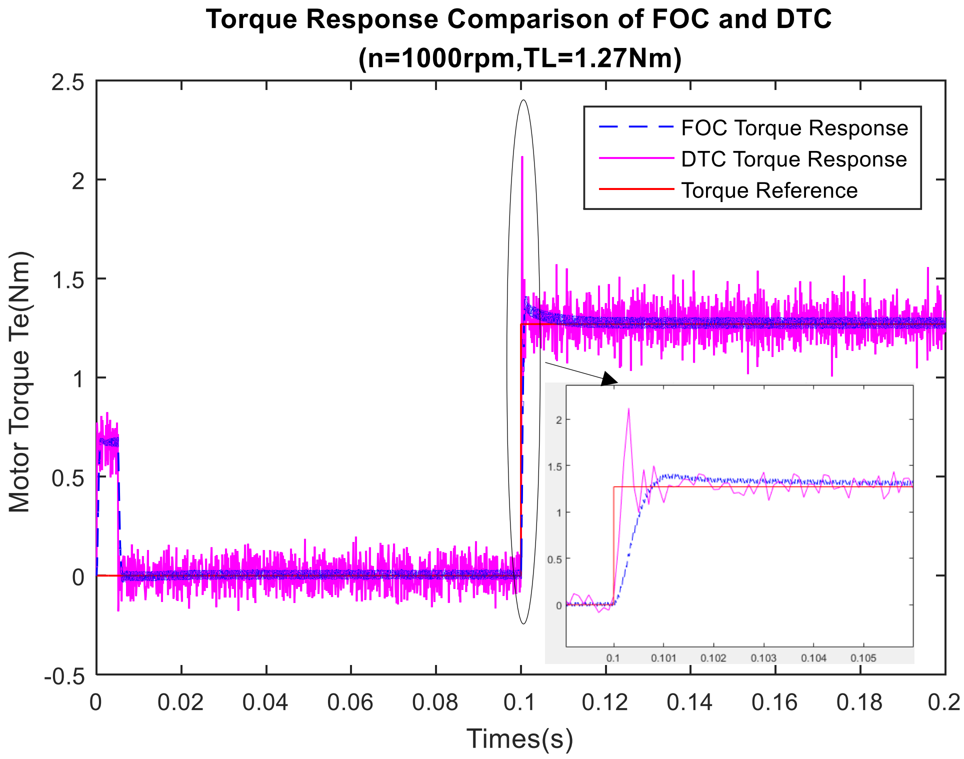

Fig. 3.14. Torque response comparison of FOC and DTC at 1000 rpm.

Chapter 4

Optimization of Conventional DTC for PMSMs Using GaN-based Inverter

This chapter focuses on the optimization of conventional DTC for PMSMs to minimize the torque ripple. First, the torque ripple analysis is presented to explain how the bandwidth of hysteresis controller will affect on the steady state behavior. Then, based on the results an optimization solution for torque ripple minimization has been presented. In order to achieve the optimization method, an innovative inverter based on Gallium Nitride (GaN) has been introduced. Next, for feasible hardware implementation of DTC, DTC-SVM has been proposed and MATLAB/Simulink software is presented to achieve constant switching frequency and torque ripple minimization using SVPWM.

4.1 Torque Ripple Analysis based on Conventional DTC

For control of stator flux linkage and electromagnetic torque, hysteresis controllers are utilized in the conventional DTC. However, the control performance of these kind of controllers is affected by the bandwidth of the hysteresis controller. As the result of that, it is necessary to analyze the torque ripple in DTC based on the hysteresis bandwidth. From [29], a smaller bandwidth hysteresis controller can lead to less distortion and a smaller torque ripple but will also lead higher switching frequency. The simulation results from the previous chapter show two important facts: The bandwidth of the stator flux linkage hysteresis controller is 0.004 *Wb* and the bandwidth of the torque hysteresis controller is 0.01 *Nm*. If the bandwidth of the hysteresis controllers can be decreased, the torque ripple can be further reduced.

In conventional DTC, until the status of the hysteresis controllers is updated, the voltage vectors are applied to the inverter. Before that, remains the same from the last control cycle. Again, the simulation models of the previous chapters reveal a vital fact: the estimated stator flux magnitude and electromagnetic torque are clearly controlled by the hysteresis controller, as long as they are within the bandwidth of those hysteresis controllers. That is DTC implemented in an analog system, the switching frequency is usually varied in order to control the estimated torque on the hysteresis bands $\pm B_w$ around the reference torque T_e^*, as shown in Fig. 4.1(a). However, when the DTC is implemented in a discrete-time (digital) system, such as a DSP or an FPGA, the hysteresis band as well as the sampling frequency affects system performance [41], which can be seen from Fig. 4.1(b). In order to make digital DTC systems perform the same as the analog DTC system a high sampling frequency is desired to achieve fast and precise control. Additionally, a high switching frequency is also required to implement DTC in the digital system. These are also done to reduce the torque ripple through adjustment of the bandwidth of the hysteresis controllers. For example, it was reported that the sampling frequency of the commercial DTC drive product ACS600 reached 40 kHz [17].

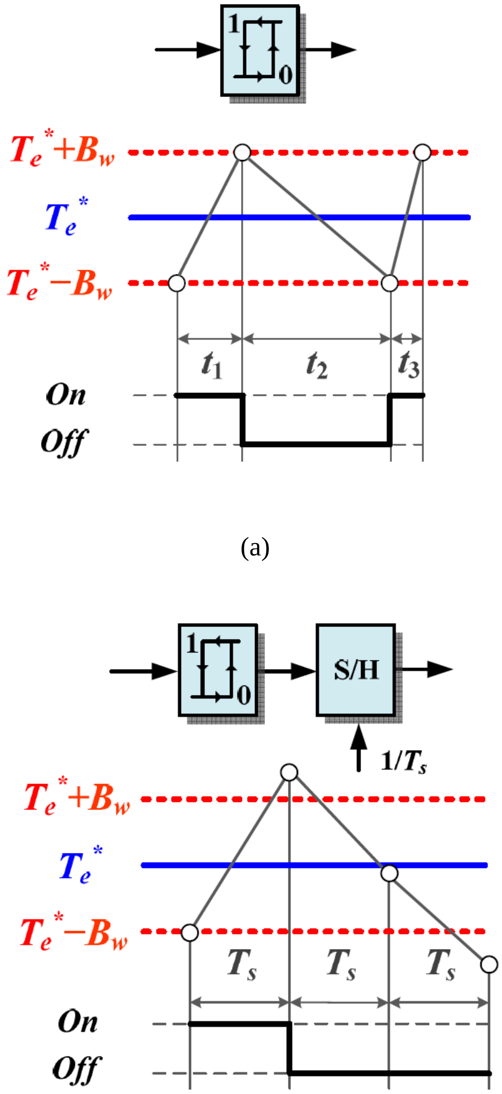

(a)

(b)

Fig. 4.1. Comparison of the switching modes of the hysteresis torque controller in (a) an analog DTC system and (b) a discrete-time DTC system and the resulting torque ripples [6].

Although the frequency is normally smaller than the sampling frequency, it can be one third of it or even less, for a high sampling frequency, the switching frequency is increased to reduce the torque ripple of the system. In conventional DTC, the voltage vectors are executed in the entire switching cycle, which is the main cause of torque and flux ripples. The ripples will be even larger when the switching frequency is lower because T_s becomes larger. Therefore, for a DTC-based PMSM drive system, the lower sampling frequency, the larger the torque ripples.

Figure 4.2. compares the stator flux level in the MATLAB/Simulink simulation for a PMSM drive system controlled by the conventional DTC with 100 kHz and 1 MHz sampling frequencies. Figure 4.3. compares the torque ripple level for the same operation condition. From the comparison results, it is very clear that a higher sampling frequency will effectively minimize the stator flux linkage magnitude ripple. It also further suppresses the torque ripple of PMSMs drive system controlled by the conventional DTC.

A higher sampling frequency results in better control performance of conventional DTC. Therefore, it is also necessary to increase the switching frequency to accompany this change. Figure 4.4. compares the difference of the switching frequency when the sampling frequency is 100 kHz and 1 MHz. The results validate that a higher sampling frequency will require higher switching frequency. Therefore, both a high sampling frequency and a high switching frequency are needed to achieve torque ripple minimization for the PMSM drive systems controlled by conventional DTC.

Applying high sampling frequency and switching frequency to DTC is limited by the hardware capabilities. First, it requires a high operation frequency digital controller with high sampling capability. This achieves a smaller sampling time T_s and reduces the calculation time required to generate gate signals to the inverter that drives the PMSMs. Second, an inverter that can operate at high switching frequency is also needed to receive the gate signals. If these two conditions are satisfied, the torque ripple of the conventional DTC can be further reduced based on the analysis above.

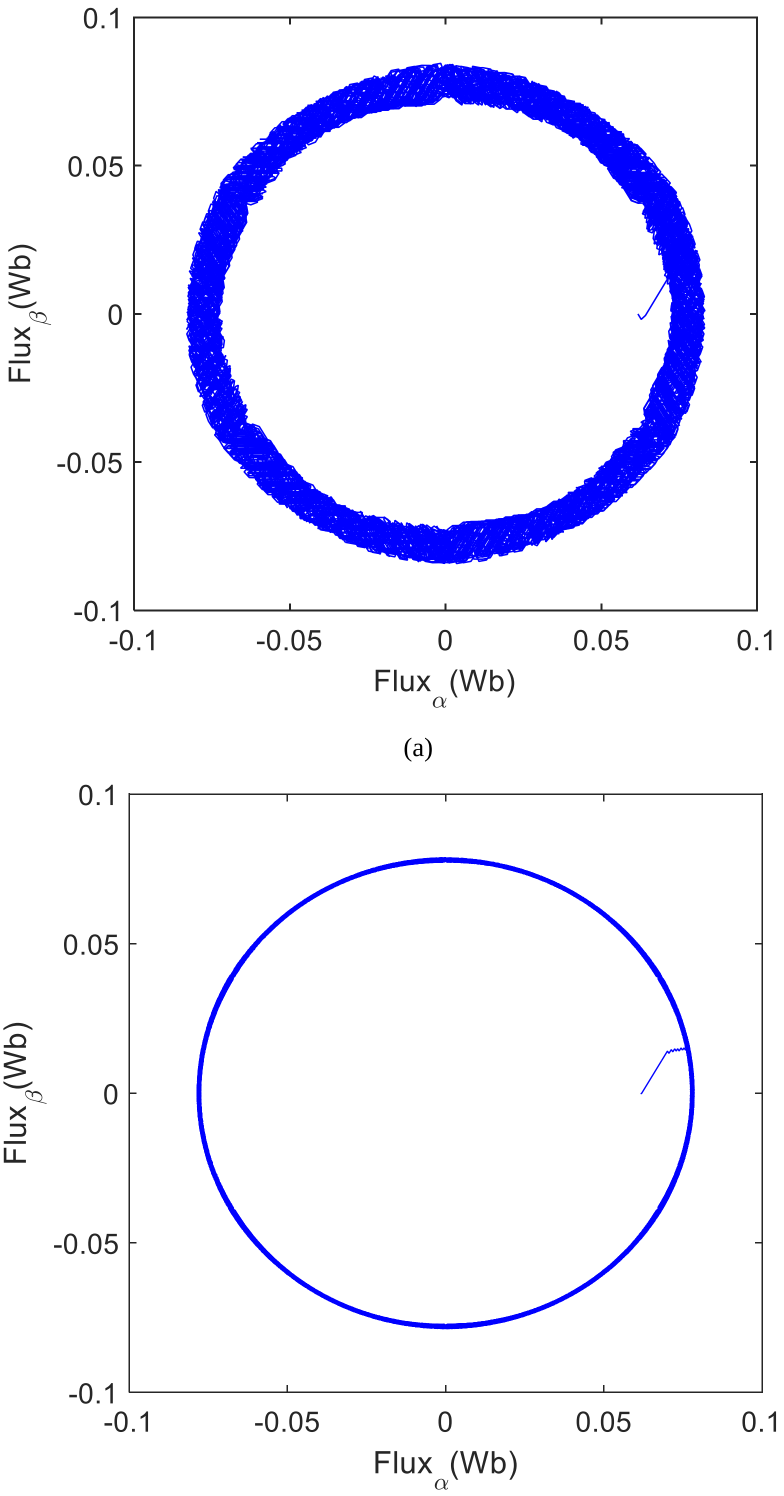

(a)

(b)

Fig. 4.2 Trajectories of the stator flux vector in the stationary reference frame: (a) T_s=10*us*; (b) T_s=1*us*.

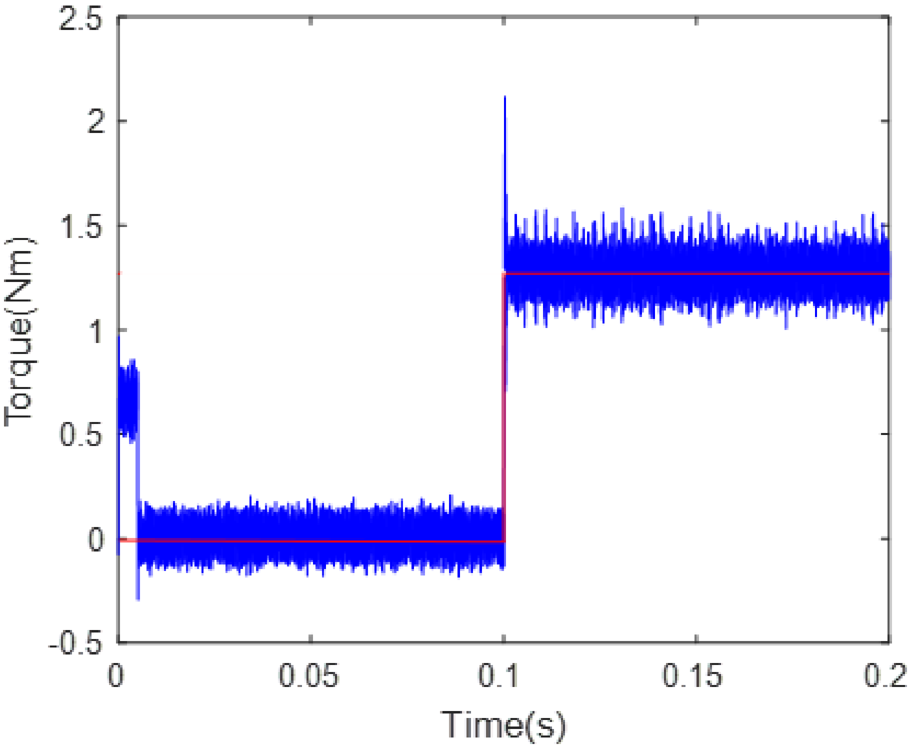

(a)

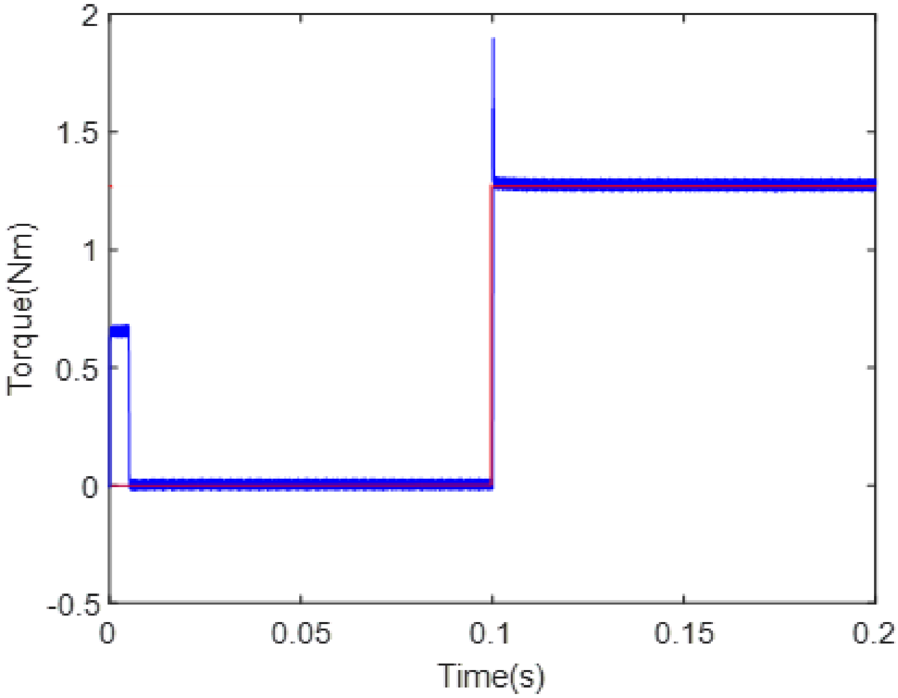

(b)

Fig. 4.3. Waveforms of the electromagnetic torque:

(a) T_s=10*us*; (b) T_s=1*us*.

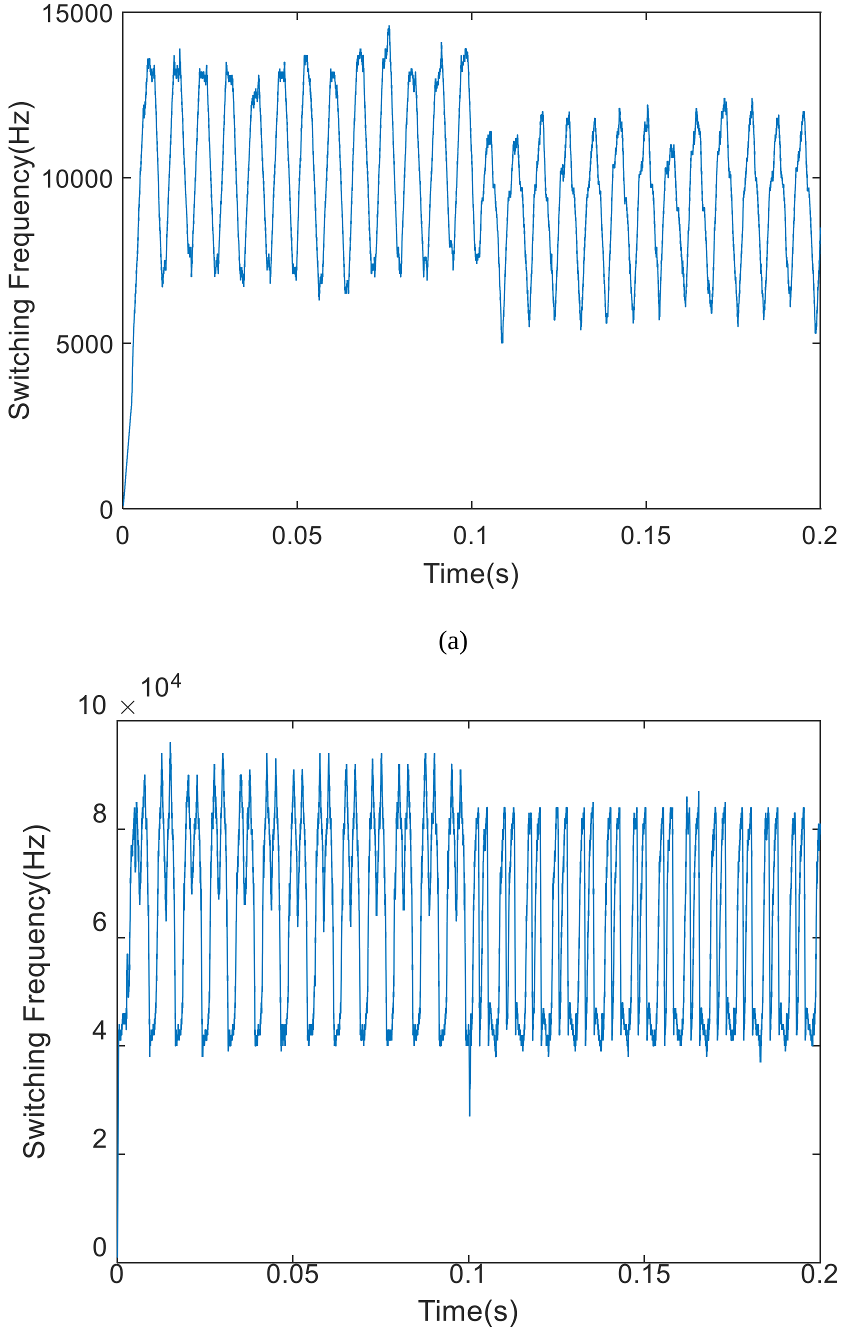

(a)

(b)

Fig. 4.4. Switching frequency comparison:
(a) T_s=10*us*; (b) T_s=1*us*.

4.2 Introduction of Gallium Nitride (GaN) based inverter

The semiconductor based IGBTs currently used for Electric and Hybrid Vehicles are usually limited by the switching frequency. This proves to be a burden if the conventional DTC needs to be applied to the PMSM drive systems with high sampling frequency and switching frequency. GaN powered devices are becoming an alternative to Silicon based IGBTs. This new technology enables Innverters to be designed with higher frequencies and efficiencies than conventional Si devices. A comparison bewteen Si, Silicon Carbide (SiC) and GaN power devices is shown as Fig. 4.5. SiC and GaN both belongs to wide bandgap (WBG) devices, which allows for high-frequency, high-efficiency power electronics [47]. The higher breakdown field of a WBG semiconductor enables devices to be optimized with thinner drift regions. This results in power devices with lower specific ON-resistance. The high mobility of GaN further reduces the ON-resistance allowing a smaller die size to achieve a given current capability. Therefore, there is lower input and output capacitances. Higher saturation velocity and lower capacitances enable faster switching transients. Overall, the material properties of WBG semiconductors results in a device with lower ON-resistance and switching losses than a Si device with comparable voltage and current capabilities [43-47]. Though SiC excels in high-temperature applications, the material characteristics of GaN are superior in high-efficiency, high-frequency converters. GaN powered devices rated up to 650 V have recently become commercially available, and GaN-based converter design has become a popular topic [47].

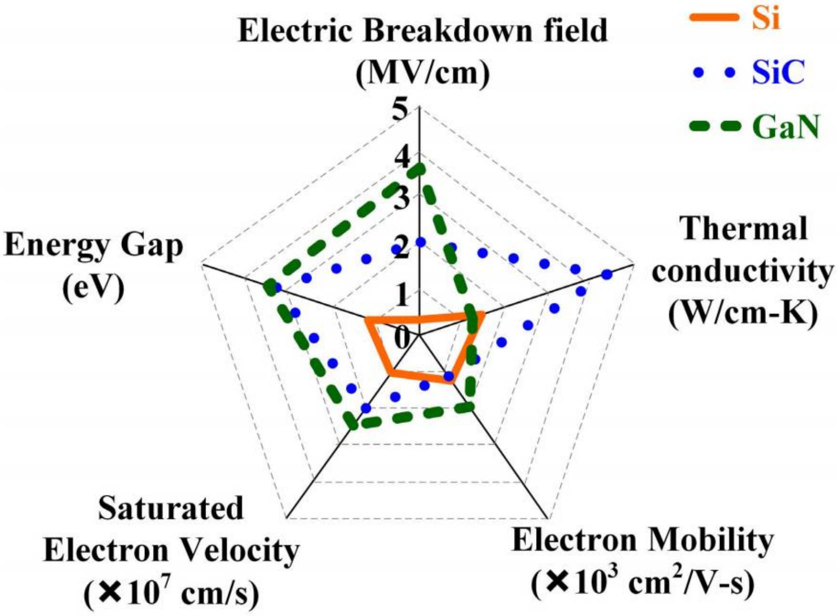

Fig. 4.5. Comparison of Si, SiC, and GaN for power semiconductor applications [43], [44].

Recently, GaN semiconductors have been introduced with nano-second speed switching time. This is combined with innovative power electronics technology leading to the switching frequency changing from 100 kHz to 2 MHz with efficiency over 95%. For applications requiring 90% efficiency, the switching frequency can be up to $100 MHz$. The maximum switching frequency is $1 GHz$. With the increase of the switching frequency, switching loss becomes an important factor that cannot be neglected. Figure. 4.6 shows how the switching loss is generated.

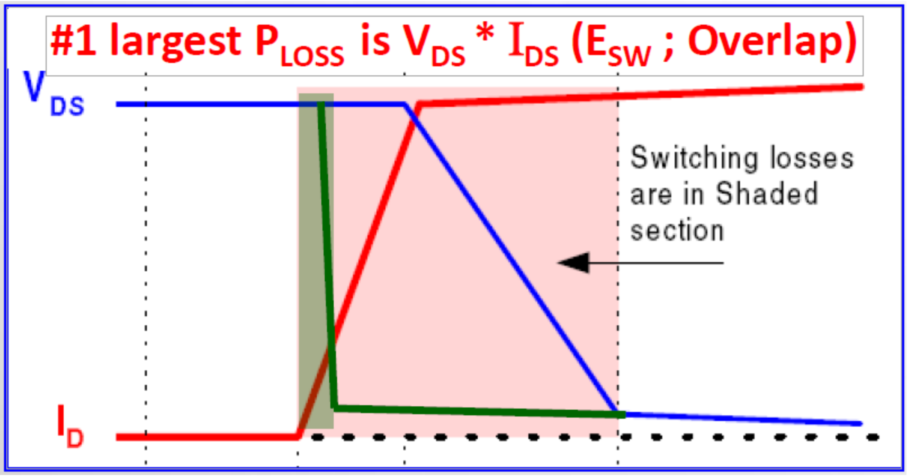

Fig. 4.6. Introduction of switching loss [48].

where V_{DS} is the Drain-to-source voltage, I_D is the drain currents.

Due to the fast switching advantage of GaN, GaN switches faster than Si/SiC MOSFETs with $\frac{dV}{dt} > 100V/ns$. That means GaN has a 4 times faster turn-on speed and about 2 times faster turn-on speed than state of art SiC MOSFET [49], which is shown below as Fig. 4.7.

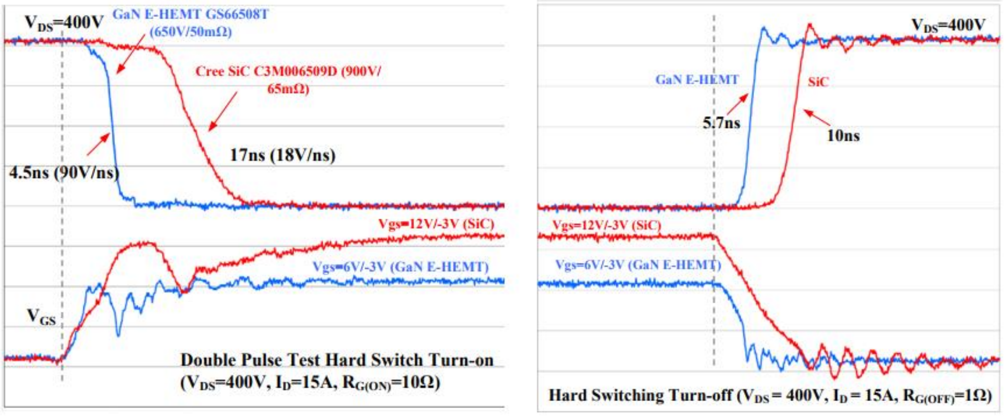

Fig. 4.7. The comparison between GaN and SiC for switching time [49].

Since the faster switching, GaN has less area under the V_{DS} - I_D curve, which will bring less switching loss to make GaN much more efficient compared with SiC. Furthermore, there is a comparison between GaN, CoolMOS and IGBT at varies frequency, which is shown as Fig. 4.8.

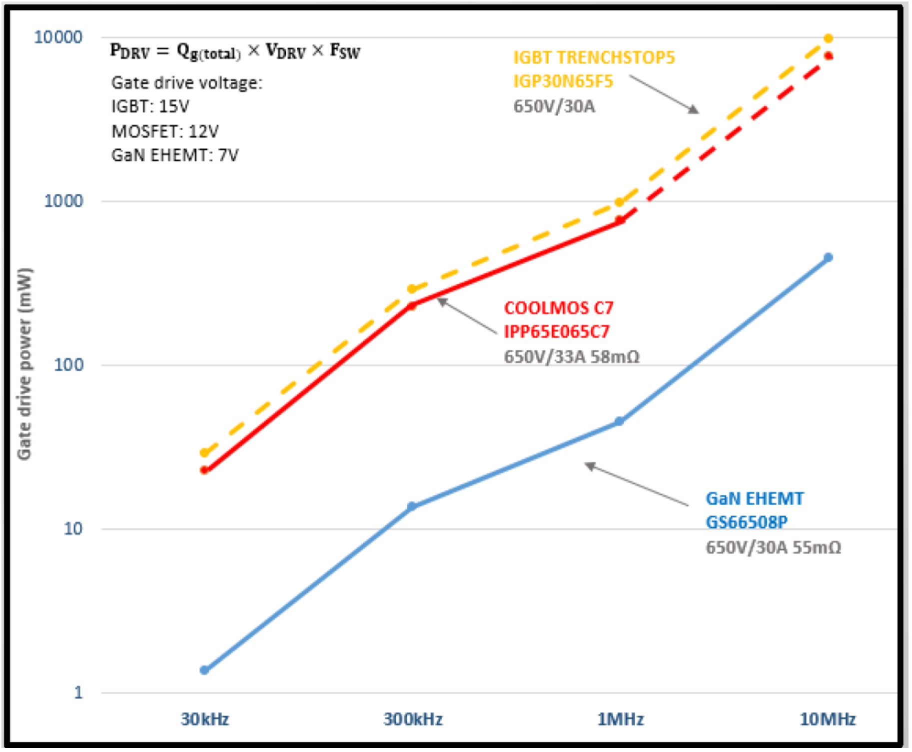

Fig. 4.8. Drive loss comparison between GaN, CoolMOS and IGBT at varies frequency [48].

Table. 4.1. shows the exact value for drive loss comparison between GaN, CoolMOS and IGBT at various frequencies.

Table. 4.1. Drive loss comparison between GaN and CoolMOS at varies frequency [48].

	V_{DS}	I_{DS}	R_{DSON}	$30kHz$	$300kHz$	$1MHz$	$10MHz$
GaN	$650V$	$30A$	$55m\Omega$	$1mW$	$14mW$	$46mW$	$455mW$
CoolMOS	$650V$	$33A$	$58m\Omega$	$23mW$	$230mW$	$770mW$	$7700mW$

From Table. 4.1, it can be noted that with the increase of the switching frequency, the drive loss increase. However, GaN still has the obvious dominant compared with MOSFET and IGBT, which more than 16 times lower drive loss at 1 MHz switching frequency. Since in general condition, the topology of full bridge is mostly used in the conventional inverter. There is a full bridge power loss comparison between COOLMOS, IGBT, SiC and GaN simulated using Pspice model or calculated using datasheet parameters shown below as Fig. 4.9. The inverter system is 2 kW, 400 VDC input, 240V/8.3A 60Hz output and the power factor is 0.9.

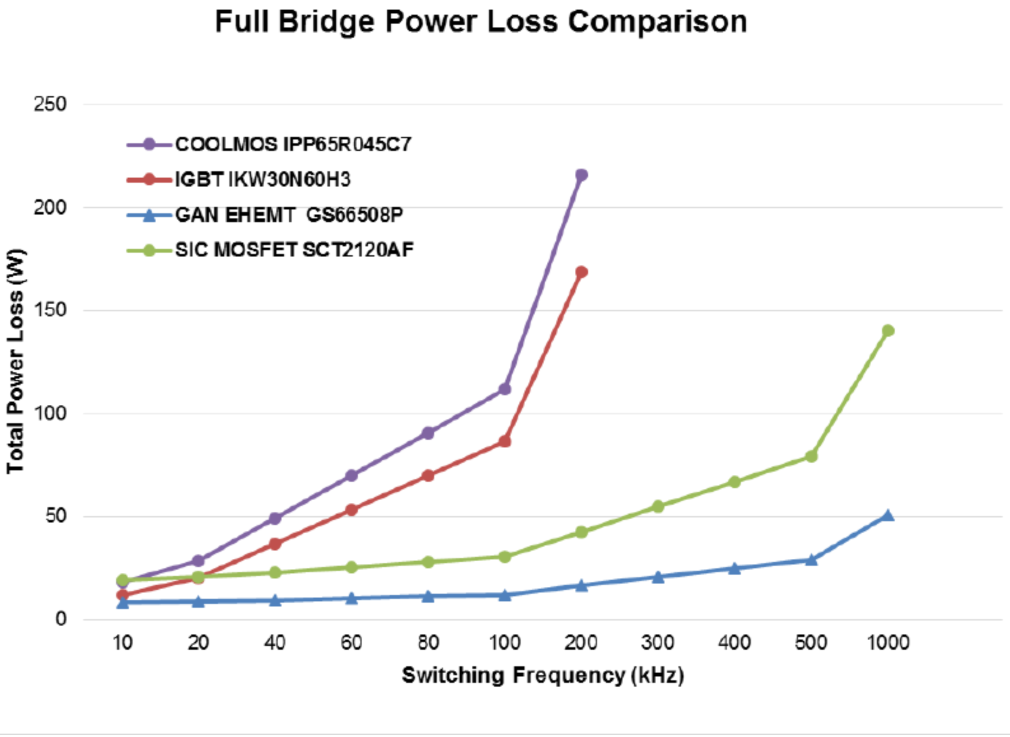

Fig. 4.9. Full bridge power loss comparison between COOLMOS, IGBT, SiC and GaN [48].

From the figures and table above, GaN shows its dominant advantages in the high switching frequency range. In order to apply conventional DTC to PMSM drive systems with high sampling frequency and switching frequency, a GaN-based inverter is required to assist to solve the limit of switching frequency for hardware implementation.

4.3 Optimization for Hardware Implementation of DTC

During the research of hardware implementation of conventional DTC, there are some key issues have been found. First of all, because of hysteresis controller, the variable switching frequency will increases the difficulty for the PWM generation, which makes it almost impossible to utilize the PWM module to generate PWM to achieve control. If using general purpose I/O port instead of PWM to achieve control, it is also not acceptable because there is no way to set a dead-band to avoid the upside and downside power switch conducting at the same time. In order to address these issues, an optimization method which combines SVPWM with conventional DTC has been applied.

4.3.1 The DTC based on SVPWM (DTC-SVM)

In the conventional DTC, the stator flux linkage amplitude $\psi_s(k)$ and phase angle $\theta(k)$ can be calculated through Clarke transformation after α- and β-axis stator voltage and current have been sampled. After a control period, the stator flux linkage amplitude becomes $\psi_s(k+1)$ and the phase angle becomes $\theta(k+1)$, with the angle between $\theta(k)$ and $\theta(k+1)$, is $\Delta\theta$. As Fig. 4.10. shows,

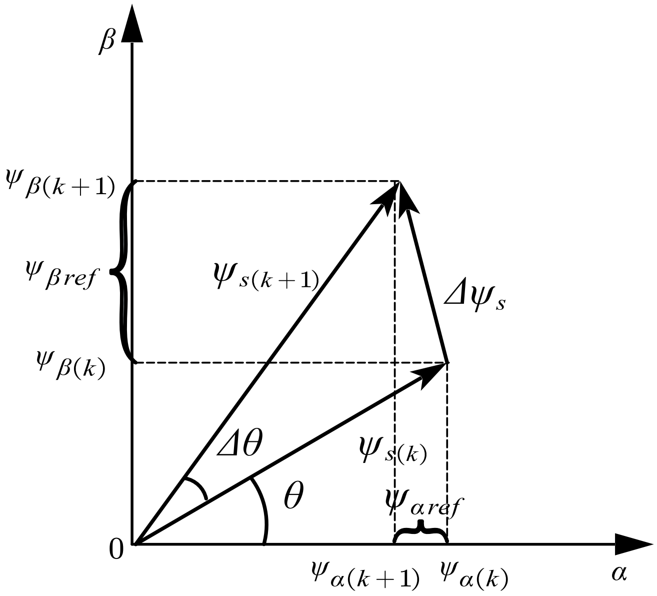

Fig. 4.10. The α- and β-axis flux vector for DTC-SVM.

It can be seen from Fig. 4.10. that:

$$\begin{cases} \psi_{\alpha(k+1)} = \psi_{s(k+1)} \cos(\theta + \Delta\theta) \\ \psi_{\beta(k+1)} = \psi_{s(k+1)} \sin(\theta + \Delta\theta) \end{cases} \tag{28}$$

$$\begin{cases} \psi_{\alpha(k)} = \psi_{s(k)} \cos(\theta) \\ \psi_{\beta(k)} = \psi_{s(k)} \sin(\theta) \end{cases} \tag{29}$$

$$\begin{cases} \psi_{\alpha ref} = \psi_{\alpha(k+1)} - \psi_{\alpha(k)} = \psi_{s(k+1)} \cos(\theta + \Delta\theta) - \psi_{s(k)} \cos(\theta) \\ \psi_{\beta ref} = \psi_{\beta(k+1)} - \psi_{\beta(k)} = \psi_{s(k+1)} \sin(\theta + \Delta\theta) - \psi_{s(k)} \sin(\theta) \end{cases} \tag{30}$$

Through Equation (30), the ψ_{ref} at α- and β-axis can be calculated. In order to compensate the error for ψ_{ref}, an equivalent voltage vector reference U_{ref} is needed. Since for the ψ_s, we have:

$$\psi_s(t) = \int \left(U_s(t) - R_s i_s(t) \right) dt \tag{31}$$

In the discrete system, through the discretization of Equation (31), it can be known that:

$$\psi_{ref} = \psi_{s(k+1)} - \psi_{s(k)} = \left(U_{s(k)} - R_s i_{s(k)} \right) T_s \tag{32}$$

Then, the α- and β-axis voltage vector can be obtained:

$$\begin{cases} U_{\alpha ref} = U_{\alpha(k)} = \psi_{\alpha ref} / T_s + R_s i_{\alpha(k)} \\ U_{\beta ref} = U_{\beta(k)} = \psi_{\beta ref} / T_s + R_s i_{\beta(k)} \end{cases} \tag{33}$$

Substituting Equation (30) into Equation (33) to obtain Equation (34) as below:

$$\begin{cases} U_{\alpha ref} = U_{\alpha(k)} = \left(\psi_{s(k+1)} \cos(\theta + \Delta\theta) - \psi_{s(k)} \cos(\theta) \right) / T_s + R_s i_{\alpha(k)} \\ U_{\beta ref} = U_{\beta(k)} = \left(\psi_{s(k+1)} \sin(\theta + \Delta\theta) - \psi_{s(k)} \sin(\theta) \right) / T_s + R_s i_{\beta(k)} \end{cases} \tag{34}$$

Based on the operation principle introduced above, the control diagram of DTC-SVM will be generated and shown below as Fig. 4.11.

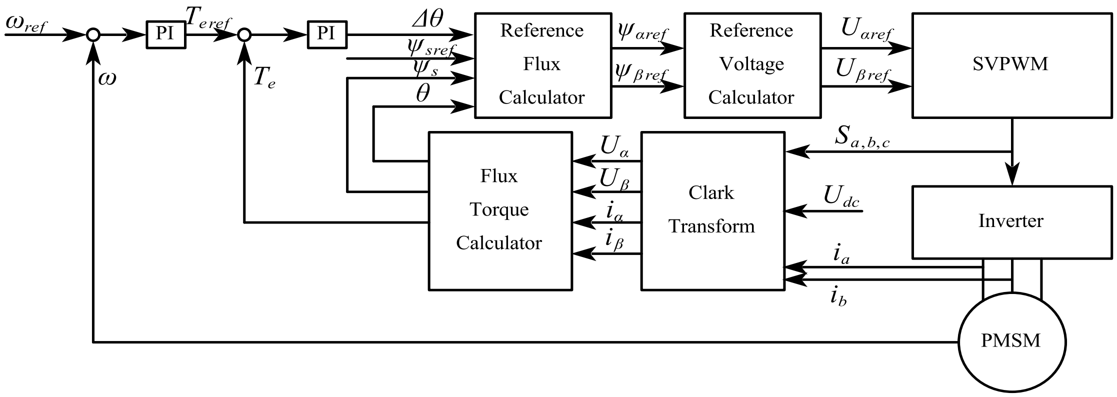

Fig. 4.11. The control diagram of DTC-SVM.

4.3.2 Space Vector Pulse Width Modulation (SVPWM)

SVPWM regards PMSM and inverter as one object, providing PMSM with circular magnetic field with constant amplitude. According to ideal flux circle generated by three-phase symmetric sinusoidal voltage, use the effective voltage vector generated by different switch patterns of inverter to approximate the standard flux circle [50-53].

Define the following variables:

$$\begin{cases} U_{ref1} = U_\beta \\ U_{ref2} = \dfrac{\sqrt{3}}{2}U_\alpha - \dfrac{1}{2}U_\beta \\ U_{ref3} = -\dfrac{\sqrt{3}}{2}U_\alpha - \dfrac{1}{2}U_\beta \end{cases} \tag{35}$$

Then, the sector number N can be decided by Equation (36)

$$N = sign(U_{ref1}) + 2sign(U_{ref2}) + 4sign(U_{ref3}) \tag{36}$$

Where *sign*(*x*) is the sign function.

The corresponding relationship between N and sector number is shown in Table. 4.2.

Table. 4.2. Relationship between N and sector number.

N	3	1	5	4	6	2
Sector No.	1	2	3	4	5	6

For voltage vector in different sectors, the conducting time T_1, T_2 of each switch pattern is different. It has been shown in Table. 4.3.

Table. 4.3. Conducting time T_1, T_2 in different sectors.

Sector No.	1	2	3	4	5	6
T_1	-Z	Y	X	Z	-Y	-X
T_2	X	Z	-Y	-X	-Z	Y

Where:

$$\begin{cases} X = \dfrac{\sqrt{3}T_s U_\beta}{U_{dc}} \\ Y = \dfrac{\sqrt{3}T_s}{U_{dc}}\left(\dfrac{\sqrt{3}}{2}U_\alpha + \dfrac{1}{2}U_\beta\right) \\ Z = \dfrac{\sqrt{3}T_s}{U_{dc}}\left(-\dfrac{\sqrt{3}}{2}U_\alpha + \dfrac{1}{2}U_\beta\right) \end{cases} \tag{37}$$

For the switching point of voltage vector, define the following variables:

$$\begin{cases} T_a = \left(T - T_1 - T_2\right)/4 \\ T_b = T_a + T_1/2 \\ T_c = T_b + T_2/2 \end{cases} \tag{38}$$

Assign $T_{\mathrm{cm}1}$, $T_{\mathrm{cm}2}$ and T_{cm3} according to Table. 4.4, where $T_{\mathrm{cm}1}$, $T_{\mathrm{cm}2}$ and T_{cm3} are defined as the conducting time of phase A, B and C, respectively.

Table. 4.4. Calculation of switch point.

Sector No.	1	2	3	4	5	6
T_{cm1}	T_b	T_a	T_a	T_c	T_c	T_b
T_{cm2}	T_a	T_c	T_b	T_b	T_a	T_c
T_{cm3}	T_c	T_b	T_c	T_a	T_b	T_a

The simulation model of DTC-SVM has been built in MATLAB/Simulink, the parameters of PMSM and load condition are the same as the conventional DTC simulation. Because of the advantages of SVPWM, it can achieve constant switching frequency which is 10kHz in this simulation, which will make it easier and more reliable for hardware implementation. Besides that, SVPWM can also achieve torque ripple minimization, which can not only keep the dynamic performance advantage of conventional DTC, but also compensate the static performance disadvantage of conventional DTC. The simulation result is shown as Fig. 4.12. below.

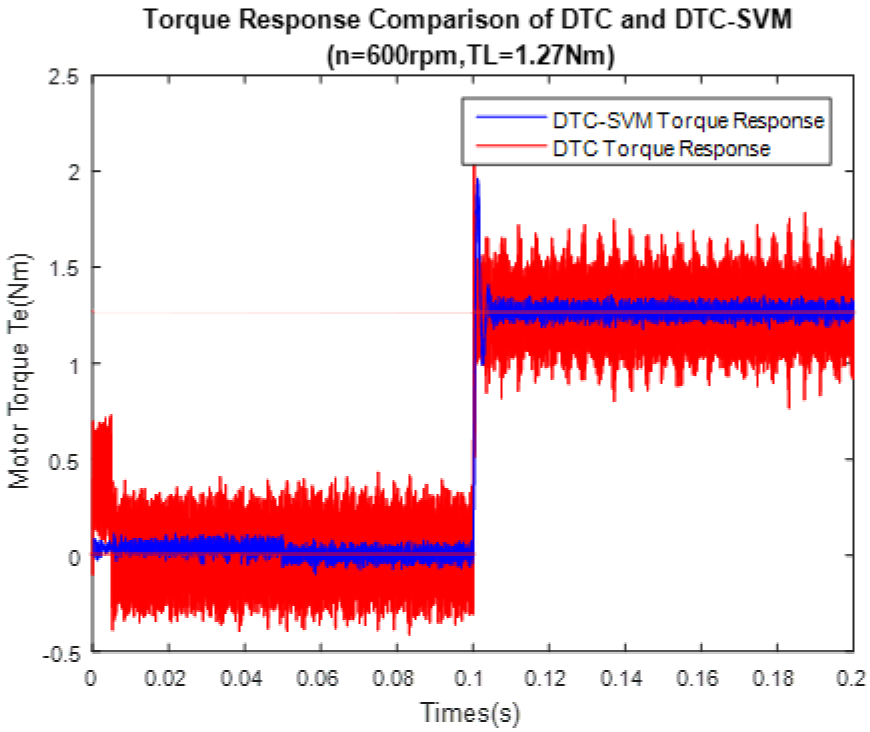

Fig. 4.12. Torque Response comparison of conventional DTC and DTC-SVM.

From Fig. 4.12, it can be known that DTC-SVM has much smaller torque ripple compared with conventional DTC, and the dynamic response is the same. So, it is proved that DTC-SVM is feasible and more effective and will be a better application prospect.

Chapter 5

Implementation and Experimental Investigations of the Proposed DTC-SVM

In this chapter, the implementation of DTC-SVM for PMSM using GaN based inverter is presented. It mainly focuses on the process of implementation and experimental studies. This chapter can be divided into four sections:1) introductions of the hardware platform including the DSP and the GaN based motor drive; 2) implementation of FOC for reference of the proposed DTC-SVM; 3) implementation of the proposed DTC-SVM; and 4) experimental investigations and results using the improved DTC-SVM for PMSM control.

5.1 The Introduction of DSP TMS320F28335

A Digital Signal Processor is a specific device that is designed around the typical mathematical operations to manipulate digital data that are measured by signal sensors. The objective is to process the data as quickly as possible to be able to generate an output stream of “new” data in “real time” [54]. Depend on powerful calculation ability and fast speed processing of the current digital signal processor, plenty of industry applications are utilizing DSPs to implement control algorithm. The features of DSP TMS320F28335 used for hardware implementation are shown below [54-60]:

(1) High-Performance Static CMOS Technology
  - Up to 150 MHz (6.67-ns Cycle Time)
  - 3.3-V I/O Design

(2) High-Performance 32-Bit CPU
  - IEEE 754 Single-Precision Floating-Point Unit (FPU)
  - Harvard Bus Architecture
  - Fast Interrupt Response and Processing

(3) On-Chip Memory
  - 256K × 16 Flash, 34K × 16 SARAM

(4) Peripheral Interrupt Expansion (PIE) Block
  - Supports all 58 Peripheral Interrupts

(5) Enhanced Control Peripherals
  - Up to 18 PWM Outputs
  - Up to 2 Quadrature Encoder Interfaces

(6) Three 32-Bit CPU Timers

(7) 12-Bit ADC, 16 Channels
   - 80-ns Conversion Rate
   - 2 × 8 Channel Input Multiplexer
   - Single/Simultaneous Conversions

(8) Up to 88 Individually Programmable, Multiplexed GPIO Pins with Input Filtering

For hardware implementation of FOC and DTC, a well-developed control card as in Fig. 5.1 will be used. This control card can be plugged into mother board to be a time-effective solution and can also ensure the quality of the design.

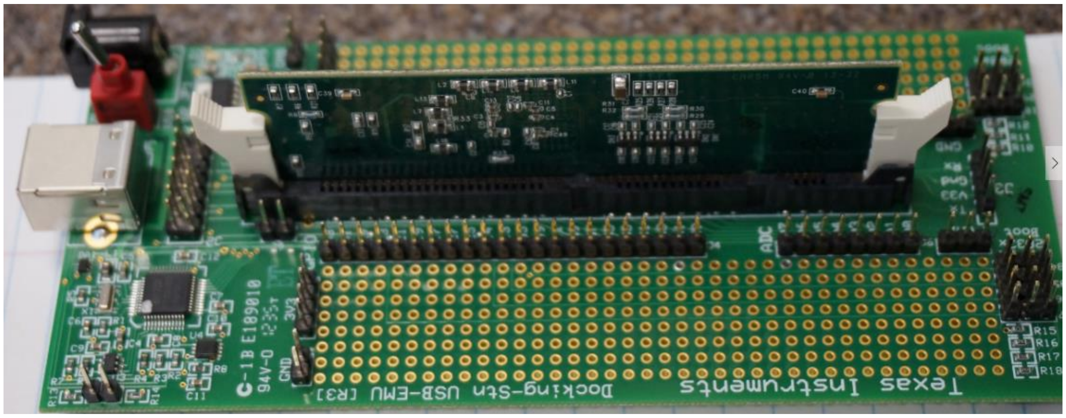

Fig. 5.1. DSP TMS320F28335 Experimental kit.

According to the specified functionalities, the GPIOs of the DSP are assigned as Table. 5.1. Follow this assignment, the schematic and PCB layout of the control board are then designed.

Table. 5.1. GPIO assignment of the DSP control card.

GPIO No.	Function	Direction	GPIO No.	Function	Direction
0	PWM1A	Output	1	PWM1B	Output
2	PWM2A	Output	3	PWM2B	Output
4	PWM3A	Output	5	PWM3B	Output
6	PWM Enable	Output	16	SPI	
17	SPI		18	SPI	
19	SPI		20	QEPA	Input
21	QEPB	Input	23	QEP Index	Input
29	/Fan ON	Output	30	CANRX	Input
31	CANTX	Output			

5.2 Implementation of FOC

According to control theory of FOC for PMSM drive system, it can be known that for hardware implementation, DSP should achieve the following functions:

- Sampling the analog signal, i.e. DC voltage of the DC bus and AC currents fed to the PMSM from inverter.
- Utilizing the sampling results from analog to digital conversion to do Clarke and Park transformation to achieve decoupling of *d*- and *q*-axis current components.
- Utilizing the PI controllers to control *d*- and *q*-axis current components.
- Utilizing the quadrature encoder to obtain the relative rotor position of the PMSM by QEP module.
- Calculating the speed of the PMSM through the encoder signals.
- Utilizing the PI controller to control the speed of PMSM.

As aforementioned, FOC independently control the torque and flux of PMSM like DC motor operation. The overall block diagram of FOC with position sensor is depicted in Fig.5.2.

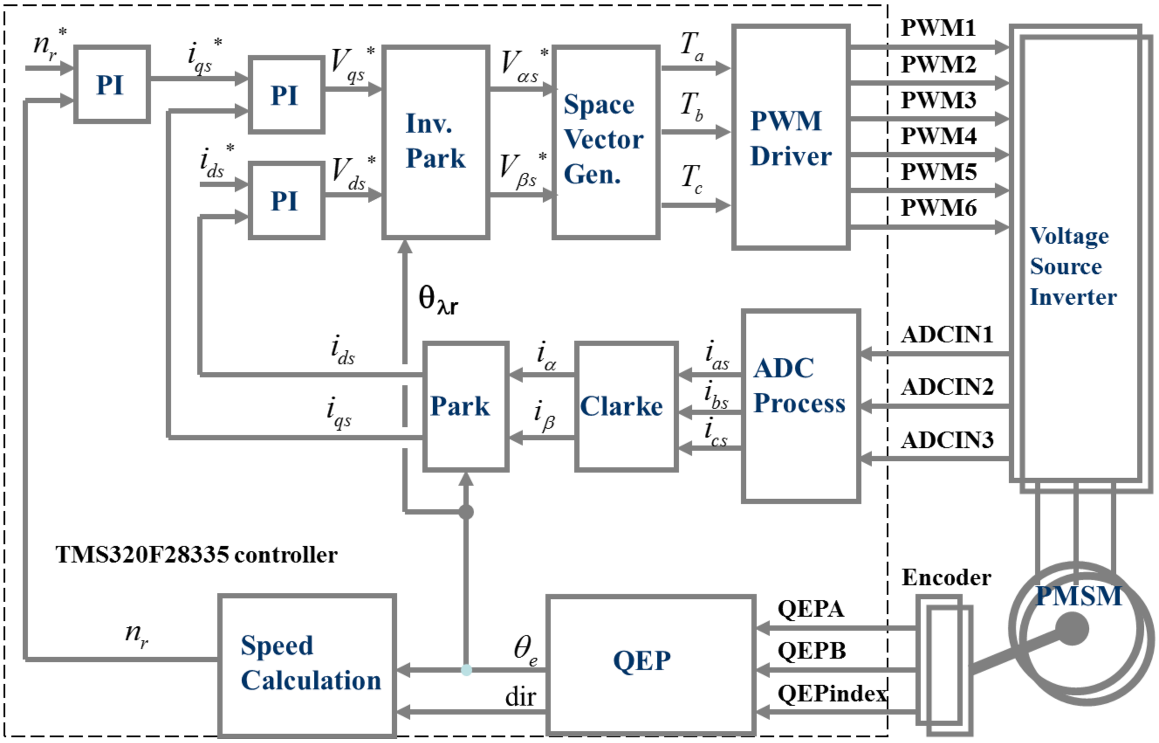

Fig. 5.2. Overall block diagram of FOC with position sensor.

Since the project for hardware implementation of FOC is quite a complicate project, it requires many function modules and multiple interrupts running in the background loop. Therefore, the software design for hardware implementation of FOC is divided into three parts according to their functionalities: Fig. 5.3 is the flowchart of main function; Fig. 5.4 is the flowchart of ADC interrupt; Fig. 5.5 is the flowchart of Timer0 interrupt.

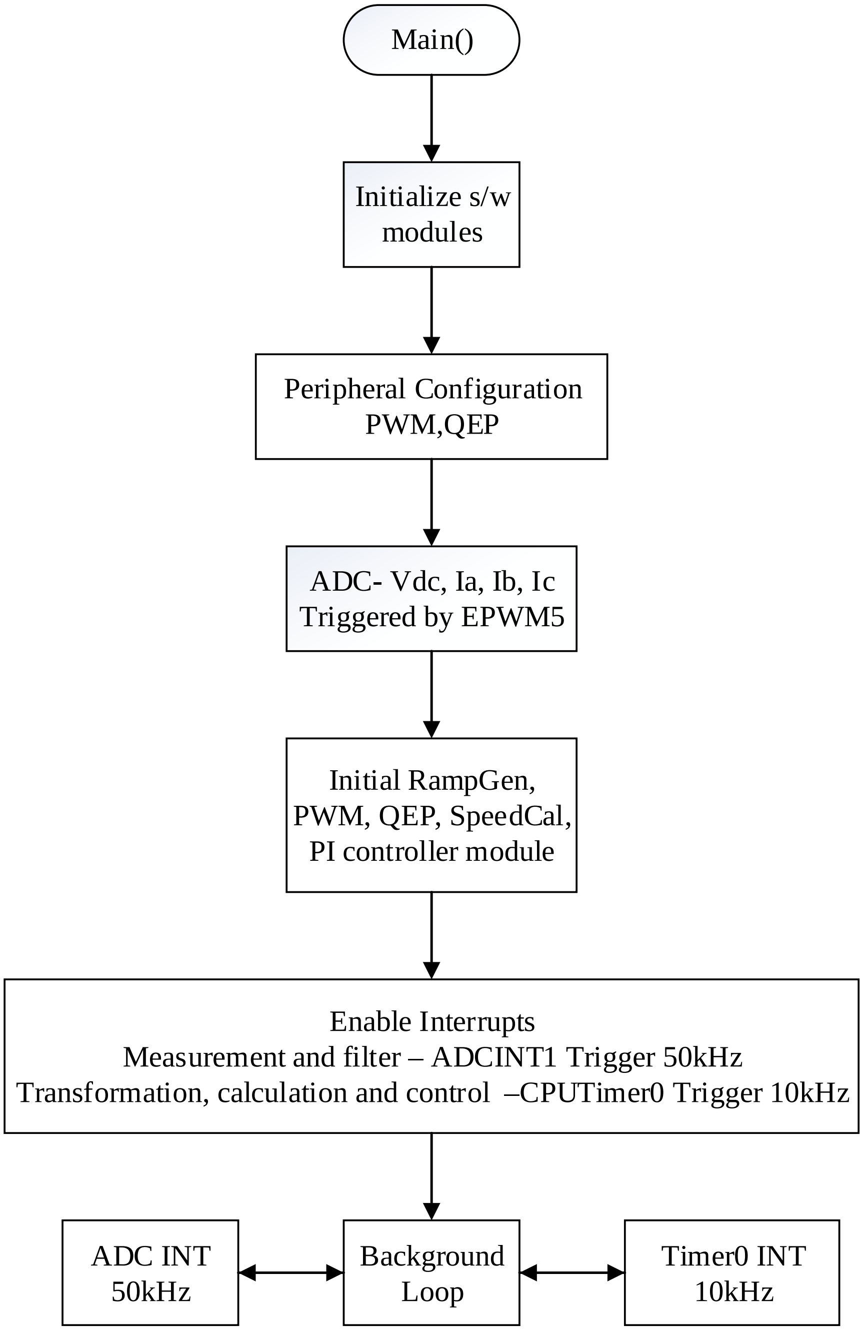

Fig. 5.3. Main function flowchart of software design for hardware implementation of FOC.

In main function, after initial the basic core for the system control, the watchdog is enabled to protect the project from elapsing or time out. If due to a hardware failure or error happens in the program, the DSP fails to reset the watchdog, it will elapse and generate a timeout signal to initiate the corrective actions. Then disable all interrupts in order to assign interrupt as requirement. After that peripheral configuration is initiated to select the multiplex assignments of GPIO, such as PWM, QEP, etc. Then ADC, RampGen, PWM, QEP, Speed and PI module is initiated. Also, two kinds of interrupts are used to achieve calculation and control, which are ADC and CpuTimer0 interrupt. Both interrupts need to be enabled in the main function. ADC interrupt is triggered at the end of every sampling sequence, and Timer0 is triggered by the timer existing in the core of DSP.

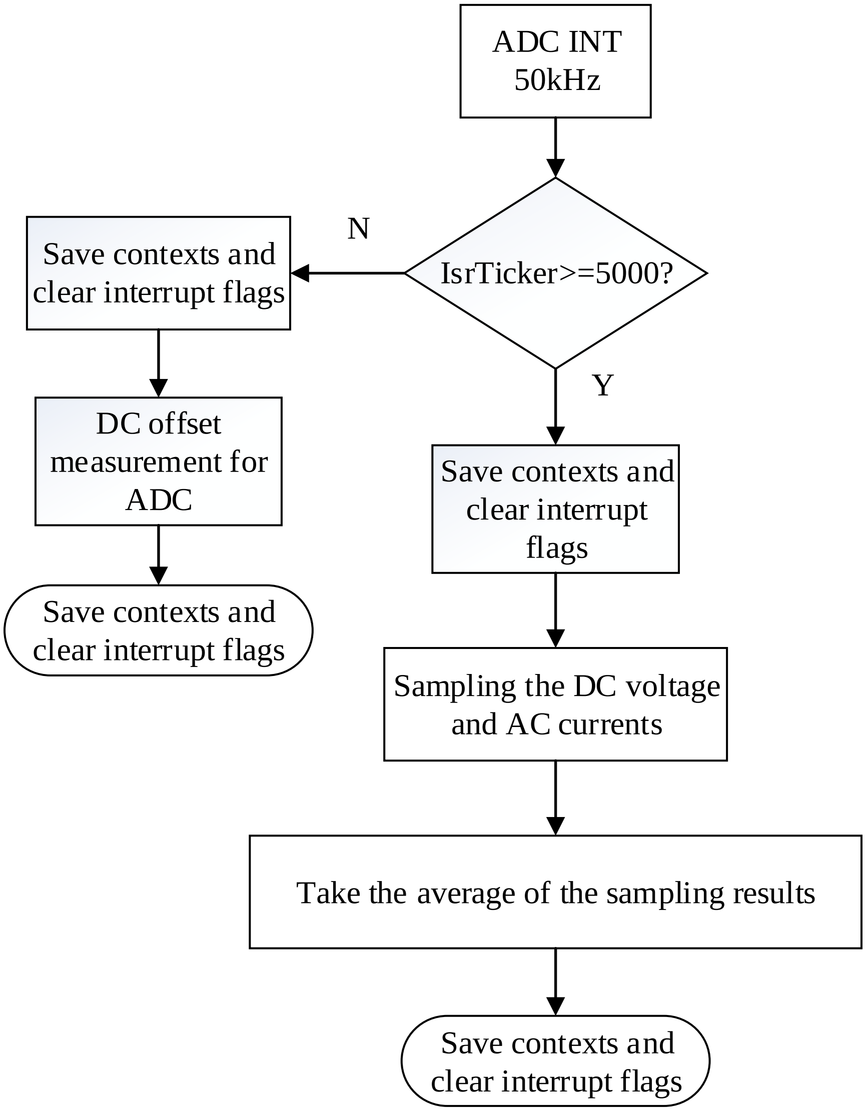

Fig. 5.4. ADC interrupt flowchart of software design for hardware implementation of FOC.

In the background loop, ADC INT and Timer0 INT will work separately to implement the calculation and control algorithm. ADC INT is triggered at the end for sampling sequence, so the frequency is 50 kHz. In ADC INT, there are two functions. The first is offset measurement for ADC, which is sampling the DC offset value for every ADC channel at the start stage of project. Then the offset value will be used in calculation of the sampled value to process the sampled results. The second is processing the sample values. As mentioned before, the DC voltage and three phase AC currents need to be sampled by the ADC. To increase the accuracy of the sampled value used for calculation and control, the sampled values are filtered by using arithmetic mean of the sampled values. Since the frequency of the ADC INT is five times of the Timer0 INT, the sampled values can be accumulated for five times then take the arithmetic mean of the results.

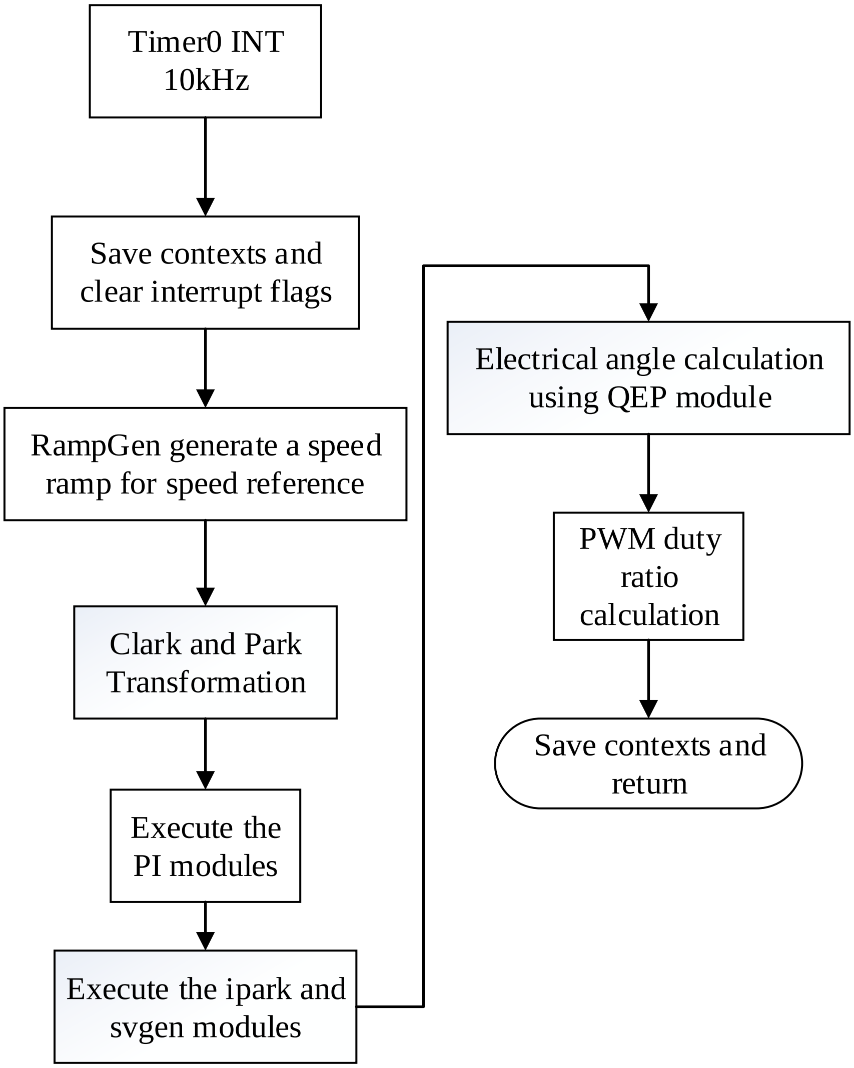

Fig. 5.5. Timer0 interrupt flowchart of software design for hardware implementation of FOC.

The main control and calculation of FOC will be implemented in Timer0 INT, which is triggered by timer in the core of the DSP with the frequency of 10kHz.

In Timer0 INT, at first the speed reference will be given to a module called RampControl (RC), which can generate a ramp signal of the speed reference. Then the filtered results from ADC INT of three phase AC currents will be transformed to α- and β-axis by Clarke Transformation. Next, the results will be transformed to *d*- and *q*-axis by Park Transformation. The angle used for Park Transformation is obtained from QEP module, which can calculate the electrical angle through capturing the encoder signals.

Then, the speed reference from the output of the RC module will given to the PI control module for speed control as the reference. The speed feedback value is calculated by the speed calculation module SpeedFR. The output of speed PI control module will be given to another PI control module for *q*-axis current control for as the reference. The *q*-axis current feedback value is from the output of Park Transformation. For *d*-axis current control, the reference of the PI control module is zero, since the I_d=0 control is used in this project. The *d*-axis current feedback value is also from the output of Park Transformation.

The outputs from *d*- and *q*-axis current PI control module then are sent to the inverse Park Transformation module to convert the regulated voltage from *d*- and *q*-axis to α- and β-axis. After the inverse Park Transformation, the α- and β-axis voltage will be sent to SVGEN module to execute the space vector generation to obtain the duty ratios of PWM signals.

As mentioned before, the electrical angle used for transformation is calculated by the QEP module, then will be sent to the SpeedFR module to calculation the speed of the PMSM used for speed PI control module to achieve a close loop control of PMSM.

At last, the duty ratios of PWM signals are sent to PWM signal generation module to generate the PWM signals for GaN-based inverter to drive the PMSM.

The software design for hardware implementation of FOC for PMSM drive system. In the project, all the sampling, calculation and control is achieved based on the DSP TMS320F28335 of Texas Instruments. The project is programmed by C codes to control the PMSM fed by a GaN-based inverter. The software consists of digital IOs, ADC sampling, reference frame transformation, PI controllers, QEP position calculation, speed calculation, SVPWM generation and PWM drive module.

Before applying any of the above software design to control the PMSM using GaN-based inverter, they have been verified initially. Because the program developed by TI has been referred during the software design, the idea for testing the software is also referred during the validation.

As Fig. 5.2 shows, the system can be gradually built in order for the final system can be confidently operated. Four phases of the incremental system build are designed to verify the major software modules used in the system.

5.2.1 Level 1 Incremental Build

For this level, there is no power flow through the inverter and PMSM. It is a simplest system check which used for verifying the system interrupt, inverse Park Transformation, SVGEN and PWM drive modules. The level can be defined to be 1 before the main function. Then debug the project and run.

Once the program is running, the variable named "IsrTicker" will be incrementally increased as seen in watch windows to confirm the ADC interrupt for offset measurement and CpuTimer0 for calculation and control working properly. Then the counter called "ADCCNT" will change from 0 to 5 to execute the sampling tasks after the offset measurement is done.

The incremental system build block diagram for level 1 is shown below as Fig. 5.6. Using the assumed SpeedRef value to generate an angle signal to imitate the change of angel when the PMSM is rotating through RG_MACRO module. Then the assumed VdTesting and VqTesting values are used for inverse Park Transformation. The output of IPARK_MACRO module is given to the SVGEN_MACRO module to generate the duty ratios of three phase PWM signals. The three outputs from SVGEN_MACRO module are monitored via the graph window as shown in Fig. 5.7 where T_a, T_b, and T_c waveform are 120° apart from each other. Specifically, T_b lags T_a by 120-degree and T_c leads T_a by 120-degree. Check the PWM test points on the board to observe PWM pulses and make sure that the PWM module is running properly.

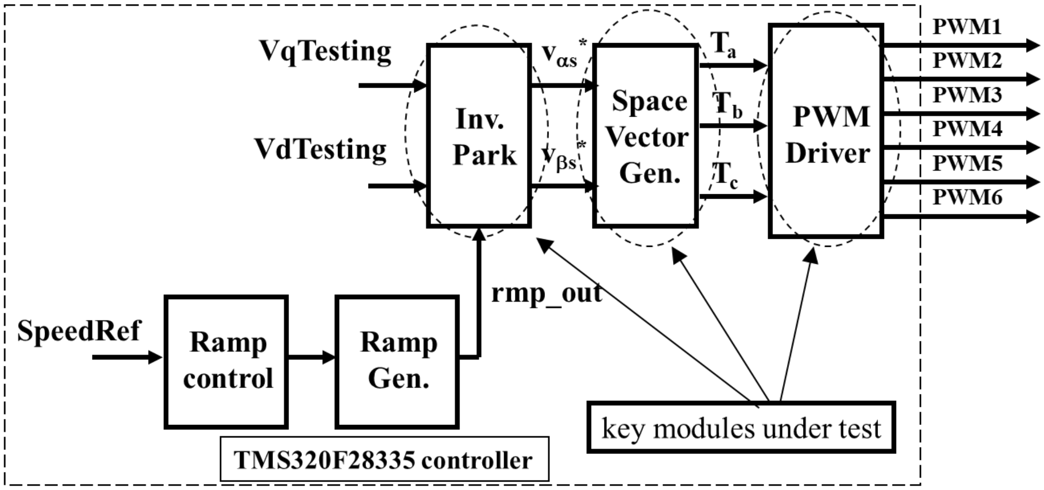

Fig. 5.6. Level1- Incremental system build block diagram [56].

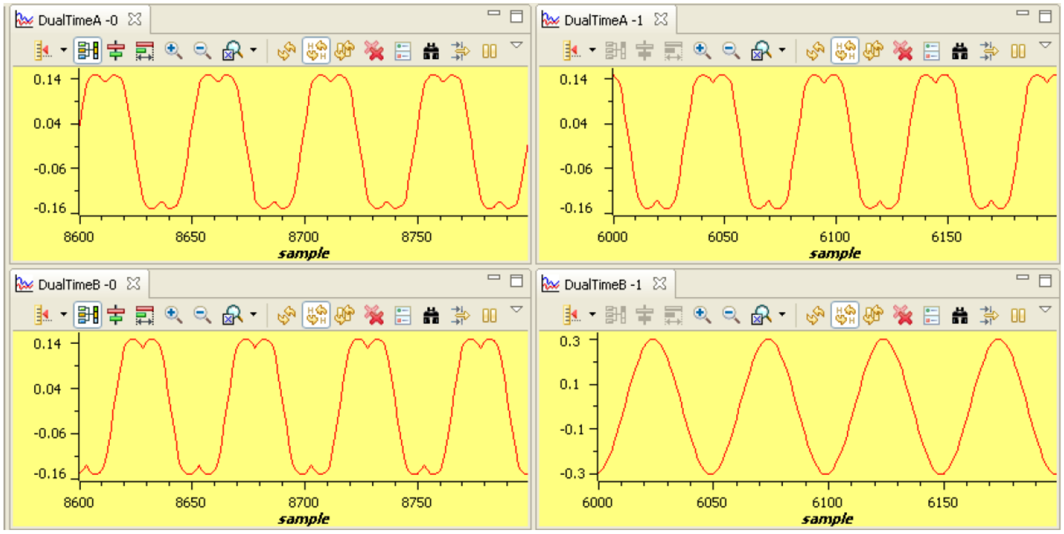

Fig. 5.7. Output of SVGEN, Ta, Tb, Tc and Tb-Tc waveforms [56].

5.2.2 Level 2 Incremental Build

The validation of level 2 is based on level 1 is completed successfully. In level 2, the ADC and reference frame transformation modules will be verified. At this level, the motor can connect to the inverter since the PWM signals are successfully proven at level 1 incremental build. Note that the open loop experiments are meant to test the ADCs, inverter stage, switching modules etc. Therefore, running motor under load or at various operating points is not recommended. Define the level to be 2, then debug the project and run.

The incremental system build block diagram for level 2 is shown below as Fig. 5.8.

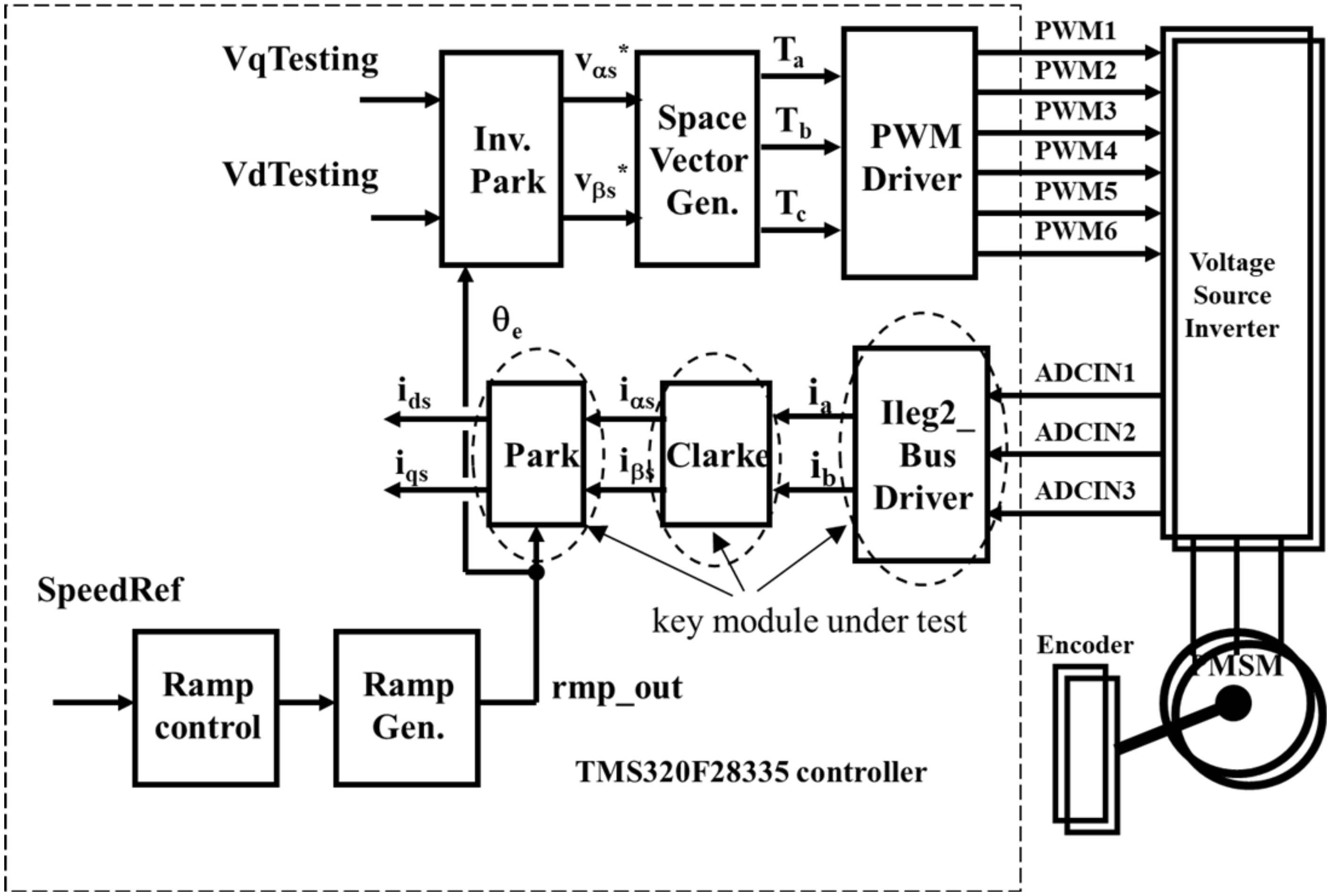

Fig. 5.8. Level2- Incremental system build block diagram [56].

During the open loop tests, VqTesting, SpeedRef and DC Bus voltages should be adjusted carefully for PM motors so that the generated Bemf is lower than the average voltage applied to motor winding. This will prevent the motor from stalling or vibrating. First, the Clarke module will be tested. The three measured line currents are transformed to two phases *d*- and *q*-axis currents in a stationary reference frame. The outputs of this module can be checked from graph window. It should be noted that the clark1.Alpha waveform should be same as the clark1.As waveform. And the clark1.Alpha waveform should be leading the clark1.Beta waveform by 90-degree at the same magnitude. The waveforms of SVGEN_dq1.Ta, rg1.Out, and phase A&B currents are shown below as Fig. 5.9.

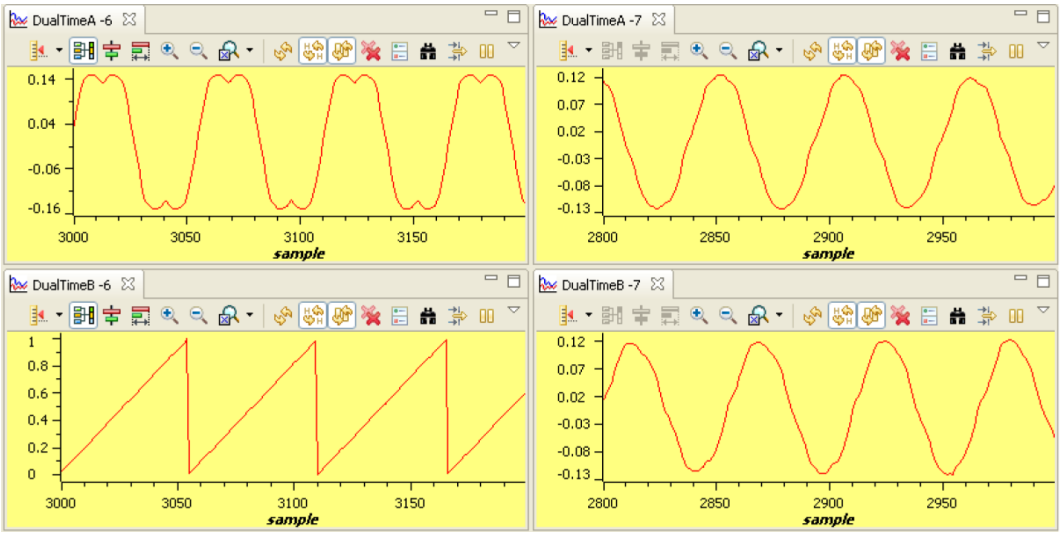

Fig. 5.9. The waveforms of SVGEN_dq1.Ta, rg1.Out, and phase A&B currents [56].

Also, in level 2, the PI controller limits for *d*- and *q*-axis currents can be adjusted. Note that the vectoral sum of *d*- and *q*-axis PI outputs should be less than 1.0 which refers to maximum duty cycle for SVGEN macro. Another duty cycle limiting factor is the current sense through shunt resistors which depends on hardware/software implementation. Depending on the application requirements 3, 2 or a single shunt resistor can be used for current waveform reconstruction. The higher number of shunt resistors allow higher duty cycle operation and better dc bus utilization.

Run the system with default VdTesting, VqTesting and SpeedRef and gradually increase VdTesting and VqTesting values. Meanwhile, watch the current waveforms in the graph window. Keep increasing until you notice distorted current waveforms and write down the maximum allowed VdTesting and VqTesting values. Make sure that these values are consistent with expected *d*- and *q*-axis current component maximums while running the motor. After this build level, PI outputs will automatically generate the voltage reference and determine the PWM duty cycle depending on the *d*- and *q*-axis current demand, therefore set pi_id.Umax/min and pi_iq.Umax/min according to recorded VdTesting and VqTesting values respectively.

5.2.3 Level 3 Incremental Build

The validation of level 3 is based the previous levels are completed successfully. In level 3, the PI controllers for *d*- and *q*-axis currents regulation and speed measurement modules. To confirm the operation of current regulation, the gains of these two PI controllers are necessarily tuned for proper operation. Define the level to be 3, then debug and run the project.

The incremental system build block diagram for level 3 is shown below as Fig. 5.10.

In this level, the PMSM is running at open speed loop, and the PMSM is supplied by AC input voltage and the current is dynamically regulated by using PI module through the park transformation of the motor currents. For level 3, before closing the current loop, there are a few steps need to be done to verify the PI controller for *d*- and *q*-axis currents regulation:

(1) Set SpeedRef to 0.3 pu, Idref to zero and Iqref to 0.05 pu.
(2) Gradually increase voltage at variac / dc power supply to get an appropriate DC-bus voltage.
(3) Check pi_id.Fdb in the watch windows with continuous refresh feature whether or not it should be keeping track pi_id.Ref for PI module.
(4) Check pi_iq.Fdb in the watch windows with continuous refresh feature whether or not it should be keeping track pi_iq.Ref for PI module.
(5) To confirm these two PI modules, try different values of pi_id.Ref and pi_iq.Ref or SpeedRef.
(6) For both PI controllers, the proportional, integral, derivative and integral correction gains may be re-tuned to have the satisfied responses.
(7) Bring the system to a safe stop as described at the end of build 1 by reducing the bus voltage, taking the controller out of realtime mode and reset. Now the motor is stopping.

During running this level, the current waveforms in the CCS graphs should appear as Fig. 5.11.

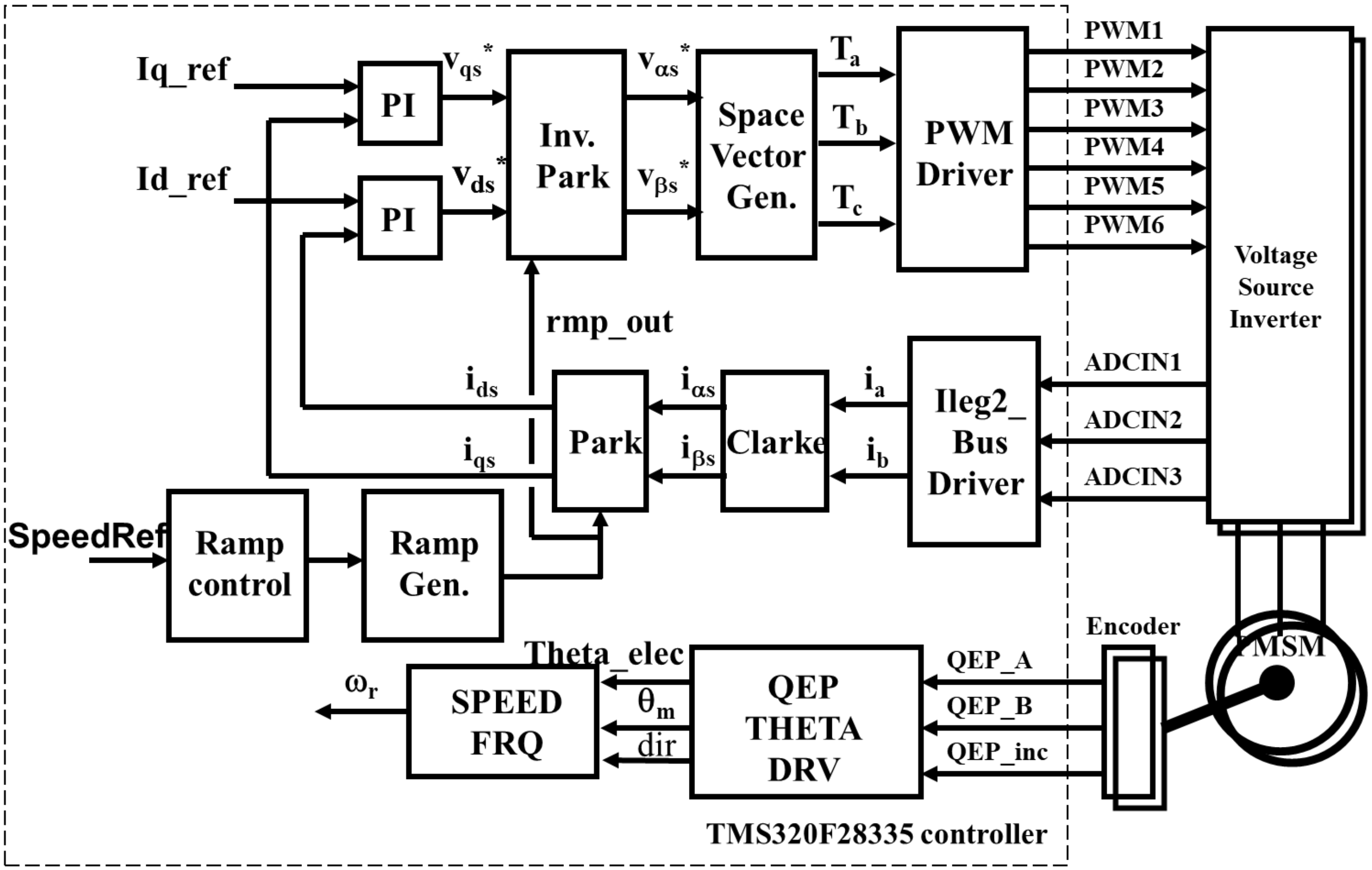

Fig. 5.10. Level3- Incremental system build block diagram [56].

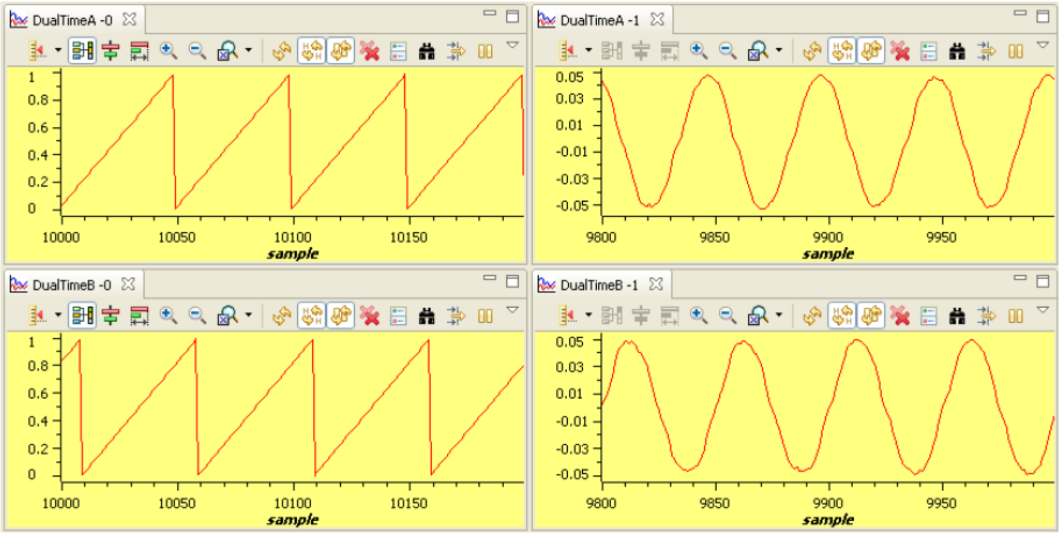

Fig. 5.11. Measured theta, rg1.out and Phase A & B current waveforms [56].

Then the QEP drive and speed calculation modules need to be verified. QEP drive macro determines the rotor position and generates a direction (of rotation) signal from the shaft position encoder pulses. The details related to these two modules have already been presented before. The steps to verify these two software modules related to the position and speed measurement can be described as follows:

(1) Set SpeedRef to 0.3 pu.

(2) Compile/load/run program with real time mode and then increase voltage at variac / dc power supply to get the appropriate DC-bus voltage.

(3) Add the soft-switch variable “lsw” to the watch window in order to switch from current loop to speed loop. In the code lsw manages the loop setting as follows:

  - lsw=0, lock the rotor of the motor.
  - lsw=1, close the current loop. PMSM runs at open loop control.

(4) Set lsw to 1. Now the motor is running close to reference speed. Check the “speed1.Speed” in the watch windows with continuous refresh feature whether or not the measured speed is around the speed reference.

(5) To confirm these modules, try different values of SpeedRef to test the speed.

(6) Check that both qep1.ElecTheta and rg1.Out are of saw-tooth wave shape and have the same period. If the measured angle is in opposite direction, then change the order of motor cables connected to inverter output.

(7) Check from Watch Window that qep1.IndexSyncFlag is set back to 0xF0 every time it reset to 0 by hand. Add the variable to the watch window if it is not already in the watch window.

(8) Qep1.ElecTheta should be slightly lagging rg1.out, if the calibration angle needs to be adjusted due to the angle offset between index and locked rotor position.
(9) Bring the system to a safe stop as described at the end of build 1 by reducing the bus voltage, taking the controller out of realtime mode and reset.

Next, the following steps are to verify and or perform calibration angle of the encoder. The steps are as follows:

(1) Set SpeedRef to 0.3 pu.
(2) Make sure EQep1Regs.QPOSCNT, EQep1Regs.QPOSILAT, Init_IFlag, qep1.CalibratedAngle, and lsw are displayed in watch window.
(3) Compile/load/run program with real time mode and then increase voltage at variac / dc power supply to get the appropriate DC-bus voltage.
(4) Now the rotor should be locked. Set lsw to 1 to spin the motor. When the first index signal is detected by QEP, the EQep1Regs.QPOSILAT register latches the angle offset in between initial rotor position and encoder index in the code. Later, EQep1Regs.QPOSILAT is set to maximum of EQep1Regs.QPOSCNT as it latches the counter value for each index signal. In the code qep1.CalibratedAngle keeps the initial offset value. This value can be recorded to initialize qep1.CalibratedAngle at the initialization section in main function.

5.2.4 Level 4 Incremental Build

The validation of level 4 is based the previous levels are completed successfully. In level 4, the PI controller for speed control will be verified. Define the level to be 4 to switch the build level, then debug and run the project.

The incremental system build block diagram for level 4 is shown below as Fig. 5.12.

The key steps can be explained as follows:

(1) Set Compile/load/run program with real time mode.
(2) Set SpeedRef to 0.3 pu.
(3) Gradually increase voltage at variac to get an appropriate DC-bus voltage and now the motor is running with this reference speed (0.3 pu).

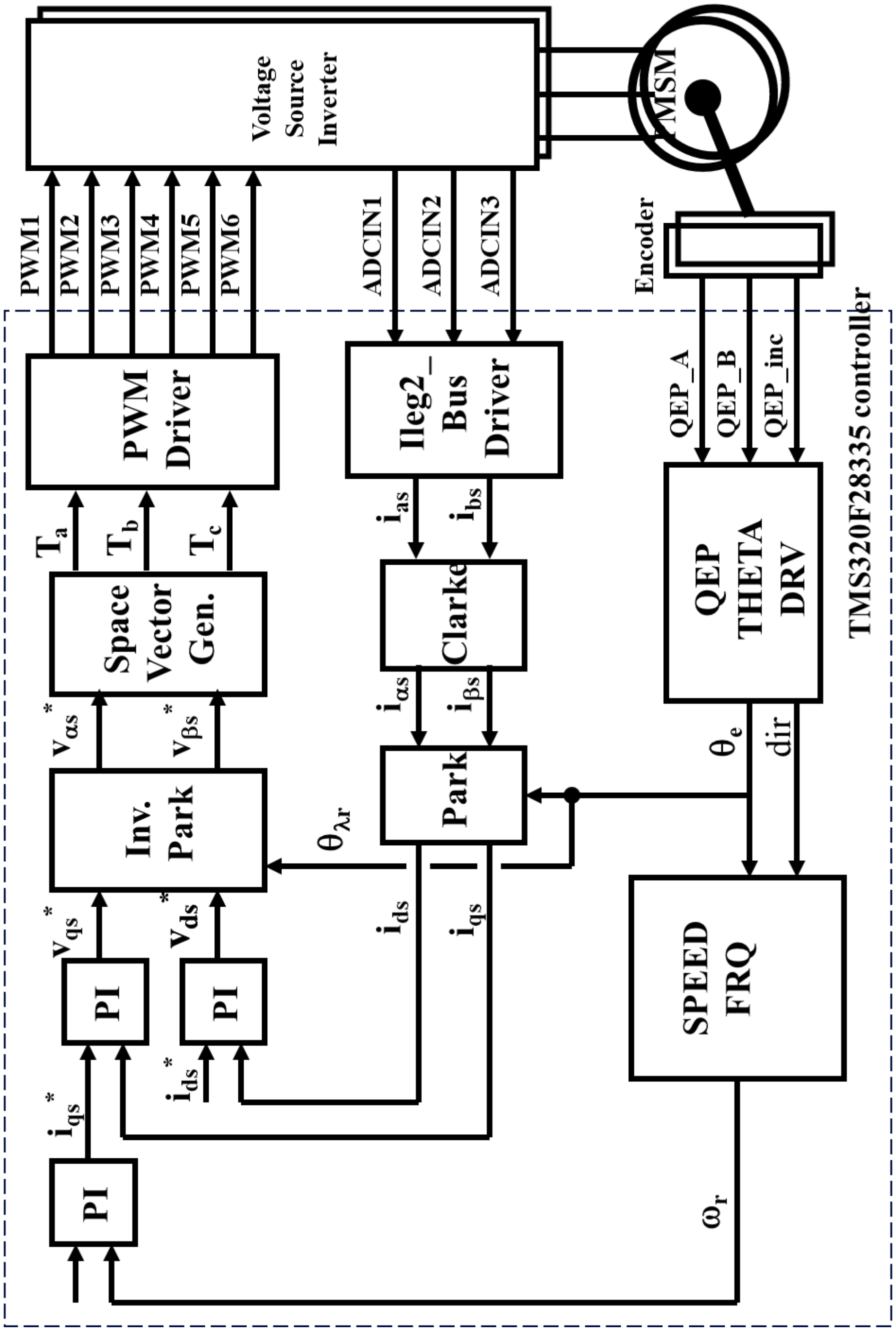

Fig. 5.12. Level4- Incremental system build block diagram [56].

(4) Add the soft-switch variable “lsw” to the watch window in order to switch from current loop to speed loop. In the code lsw manages the loop setting as follows:

- lsw=0, lock the rotor of the motor.
- lsw=1, close the current loop.

  - lsw=2, close the speed loop.

(5) Set lsw to 1. Compare Speed with SpeedRef in the watch windows with continuous refresh feature whether or not it should be nearly the same.

(6) To confirm this speed PI module, close the speed loop by setting lsw to 2 and try different values of SpeedRef. For speed PI controller, the proportional, integral, derivative and integral correction gains may be re-tuned to have the satisfied responses.

During running this build, the current waveforms in the CCS graphs should appear as follows:

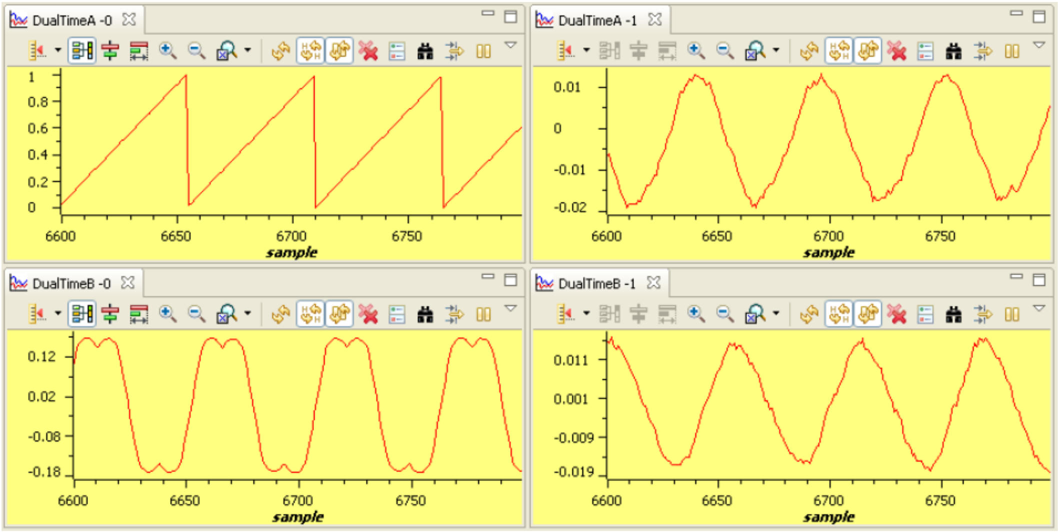

Fig. 5.13. Measured theta, SVGEN duty cycle, and Phase A&B current waveforms.

under no-load & 0.3 pu speed [56].

5.3 Implementation of DTC-SVM

Different from FOC, according to control theory of DTC-SVM for PMSM drive system, it can be known that for hardware implementation, DSP should achieve the following functions:

- Sampling the analog signal, i.e. DC voltage of the DC bus and two-phase AC currents fed to the PMSM from inverter.
- Processing the sampled results to achieve accuracy of sampling through filter.
- Utilizing the sampled results to obtain the V_a, V_b, I_a, I_b to do Clarke Transformation to obtain V_α, V_β, I_α, I_β.
- Utilizing V_α, V_β, I_α, I_β to calculate the stator flux linkage on α- and β-axis, which is $\psi_{s\alpha}$ and $\psi_{s\beta}$.

- Utilizing $\psi_{s\alpha}$ and $\psi_{s\beta}$ to estimate the stator flux linkage and angle.
- Calculating the speed of the PMSM through the encoder signals.
- Utilizing the PI controller to control the speed and electromagnetic torque of PMSM.
- Utilizing reference flux calculator to calculate the α- and β-axis stator flux linkage reference.
- Utilizing reference voltage calculator to calculate the α- and β-axis voltage reference.
- Utilizing the SVPWM module to generate PWM wave for DTC-SVM of PMSM.

The overall block diagram of DTC-SVM is depicted in Fig. 5.14.

Similar with the hardware implementation of FOC, DTC-SVM also requires many function modules and multiple interrupts running in the background loop to execute the sampling, calculation and control command. Therefore, the software design for hardware implementation of DTC-SVM is divided into four parts according to their functionalities: Fig. 5.15 is the flowchart of main function; Fig. 5.16 is the flowchart of ADC interrupt; Fig. 5.17 is the flowchart of Timer0 interrupt and Fig. 5.18 is the flowchart of Timer1.

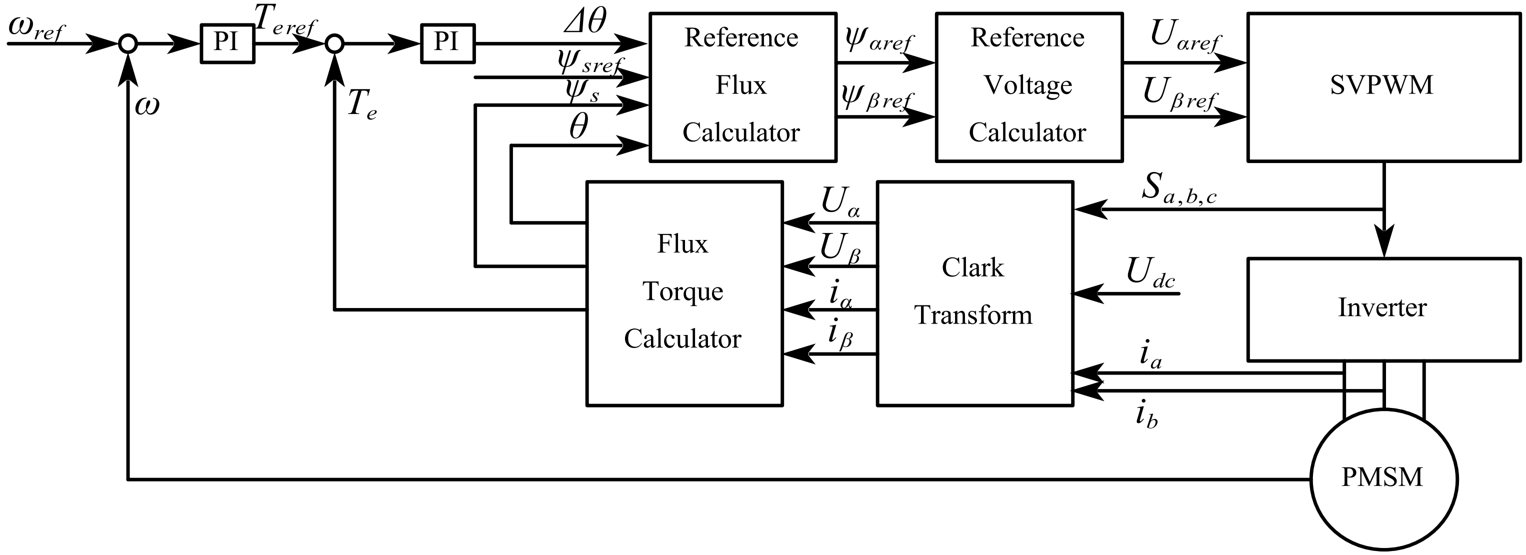

Fig. 5.14. Overall block diagram of DTC-SVM.

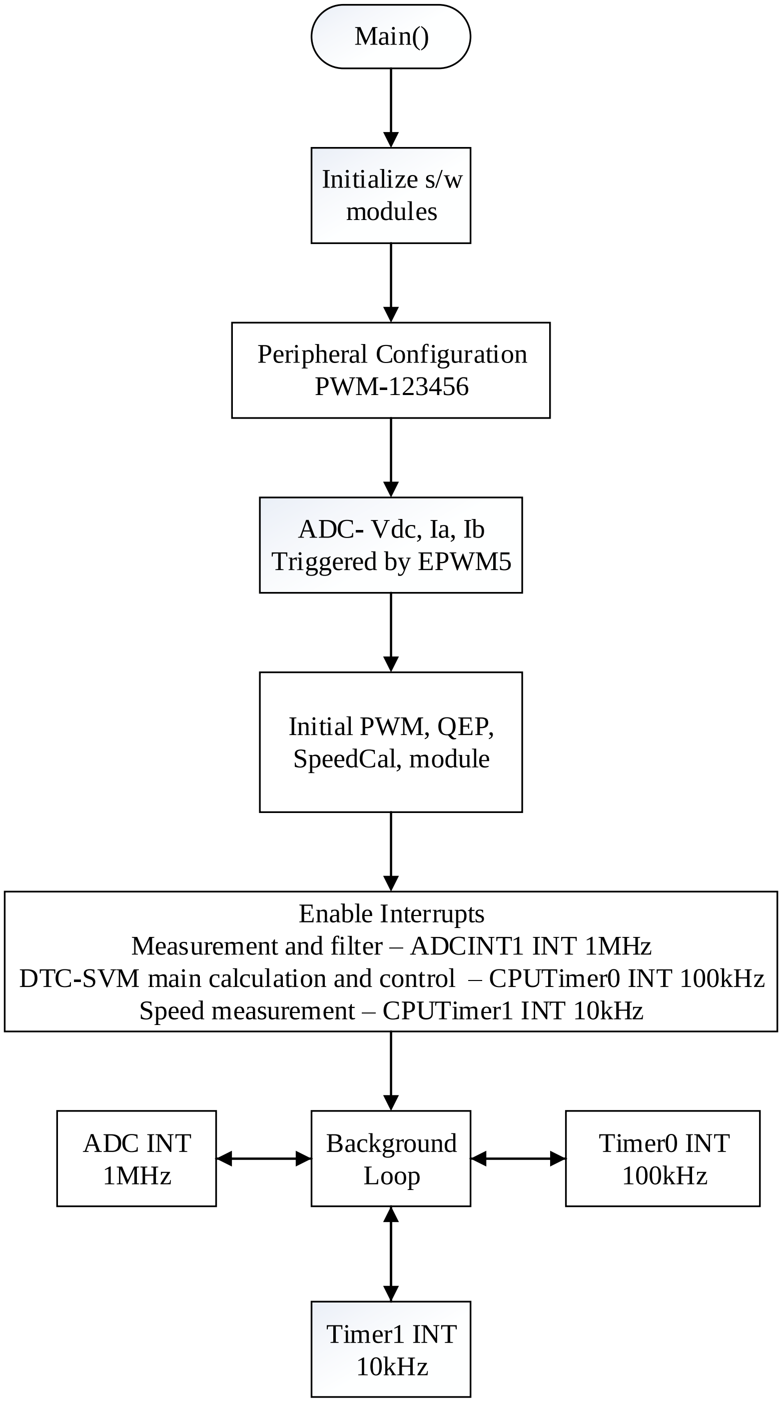

Fig. 5.15. Main function flowchart of software design for hardware implementation of DTC-SVM.

In main function, after initial the basic core for the system control, the watchdog is enabled to protect the project from elapsing or time out. If due to a hardware failure or error happens in the program, the DSP fails to reset the watchdog, it will elapse and generate a timeout signal to initiate the corrective actions. Then disable all interrupts in order to assign interrupt as requirement. After that peripheral configuration is initiated to select the multiplex assignments of GPIO, such as PWM, QEP, etc. Then ADC, PWM, QEP, Speed and PI module is initiated. The variables used for sampling, calculation and control need to be set to be the default value. Also, three kinds of interrupts are used to achieve calculation and control, which are ADC, CpuTimer0 and CpuTimer1 interrupt. All the interrupts need to be enabled in the main function. ADC interrupt is triggered at the end of every sampling sequence, and Timer0 and Timer1are triggered by the timer existing in the core of DSP.

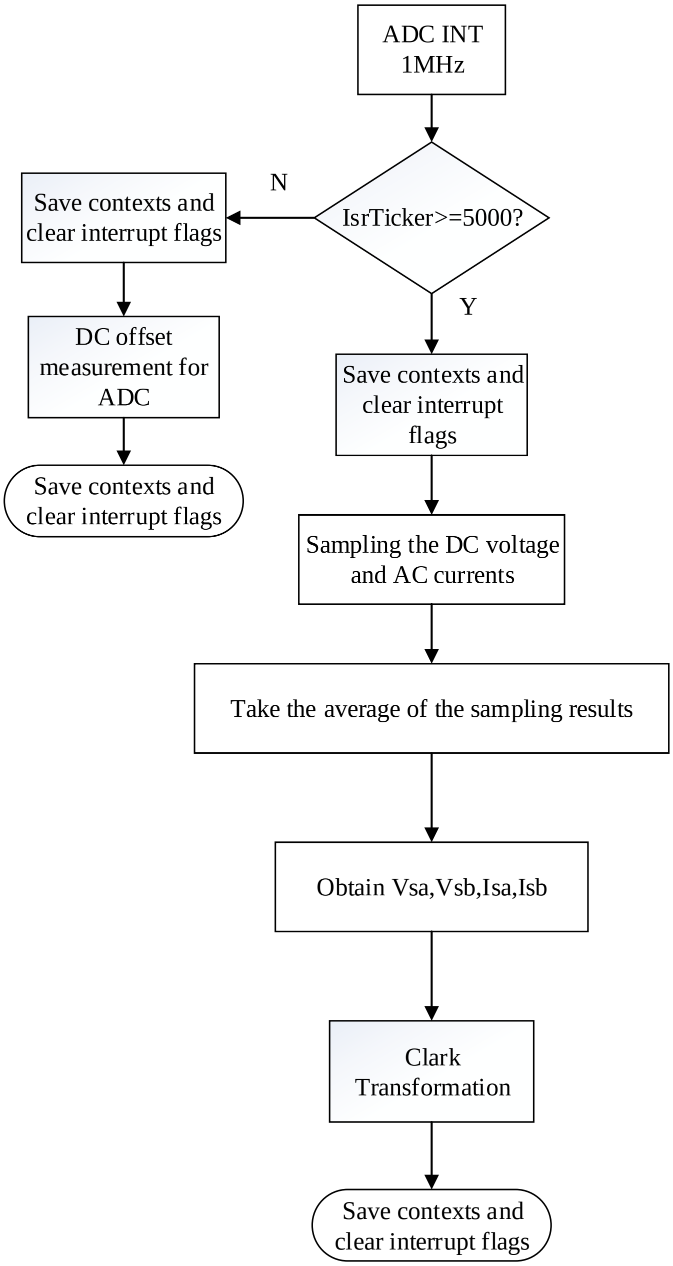

Fig. 5.16. The flowchart of ADC interrupt.

In the background loop, ADC INT, Timer0 INT and Timer1 INT will work separately to implement the calculation and control algorithm. ADC INT is triggered at the end for sampling sequence. Different from the FOC, in order to increase control performance and minimize the torque ripple, the sampling frequency should be as high as possible. So, for this project, the frequency of ADC INT is 1MHz. In ADC INT, there are two functions. The first is offset measurement for ADC, which is sampling the DC offset value for every ADC channel at the start stage of project. Then the offset value will be used in calculation of the sampled value to process the sampled results.

The second is processing the sample values. As mentioned before, the DC voltage and three phase AC currents need to be sampled by the ADC. To increase the accuracy of the sampled value used for calculation and control, the sampled values are filtered by using arithmetic mean of the sampled values. Since the frequency of the ADC INT is ten times of the Timer0 INT, the sampled values can be accumulated for ten times then take the arithmetic mean of the results. The filter results from ADC INT of DC voltage and two-phase AC currents will be then used for Clarke Transformation to be converted into α- and β-axis voltage and current.

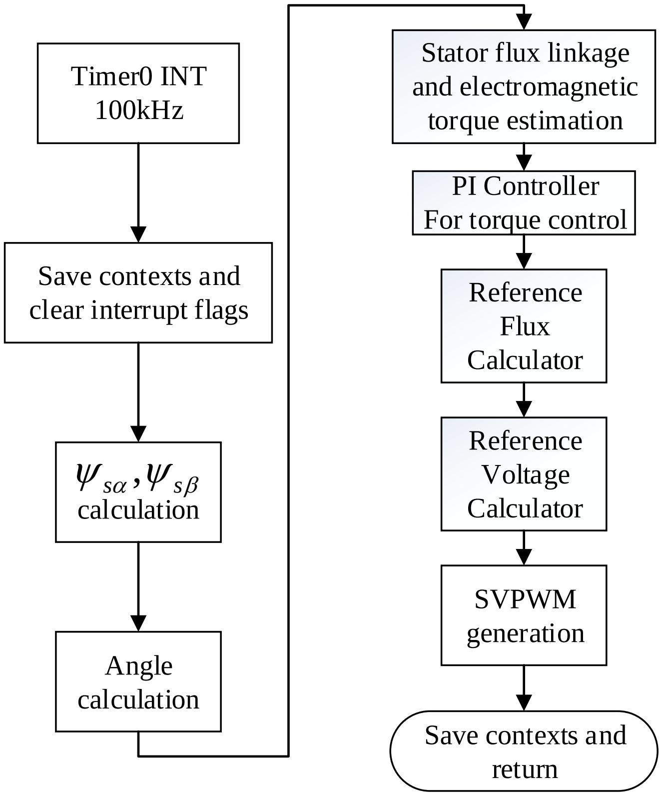

Fig. 5.17. The flowchart of Timer0 interrupt.

The main calculation and control of DTC will be implemented in Timer0 INT, which is triggered by timer0 in the core of the DPS with the frequency of 100kHz.

In Timer0 INT, at first the α- and β-axis voltage and current will be used for calculating the α- and β-axis stator flux linkage. Since the integration in DSP is quite different from the simulation, in this project, the integration will be achieving by using the equation below:

$$\psi_{s\alpha\beta(t)}\Big|_{t=\Delta t} = \psi_{s\alpha\beta(t)}\Big|_{t=0} \bullet \Delta t + \psi_{s\alpha\beta(t)}\Big|_{t=0} \tag{39}$$

Where Δt is the sampling time.

After the α- and β-axis stator flux linkages are estimated, then take the inverse tangent of $\frac{\psi_{s\beta}}{\psi_{s\alpha}}$. The result can determine the angle of stator flux linkage. Then the stator flux linkage amplitude can be calculated by $\sqrt{\psi_{s\alpha}{}^2 + \psi_{s\beta}{}^2}$, and the electromagnetic torque can also be calculated by $\frac{3}{2}p\left(\psi_{s\alpha}i_{s\beta} - \psi_{s\beta}i_{s\alpha}\right)$.

The torque reference is decided by the output of the PI speed controller, then the calculated the electromagnetic torque will be compared with the torque reference. The error will be sent to the PI torque controller to generate the error angle. Then according to the operation principle from the previous chapter of DTC-SVM, through the reference flux calculator and the reference voltage calculator, the α- and β-axis voltage reference can be obtained then given to the SVPWM module to generate PWM to achieve DTC-SVM of PMSM.

Unlike FOC, in this project, the QEP speed measurement is not included in the Timer0. Another CpuTimer1 is used to trigger the interrupt to measure the speed for speed control in Timer1. The speed loop should be slower than the electrical control loop, as the result of that, the frequency of Timer1 is set to be 10kHz. In this interrupt, QEP module will capture the encoder signals. Then the calculation of electrical angle will be done by the QEP module, then the Speed module will calculate the rotor speed, then send to Timer0 INT to achieve control of speed to generate torque reference for the PI controller for torque control.

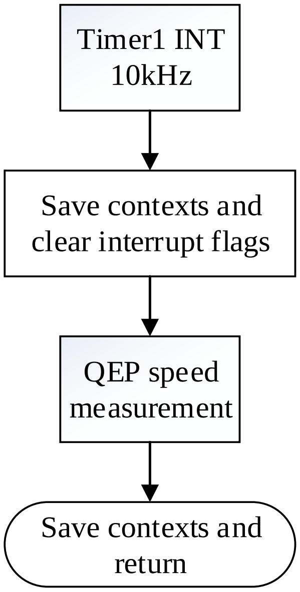

Fig. 5.18. The flowchart of Timer1 interrupt.

In the design of the software for DTC-SVM, there are some function modules need to be discussed. In the subsections below, there is an introduction of these function modules:

5.3.1 Design of ADC Module for Sampling

To achieve accurate control performance, achieving precise sampling is necessary to guarantee calculation and control will be correct. There are three methods to trigger the ADC module of DSP to start sampling: software trigger, PWM trigger and external trigger. At first, the software trigger is used to trigger the ADC to sample the DC voltage and three phase AC current. The sampling frequency can be set by the clock register of ADC. However, in the test, it has been found that the software trigger is not accurate, since the ADC is working at sequential cascaded mode, the actual sampling frequency will be the setting frequency divided by the number of sampling channel. That will affect practical sampling when the software runs in real-time, and it is difficult to get the arithmetic mean of the sampled value. As the result of that, PWM trigger is used for ADC module because it will have more accurate sample frequency. PWM5 is a vacant PWM, so it is used to trigger the ADC [55].

To make sure the sampling result is correct, the offset values need to be removed from the calculation. Although the offset values can be measure online, it still requires offline measurement of the offset values to make sure the sampling circuit is functional as design.

For offset measurement, a 1st-order low-pass filter is used. To apply 1st-order low-pass filter in a discrete system is shown below:

Since the transfer function of 1st-order low-pass RC filter in s-plane is:

$$\frac{V_{out(s)}}{V_{in(s)}} = \frac{1}{RCs+1} \tag{40}$$

Then use z transformation, let $s = \frac{1-z^{-1}}{T_s}$, T_s is the sampling time. Substituted into Equation (41), to get:

$$\frac{V_{out(z)}}{V_{in(z)}} = \frac{1}{RC\frac{1-z^{-1}}{T_s}+1} = \frac{T}{RC\left(1-z^{-1}\right)+T_s} \tag{41}$$

Then it can be converted to:

$$V_{in(z)} = \frac{RC}{T_s}V_{out(z)} - \frac{RC}{T_s}V_{out(z)}z^{-1} + V_{out(z)} \tag{42}$$

Then the Equation (32) can be converted to differential equation, which is:

$$V_{out(t)} = \frac{T_s}{RC+T_s}V_{in(t)} + \frac{RC}{RC+T_s}V_{out(t-1)} \tag{43}$$

In the project, RC is assumed to be 0.05, which means the cut off frequency $f_c = \frac{1}{2\pi RC} = 3.183Hz$.

5.3.2 Design of QEP Module for Position Calculation

For TMS320F28335, the encoder signals A, B and Index is connected to the EQEP2A, EQEP2B and EQEP2I pin to capture the pulses generated by the encoder. Since the number of pulses generated by the sensor is proportional to the angular displacement of the motor shaft. For example, a complete 360-degree rotation of motor will generate 2500 pulses of each of the signals in encoder A and B. The QEP circuit counts both edges of the two QEP pulses. This means, for 2500 pulses for each of encoder A and B, the number of counter clock cycles will be 10000.

Since the counter value is proportional to the number of QEP pulses, therefore, it is also proportional to the angular displacement of the motor shaft. When the QEP module is used to capture the encode signals, the position counter is obtained by QPOSCNT register. And the QDF bit in QEPSTS register is used to detect the rotational direction.

The encoder Index pulse can reset the timer counter T2CNT and sets the index synchronization flag IndexSyncFlag to 00F0. Thus, the counter T2CNT gets reset and starts counting the QEP_CLK pulses every time encoder Index high pulse is generated. To determine the rotor position at any instant of time, the counter value (T2CNT) is read and saved in the variable RawTheta. This value indicates the clock pulse count at that instant of time. Therefore, RawTheta is a measure of the rotor mechanical displacement in terms of the number of clock pulses [56].

As the example above, the maximum number of clock pulses in one revolution is 10000, so a coefficient called MechScaler can be used to obtain the mechanical displacement of the rotor, which is MechTheta. Then the electrical displacement ElecTheta can be calculated using polepairs multiplied by MechTheta. In this way, the electrical angle can be acquired for the speed calculation and reference frame transformation.

The offset value also need to be considered in the position calculation. In this project, PMSM will start to rotate at a starting position. The starting position is decided through switching on the upside switch of phase A, and switching on the bottom switches of phase B and C to let rotor aligns with winding of phase A. When the first index signal is detected by QEP, the EQep1Regs.QPOSILAT register latches the angle offset in between initial rotor position and encoder index in the code. Later, EQep1Regs.QPOSILAT is set to maximum of EQep1Regs.QPOSCNT as it latches the counter value for each index signal. In the code QEP1.CalibratedAngle keeps the initial offset value. This value can be recorded to initialize QEP1.CalibratedAngle at the initialization section in the main function or it can be detected in the code each time the motor is restarted [56].

5.3.3 Design of Speed Calculation Module

The QEP peripheral includes an integrated edge capture unit to measure the speed. There are two methods used for speed measurement target towards low and high speed.

For low speed measurement, the method is to measure the elapsed time between the unit position events to calculate the speed. This method has the following equation:

$$v(k) = \frac{x}{t(k) - t(k-1)} = \frac{x}{\Delta T} \tag{44}$$

Where, x is the unit position is defined by integer multiple of quadrature edges; ΔT is the elapsed time between unit position events and v(k) is the velocity at time instant *k*.

The QEP capture timer (QCTMR) runs from prescaled SYSCLKOUT and the prescaler is programmed by the QCAPCTL[CCPS] bits. The capture timer (QCTMR) value is latched into the capture period register (QCPRD) on every unit position event and then the capture timer is reset, a flag is set in QEPSTS: UPEVNT to indicate that new value is latched into the QCPRD register. Software can check this status flag before reading the period register for low speed measurement and clear the flag by writing 1.

Time measurement (ΔT) between unit position events will be correct if the following conditions are met:

- No more than 65,535 counts have occurred between unit position events.
- No direction changes between unit position events.

The capture unit sets the eQEP overflow error flag (QEPSTS[COEF]) in the event of capture timer overflow between unit position events. If a direction change occurs between the unit position events, then an error flag is set in the status register (QEPSTS[CDEF]) [56].

For high speed measurement, the method is to measure the incremental position movement in fixed unit time. This method has the following equation:

$$v(k) = \frac{x(k) - x(k-1)}{T} = \frac{\Delta x}{T} \tag{45}$$

where, x(k-1) is the position at time instant k, x(k-1) is the position at time instant k-1, T is the fixed unit time and Δ x is the incremental position movement in unit time.

Capture Timer (QCTMR) and Capture period register (QCPRD) can be configured to latch on following events. The read of QPOSCNT register will be saved even if the QEPCTL[QCLM] bit is cleared, then the capture timer and capture period values are latched into the QCTMRLAT and QCPRDLAT registers, respectively, when the CPU reads the position counter (QPOSCNT). If the QEPCTL[QCLM] bit is set, then the position counter, capture timer, and capture period values are latched into the QPOSLAT, QCTMRLAT and QCPRDLAT registers, respectively, on unit time out. Unit time (T) and unit period(x) are configured using the QUPRD and QCAPCTL[UPPS] registers. Incremental position output and incremental time output is available in the QPOSLAT and QCPRDLAT registers [57].

For the speed measurement in this project, the second method used to calculate the speed. It is necessary process the calculation results to reduce the amplifying noise generated by the pure differentiator. A simple 1st -order low-pass filter is used, then the actual rotor speed to be used is the output of the low-pass filter.

5.3.4 Optimization of Stator Flux Linkage Estimation

For stator flux linkage estimation, it can be achieved with an integrator in the simulation model. It is can be seen from Equation (31) that this method is simple and low parameter dependent. However, when it is in the real-time experiment, since there will be sampling error from ADC during the sampling stage. This issue will bring saturation by DC drift during the stator flux linkage estimation which will impact the accuracy of the calculation and control. In order to solve this issue, a high pass filter has been used series with the integrator, which can filter the DC component of the signals.

To apply 1st-order high-pass filter in a discrete system is shown below:

Since the transfer function of 1st-order high-pass RC filter in s-plane is:

$$\frac{V_{out(s)}}{V_{in(s)}} = \frac{1}{\frac{1}{RCs}+1} \tag{46}$$

Then use z transformation, let $s = \frac{1-z^{-1}}{T_s}$, T_s is the sampling time. Substituted into Equation (46), to get:

$$V_{out(z)} + \frac{T}{RC\left(1-z^{-1}\right)} V_{out(z)} = V_{in(z)} \tag{47}$$

Then it can be converted to:

$$\left(1+\frac{T}{RC}\right)V_{out(z)} - z^{-1}V_{out(z)} = V_{in(z)} - z^{-1}V_{in(z)} \tag{48}$$

Then the Equation (47) can be converted to differential equation, which is:

$$V_{out(t)} = \frac{RC}{RC+T} V_{out(t-1)} + \frac{RC}{RC+T}\left(V_{in(t)} - V_{in(t-1)}\right) \tag{49}$$

In the project, RC is assumed to be 0.02, which means the cut off frequency $f_c = \frac{1}{2\pi RC} = 7.958Hz$.

5.3.5 Optimization Software Design for Accelerating the Calculation

According to the ADC INT flowchart above, here are the tasks need to be finished in the ADC INT:

- Processing the sample result from ADC to get the value in propriate value.
- Take mathematical mean of the sample results to filter the sample results.
- Utilizing Clarke Transformation to convert the sample results to *α*- and *β*-axis voltage and current.

Since the frequency of ADC INT is related to the ADC sampling frequency. In order to achieve higher sample frequency, the time used for calculation in ADC INT should be as small as possible. At first, after simplifying the calculation, it still requires about 283 CPU clock to finish the calculation. As the result of that, the sampling frequency of ADC is set to be 500 kHz at the beginning [55].

After investigation of Clarke Transformation, it is found that it can use two-phase voltage and current to do the transformation. After solving the matrix of Clarke Transformation, it proves that less clock will be consumed if Clarke Transformation is rewritten in equation format not matrix format. After the optimization, the clock for calculation is reduced to 133. So, the sampling frequency can be doubled, which is 1MHz, and the sample results will be more precise.

5.4. Experiment Results and Analysis

After the implementation design for DTC-SVM of PMSM, an experiment has been conducted in CHARGE LAB using DSP TMS320F8335 to evaluate the DTC-SVM control of PMSM. The dc-link voltage is 170 V and the switching frequency is 10 kHz. Some experimental results are obtained from the digital to analog converter (DAC) circuit with the cutoff frequency of 328.83 Hz.

Figure 5.19-5.21 below shows the experiment *α*- and *β*-axis stator phase voltages, currents and stator flux linkages estimation using DTC-SVM. Then Fig. 5.22-5.23 below shows the experiment torque response at the starting point and the varying speed response using DTC-SVM.

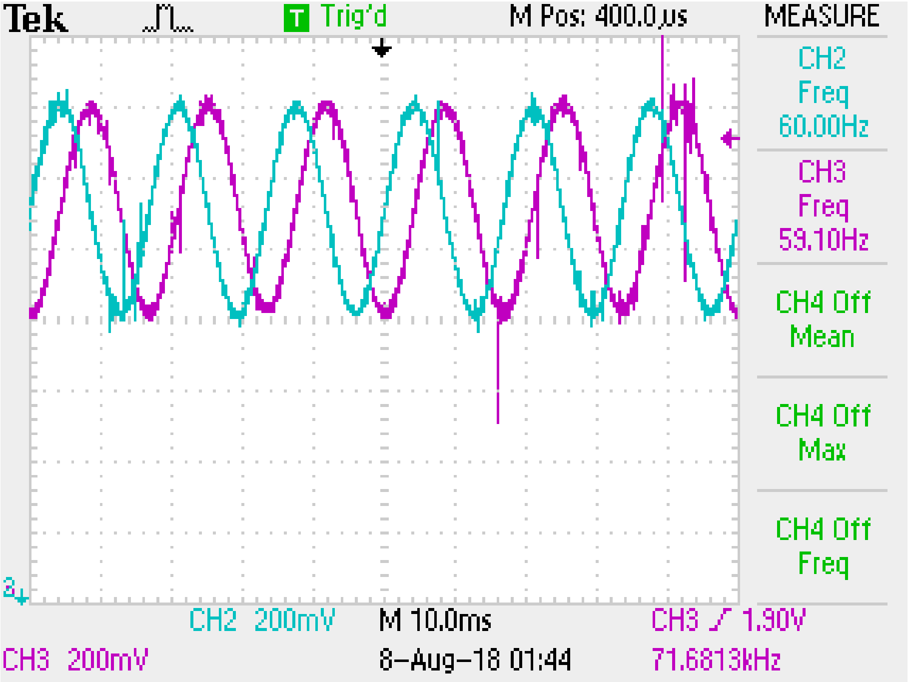

Fig. 5.19. Experiment α- and β-axis stator phase voltages using DTC-SVM at 900 RPM.

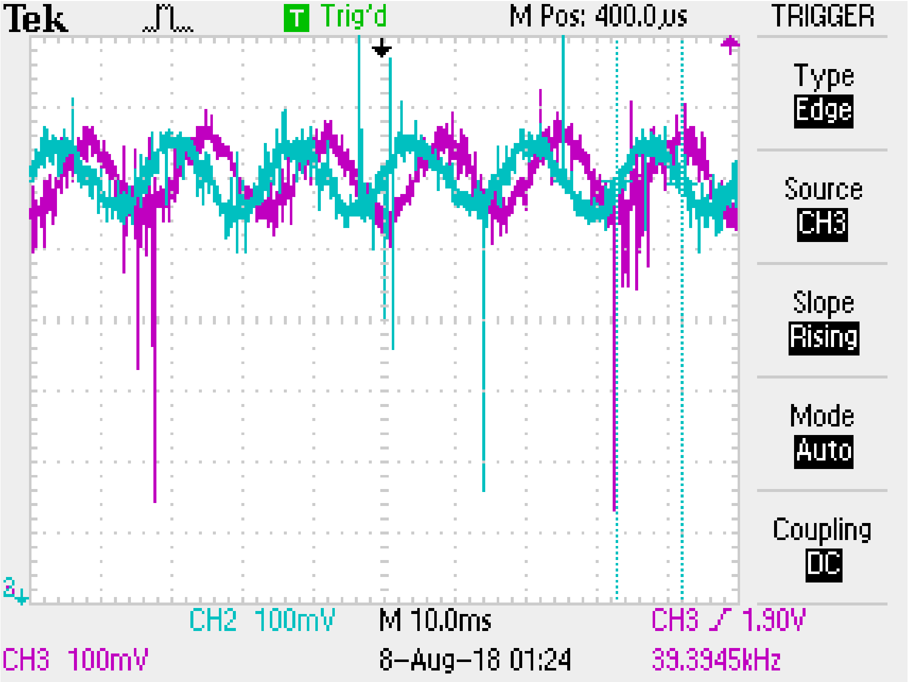

Fig. 5.20. Experiment α- and β-axis stator phase currents using DTC-SVM at 900 RPM.

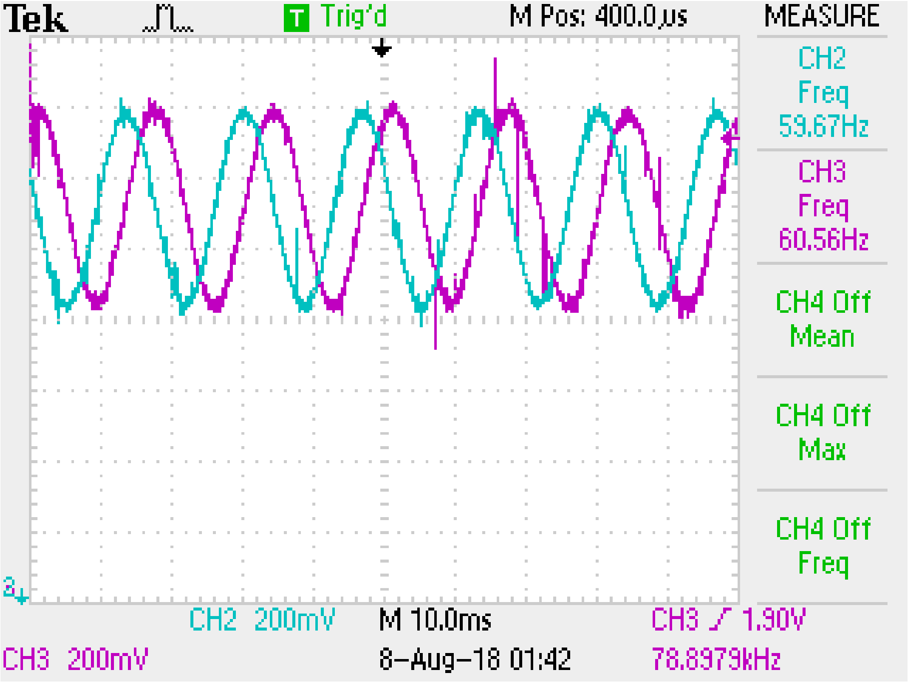

Fig. 5.21. Experiment α- and β-axis stator flux linkages using DTC-SVM at 900 RPM.

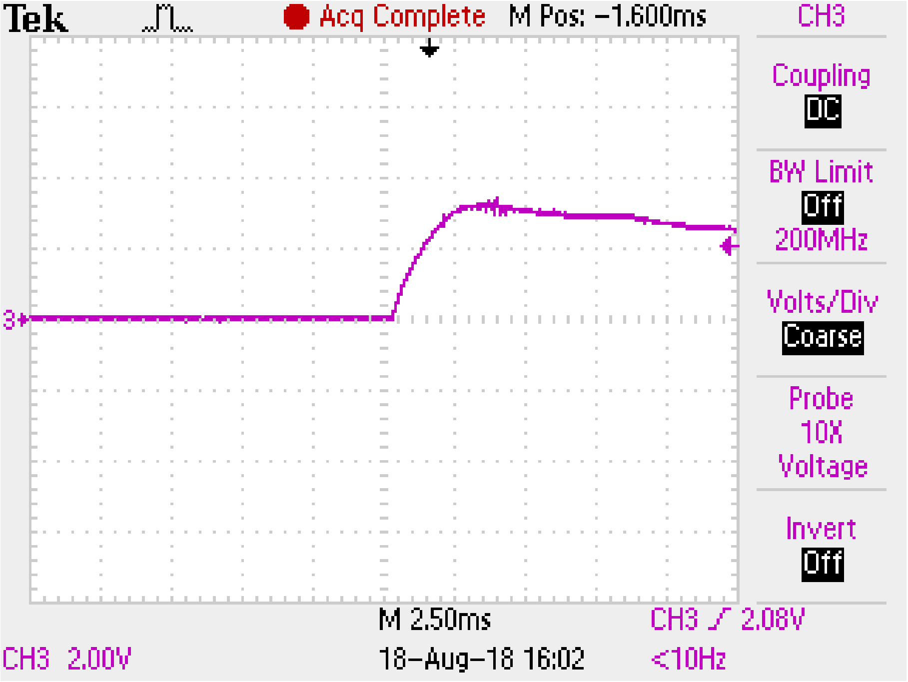

Fig. 5.22. Experiment torque response using DTC-SVM at starting point.

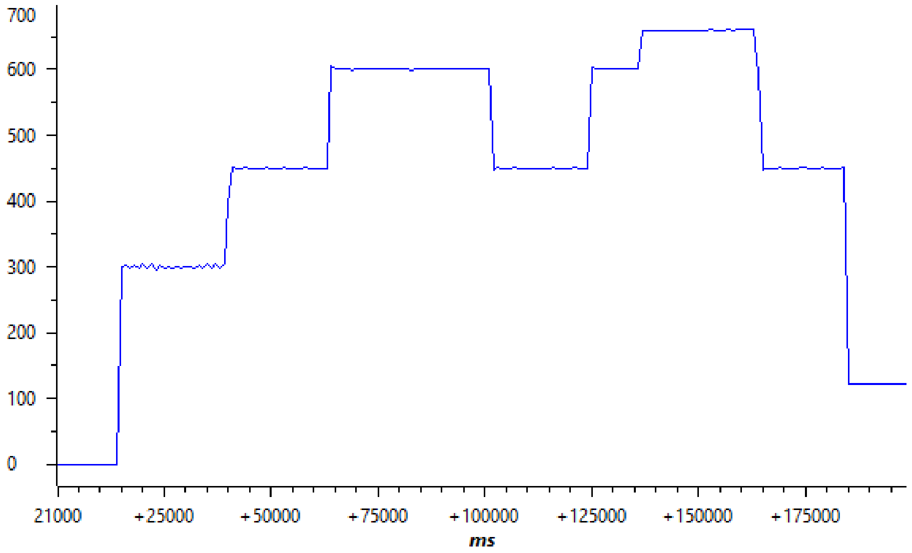

Fig. 5.23. Experiment varying speed response using DTC-SVM.

From the experiment results, the DTC-SVM of PMSM is successfully implemented using DSP TMS320F28335. The α- and β-axis stator phase voltages, currents and flux linkage estimation have constant amplitude and the frequency is relative to the speed of PMSM.

Chapter 6

Conclusions and Future Work

6.1. Conclusions

This thesis focuses on the design and implementation of high-performance DTC for PMSMs for a GaN based high switching frequency motor drive, which will be the next-generation motor drive for the future applications.

First, the characteristics and operation principles of a PMSM are introduced. Then, the mathematical models of a PMSM under different coordinate systems are investigated. Consequently, a PMSM model is developed based on the dq rotating reference frame and implemented in the MATLAB/Simulink for validation. Two advanced PMSM control strategies, FOC and DTC, are investigated and compared in terms of control performance through comprehensive simulation studies and the results demonstrate that DTC has better dynamic performance.

Conventional DTC contributes to higher torque ripple in the PMSM due to the limited switching frequency in a conventional semiconductor-based motor drive, which inevitably deteriorates the drive performance. Therefore, this thesis aimed to reduce the torque ripple in the DTC based PMSM drive by using the new generation wide bandgap switching devices. More specifically, DTC is improved by using the optimized space vector pulse width modulation strategy and a higher switching frequency contributed by the GaN based motor drive.

Finally, the proposed DTC based PMSM control strategy is implemented on the DSP and evaluated on the laboratory GaN based PMSM drive. Both the simulation and experimental results show that the proposed improvement in the DTC can further improve the PMSM drive performance. The effectiveness of the DTC-SVM schemes developed has been demonstrated and validated by simulation results as well as experimental studies on an 400W PMSM drive system.

6.2. Future Work

Recommendations for future work are summarized as follows:

(1) The control performance of DTC depends on the accuracy of the stator flux estimation. Both the amplitude and phase would be impact through the filter. Therefore, it is necessary to investigate precise stator flux estimation. Maybe a phase lock loop could be used to lock the amplitude and phase.

(2) Now for the DTC-SVM of PMSM, the speed calculation is still acquired through the encoder signals. In the future, it should be sensorless, so that there is no need for the encoder.

(3) Investigate the dead band loss and switching loss associated with GaN inverter associated with the DTC-SVM. Especially, during the high switching frequency over 100 kHz. It will be very important to improve the control performance and investigate how the inverter could operate under high switching frequency condition and how the heat would effect on GaN.

REFERENCES/BIBLIOGRAPHY

[1] N. Mohan, *Advanced Electric Drives: Analysis, Control and Modeling Using Simulink,* MNPERE, 2001.

[2] P. Vas, *Sensorless Vector and Direct Torque Control*, Oxford University Press, July 1998.

[3] K. T. Chau, *Electric Vehicle Machines and Drives: Design, Analysis and Application*, New York, NY, USA: Wiley, 2015

[4] *Electric Motors for Electric Vehicles 2013-2023: Forecasts, Technologies, Players*, IDTechEx research report, Nov. 2013.

[5] J. F. Gieras, *Permanent Magnet Motor Technology: Design and Applications,* CRC Press, 2010.

[6] Z. Zhang, “Direct Torque Control of Permanent Magnet Synchronous Machines with Applications to Motor Drives and Wind Energy Conversion Systems,” Ph.D. dissertation, Dept. Elect. Eng., University of Nebraska-Lincoln, Lincoln, NE, 2015.

[7] P. D. Chandana Perera, *Sensorless control of Permanent Magnet Synchronous Motor Drives*, Aalborg University, Second Edition, 2002. ISBN 87-89179-41-2.

[8] L. Zhong, M. F. Rahman, W. Y. Hu and K. W. Lim, "Analysis of direct torque control in permanent magnet synchronous motor drives," in *IEEE Transactions on Power Electronics*, vol. 12, no. 3, pp. 528-536, May 1997.

[9] P. Vas, *Sensorless Vector and Direct Torque Control*, Oxford University Press, July 1998.

[10] D. W. Novotny and T. A. Lipo, *Vector Control and Dynamics of AC Drives,* Oxford University Press Inc., NY, 1996.

[11] J. Luukko, “Direct torque control of permanent magnet synchronous machines analysis and implementation,” Ph.D. dissertation, Lappeenranta University of Technology, Lappeenranta, Finland, 2000.

[12] I. Takahashi and T. Noguchi, “A new quick-response and high efficiency control strategy of an induction machine,” *IEEE Trans. Ind. Appl.*, vol. IA–22, pp. 820– 827, Sep./Oct. 1986.

[13] M. Depenbrock, “Direct self control of inverter-fed induction machines,” *IEEE Trans. Power Electron.*, vol. 3, pp. 420–429, Oct. 1988.

[14] U. Baader, M. Depenbrock, and G. Gierse, “Direct self control (DSC) of inverter-fed-induction machine—A basis for speed control without speed measurement,” *IEEE Trans. Ind. Appl.*, vol. 28, pp. 581–588, May/Jun. 1992.

[15] P. Tiitinen and M. Surandra, “The next generation motor control method, DTC direct torque control,” in *Proc. International Conference on Power Electronics, Drives and Energy Systems for Industrial Growth*, Jan. 1996, vol. 1, pp. 37-43.

[16] L. Zhong, M. F. Rahman, W. Y. Hu and K. W. Lim, "Analysis of direct torque control in permanent magnet synchronous motor drives," in *IEEE Transactions on Power Electronics*, vol. 12, no. 3, pp. 528-536, May 1997.

[17] “Direct torque control,” ABB, Tech. Rep. Jun. 2011.

[18] X. del Toro Garcia, B. Zigmund, A. Terlizzi, R. Pavlanin and L. Salvatore "Comparison between FOC and DTC strategies for permanent magnet synchronous motors," *Advances in Electrical and Electronic Engineering*, vol. 5 no. pp. 76-82 May 2006.

[19] Y. Hu, C. Tian, Y. Gu, Z. You, L. X. Tang and M. F. Rahman, "In-depth research on direct torque control of permanent magnet synchronous motor," *IEEE 2002 28th Annual Conference of the Industrial Electronics Society*. IECON 02, 2002, pp. 1060-1065 vol.2.

[20] V. Ambrozic, G. S. Buja and R. Menis, "Band-constrained technique for direct torque control of induction motor," in *IEEE Transactions on Industrial Electronics*, vol. 51, no. 4, pp. 776-784, Aug. 2004.

[21] D. Casadei, G. Serra and K. Tani, "Implementation of a direct control algorithm for induction motors based on discrete space vector modulation," in *IEEE Transactions on Power Electronics*, vol. 15, no. 4, pp. 769-777, Jul 2000.

[22] D. Casadei, F. Profumo, G. Serra and A. Tani, "FOC and DTC: two viable schemes for induction motors torque control," in *IEEE Transactions on Power Electronics*, vol. 17, no. 5, pp. 779-787, Sep 2002.

[23] Li Lianbing, Wang Xiaojun and Sun Hexu, "A variable-voltage direct torque control based on DSP in PM synchronous motor drive," *TENCON '02. Proceedings. 2002 IEEE Region 10*

Conference on Computers, Communications, Control and Power Engineering, 2002, pp. 2065-2068 vol.3.

[24] Y. S. Lai, Wen-Ke Wang and Yen-Chang Chen, "Novel switching techniques for reducing the speed ripple of AC drives with direct torque control," in *IEEE Transactions on Industrial Electronics*, vol. 51, no. 4, pp. 768-775, Aug. 2004.

[25] Y. Kwak, J. W. Ahn and D. H. Lee, "A high performance direct torque control method with PWM approach of PMSMs," *2014 IEEE International Conference on Industrial Technology (ICIT)*, Busan, 2014, pp. 61-66.

[26] S. S. Sebtahmadi, H. Pirasteh, S. H. Aghay Kaboli, A. Radan and S. Mekhilef, "A 12-Sector Space Vector Switching Scheme for Performance Improvement of Matrix-Converter-Based DTC of IM Drive," in *IEEE Transactions on Power Electronics*, vol. 30, no. 7, pp. 3804-3817, July 2015.

[27] X. Liao, L. Shao, “The Twelve-section Control Methods of Direct Torque Control,” *Proceeding of the CSEE*, 2006, 26(6): 167-173.

[28] Y. Wang, J. G. Zhu and Y. G. Guo, "A survey of direct torque control schemes for permanent magnet synchronous motor drives," *2007 Australasian Universities Power Engineering Conference*, Perth, WA, 2007, pp. 1-5.

[29] J.-K. Kang and S.-K. Sul, “Analysis and prediction of inverter switching frequency in direct torque control of induction machine based on hysteresis band and machine parameters,” *IEEE Trans. Ind. Electron*., Vol. 48, No. 3, pp. 545-553, Jun. 2001.

[30] Yen-Shin Lai and Jian-Ho Chen, "A new approach to direct torque control of induction motor drives for constant inverter switching frequency and torque ripple reduction," in *IEEE Transactions on Energy Conversion*, vol. 16, no. 3, pp. 220-227, Sept. 2001.

[31] J. Zhang, M. F. Rahman and C. Grantham, "A New Scheme to Direct Torque Control of Interior Permanent Magnet Synchronous Machine Drives for Constant Inverter Switching Frequency and Low Torque Ripple," *2006 CES/IEEE 5th International Power Electronics and Motion Control Conference*, Shanghai, 2006, pp. 1-5.

[32] G. Foo, S. Sayeef and M. F. Rahman, "Sensorless SVM direct torque controlled interior permanent magnet synchronous drive," *2007 Australasian Universities Power Engineering Conference*, Perth, WA, 2007, pp. 1-5.

[33] G. Foo, S. Sayeef and M. F. Rahman, "Wide speed sensorless SVM direct torque controlled interior permanent magnet synchronous motor drive," *2008 34th Annual Conference of IEEE Industrial Electronics*, Orlando, FL, 2008, pp. 1439-1444.

[34] G. Foo, C. S. Goon and M. F. Rahman, "Analysis and design of the SVM direct torque and flux control scheme for IPM synchronous motors," *2009 International Conference on Electrical Machines and Systems*, Tokyo, 2009, pp. 1-6.

[35] T. G. Habetler, F. Profumo, M. Pastorelli, and L. M. Tolbert, "Direct torque control of induction machines using space vector modulation," *IEEE Trans. Ind. Appl.*, vol. 28, no. 5, pp. 1045–1053, Sep./Oct. 1992.

[36] F. Niu, B. Wang, A. S. Babel, K. Li and E. G. Strangas, "Comparative Evaluation of Direct Torque Control Strategies for Permanent Magnet Synchronous Machines," in *IEEE Transactions on Power Electronics*, vol. 31, no. 2, pp. 1408-1424, Feb. 2016.

[37] G. H. B. Foo and X. Zhang, "Constant Switching Frequency Based Direct Torque Control of Interior Permanent Magnet Synchronous Motors With Reduced Ripples and Fast Torque Dynamics," in *IEEE Transactions on Power Electronics*, vol. 31, no. 9, pp. 6485-6493, Sept. 2016.

[38] C. Lascu and I. Boldea, "Variable-structure direct torque control - a class of fast and robust controllers for induction machine drives," *IEEE Trans. Ind. Electron.*, Vol. 51, No. 4, pp. 785-792, Aug. 2004.

[39] S. K. Lin and C. H. Fang, "Sliding-mode direct torque control of an induction motor," in *Proc. IECON,* Mar. 2001, pp. 2117-2177.

[40] D. Sun, Y. K. He, and J. G. Zhu, "Fuzzy logic direct torque control for permanent magnet synchronous motors," in *Proc. 5th World Congress on Intelligent Control and Automation,* Jun. 2004, Vol. 5, pp. 4401-4405.

[41] G. S. Buja and M. P. Kazmierlowski, "Direct torque control of PWM inverter fed AC motors-a survey," *IEEE Trans. Industrial Electronics*, vol. 51, no. 4, pp. 744-757, Aug. 2004.

[42] E. A. Jones, F. F. Wang and D. Costinett, "Review of Commercial GaN Power Devices and GaN-Based Converter Design Challenges," in *IEEE Journal of Emerging and Selected Topics in Power Electronics*, vol. 4, no. 3, pp. 707-719, Sept. 2016.

[43] T. P. Chow, “Progress in high voltage SiC and GaN power switching devices,” *Mater. Sci. Forum*, vols. 778–780, pp. 1077–1082, 2014.

[44] T. P. Chow, “Wide bandgap semiconductor power devices for energy efficient systems,” in *Proc. IEEE Workshop Wide Bandgap Power Devices Appl. (WiPDA)*, Nov. 2015, pp. 402–405.

[45] S. Chowdhury, Z. Stum, Z. D. Li, K. Ueno, and T. P. Chow, “Comparison of 600V Si, SiC and GaN power devices,” *Mater. Sci. Forum*, vols. 778–780, pp. 971–974, 2014.

[46] J. Millan, P. Godignon, X. Perpina, A. Perez-Tomas, and J. Rebollo, “A survey of wide bandgap power semiconductor devices,” *IEEE Trans. Power Electron.*, vol. 29, no. 5, pp. 2155–2163, May 2014.

[47] B. Ozpineci and L. M. Tolbert, “Comparison of wide-bandgap semiconductors for power electronics applications,” Oak Ridge Nat. Lab., Oak Ridge, TN, USA, Tech. Rep. ORNL/TM-2003/257, 2003.

[48] J. Styles, “Company Update,” GaN Systems, Sep. 2015.

[49] “Design with GaN Enhancement mode HEMT”, GaN Systems Inc. April 12, 2018.
[50] X. Wang, Y. Xing, Z. He, and Y. Liu, “Research and Simulation of DTC Based on SVPWM of PMSM,”, *Procedia Engineering*., vol. 29, pp. 1685-1689, 2012.

[51] D. Swierczynski and M. P. Kazmierkowski, "Direct torque control of permanent magnet synchronous motor (PMSM) using space vector modulation (DTC-SVM)-simulation and experimental results," *IEEE 2002 28th Annual Conference of the Industrial Electronics Society. IECON 02*, Sevilla, 2002, pp. 751-755 vol.1.

[52] L. Tang, L. Zhong, M. F. Rahman and Y. Hu, "A novel direct torque control scheme for interior permanent magnet synchronous machine drive system with low ripple in torque and flux, and fixed switching frequency," *2002 IEEE 33rd Annual IEEE Power Electronics Specialists Conference. Proceedings (Cat. No.02CH37289)*, Cairns, Qld., Australia, 2002, pp. 529-534 vol.2.

[53] A. H. Abosh, Z. Q. Zhu and Y. Ren, "Reduction of Torque and Flux Ripples in Space Vector Modulation-Based Direct Torque Control of Asymmetric Permanent Magnet Synchronous Machine," in *IEEE Transactions on Power Electronics*, vol. 32, no. 4, pp. 2976-2986, April 2017.

[54] "TMS320F2833x, TMS320F2823x Digital Signal Controllers (DSCs) datasheet (Rev. N)", Texas Instruments,18 OCT, 2016.

[55] "TMS320x2833x, 2823x Analog-to-Digital Converter (ADC) Module Reference Guide", Texas Instruments, Oct. 2007.

[56] "Digital Motor Control, Software Library: F2833x Drivers", Texas Instruments, 2012.

[57] "TMS320x2833x, 2823x Enhanced Quadrature Encoder Pulse (eQEP) Reference Guide", Texas Instruments, Dec. 2008.

[58] "TMS320C28x Floating Point Unit and Instruction Set Reference Guide", Texas Instruments, Aug. 2008.

[59] "TMS320x2833x, 2823x Enhanced Pulse Width Modulator (ePWM) Reference Guide", Texas Instruments, Jul. 2009.

[60] "TMS320x2833x, 2823x System Control and Interrupts Reference Guide", Texas Instruments, Mar. 2010.

VITA AUCTORIS

NAME: Junxi Cai

PLACE OF BIRTH: Jiaxing, Zhejiang, China

YEAR OF BIRTH: 1992

EDUCATION: Jiaxing No.1 High School, Jiaxing, Zhejiang, China, 2007

Shenyang University of Technology, B.Sc., Shenyang, Liaoning, China, 2010

University of Windsor, M.eng., Windsor, ON, 2015